ELECTRON MICROSCOPE STUDIES

Progress Report
DOE ER 60437-6

for Period 1 July 1990 to 1 June 1991

A. V. Crewe and O. H. Kapp
The University of Chicago
The Enrico Fermi Institute and
The Department of Physics

June 1, 1991

Prepared for
The U.S. Dept. of Energy
Agreement Number DE-FG02-86ER60437

DOE/ER/60437--6

DE92 004693

ELECTRON MICROSCOPE STUDIES

Progress Report
DOE ER 60437-6

for Period 1 July 1990 to 1 June 1991

A. V. Crewe and O. H. Kapp
The University of Chicago
The Enrico Fermi Institute and
The Department of Physics

June 1, 1991

Prepared for
The U.S. Dept. of Energy
Agreement Number DE-FG02-86ER60437

Notice

Contents

Abstract

This year our laboratory has continued to make progress in the design of electron-optical systems, in the study of structure-function relationships of large multi-subunit proteins, in the development of new image processing software and in achieving a workable sub-angstrom STEM.

We present an algebraic approach to the symmetrical Einzel (unipotential) lens wherein we simplify the analysis by specifying a field shape that meets some preferred set of boundary or other conditions and then calculate the fields.

In a second study we generalize this approach to the study of three element electrostatic lenses of which the symmetrical Einzel lens is a particular form. The purpose is to develop a method for assisting in the design of a lens for a particular purpose.

In our biological work we study a stable and functional dodecameric complex of globin chains from the hemoglobin of *Lumbricus terrestris*. This is a complex lacking the "linker" subunit first imaged in this lab and required for maintenance of the native structure. In addition, we do a complete work-up on the hemoglobin of the marine polychaete *Eudistylia vancouverii* demonstrating the presence of a hierarchy of globin complexes.

We demonstrate stable field-emission in the sub-angstrom STEM and the preliminary alignment of the beam.

We continue our exploration of a algorithms for alignment of sequences of protein and DNA.

Our computer facilities now include four second generation RISC workstations and we continue to take increasing advantage of the floating-point and graphical performance of these devices.

Introduction

The work in this laboratory has continued in the multi-disciplinary fashion of past years. Our emphasis is still on the development of ideas and methods in the design and use of electron microscopes and the experimental application of these instruments with a particular emphasis on biology.

In the past year we have been able to take advantage of some support from the State of Illinois. We have obtained editorial and programming help along with a state-of-the-art workstation (IBM RS6000-730) connected to a high-speed (100 Mbit/sec.) network. We have also directed a senior project for an undergraduate (E. Lipman) and have been advisor for a Ph.D. project (D. Gunter, June, 91). In addition, a student from the University of Illinois (M. Ryan) obtained a MS in computer science for work done in this lab this past year.

We have taken a look at Einzel lenses with an eye toward simplifying the calculations in order to facilitate the design process. Briefly we specify a field shape that meets some preferred set of boundary or other conditions and then calculate the field. If a particular distribution is chosen for fabrication, the eletrodes can be made by reproducing the equipotentials, an approach that proved successful in the design of the Butler accelerating lens. In this work we demonstrate that it is possible to predict the first and third order optical properties of this type of lens by using just two parameters, the physical length of the lens and the potential on the axis at the mid-point.

We have generalized these observations by examining the common three element electrostatic lens in order to develop a better understanding of their characteristics. Using a limited set of parameters and also using the simplest potential distribution that will suffice for the problem, we have developed expressions for the three important properties of these lenses, the focal length and the coefficients of spherical and chromatic aberration.

We have made good progress with the sub-angstrom STEM project and now have steady field-emission and are aligning the beam. We have solved a number of mechanical and vacuum problems and have developed a relatively sophisticated program for automatic conditioning of the field-emission tip. We are presently using a CCD camera to monitor a scintillator in order to make the initial alignments of the optical column.

Through individual agreements with IBM and DEC we have obtained three additional RISC workstations. We now have two DEC 5000 and two IBM RS-6000 workstations. Each manufacturer has supplied us with configurations that include high-end graphics capabilities. In addition DEC has supplied us with their product set for FDDI compatible networking of their workstations. This network, along with the high-speed network, already partially installed (to connect our lab with other imaging labs on campus), puts us in a unique position to experiment with this rapidly evolving technology.

To emphasize the importance of the newest generation of workstations O. Kapp and R. Beck hosted a joint industry-university conference on high performance workstations and visualization (see appendix). Funded by the manufacturers, this conference featured presentations by several experts in this area of research.

We have continued our research into the structure and function of proteins. Our model system, the invertebrate hemoglobins, has provided us with many challenges because of the extraordinary diversity of functional and structural characteristics of these respiratory proteins. Of particular interest this year was a thorough study of the hemoglobin of the marine worm *Eudistylia vancouverii*. In this work we compared characteristics of this giant protein with the structures of other hemoglobins that we have studied using the STEM and other techniques. In addition, we were able to apply a technique to determine the subunit stoichiometry of this protein using linear equations, a method developed in this lab over the past two years.

This past summer one of us (O. Kapp) with S. Vinogradov organized a meeting on invertebrate di-oxygen binding carriers. The proceedings were edited in this lab and are being published by Springer-Verlag. This book is in press and the front matter and index appears in the appendix.

We have continued our work on algorithm development for sequence alignment. This work was stimulated by the difficulties we encountered while trying to use published subroutines to align invertebrate hemoglobin sequences. Compared to the vertebrate hemoglobin sequences, of which about 400 are known, there is a relatively low sequence homology among the few known invertebrate sequences. We have thus spent considerable time developing algorithms for alignment of these sequences and have made use of the advanced graphics capabilities of our new workstations to explore the more promising 3D methods for alignment comparison. Using the 3D structure of a homologous protein, the proper alignment is determined by fitting the primary sequence of a second protein to this three-dimensional model.

Finally, one of us (A. Crewe) will host a colloquium at the National Academy of Sciences entitled "Science of Images-Images of Science" to be held this Fall. This conference will bring together experts in the various aspects of imaging science and provide additional impetus to this evolving field. The proceedings of this meeting will by published in the *Proceedings of the National Academy*.

I. THEORETICAL STUDIES

An Algebraic Approach to the Symmetrical Einzel Lens

Introduction

The Einzel or unipotential lens has been the subject of much study and there are innumerable papers in the literature, far too many to refer to individually, but a good summary can be found in Grivet (1). The early work was hampered by lack of precise knowledge of the shape of the potential and the calculations of the aberrations were therefore inaccurate (2). Later papers concentrated upon an analysis of mathematical approximations to field shapes (3) and in particular on the use of field shapes for which the equations of motion could be integrated. Most of these publications have dealt with simple geometrical structures such as coaxial cylinders (3) or flat plates (4) because they are easy to make and the potential can be approximated. Some attention has been given to the calculation of the properties of lenses using thick electrodes (4) and in addition, there are experimental studies on the same problem, the most extensive being the one by Rempfer (5). The difficulties are many, however, principally because there are so many adjustable parameters. In fact, the experimental approach does not appear to be a good way to proceed.

As a result of all this work, there are a number of lens designs that are available and many that are in common use. However, it is not at all certain that these are the best designs and we hope to show that there is still more work that can be done to improve them.

Approaches to this design problem have all ultimately depended upon the calculational techniques that can be applied. In the absence of computers, investigators had to depend upon analytical techniques. It seems to be true that the number of field shapes that can be investigated in this way is very few indeed. The first order equations are difficult enough, but the third order equations are for the most part, quite intractable. This means that it is often not possible to calculate the aberration coefficients, or the results are admittedly inaccurate.

With the advent of computers it has become possible to study a larger variety of potential distributions but it is nevertheless difficult to obtain accurate results. As we will show later, very lengthy calculations are needed to obtain, for example, one percent accuracy. This lack of precision has obscured the situation to a large extent with the result that there is little insight available to the design problem and no guidance through the maze of choices.

The field shapes that are amenable to calculation are not the ones that can be readily manufactured and in reverse, electrodes that are easily made lead to fields that are not easily calculated. For the most part, this has lead to a compromise and the use of flat plates with a central hole. Three of these arranged along the axis will form an Einzel lens. Finite element methods can be used to determine the fields and ray-tracing methods can be used to calculate the trajectories. This method is now in common use but there are some inherent difficulties, especially with the problem of determining the fields with sufficient accuracy.

As a result of all these calculations and experimental measurements, the designer is faced with a multitude of options, many of which are in conflict. There are numerous compilations of numerical data (e.g. (6)), graphs and approximations and very little guidance in finding the optimum system for any given application. This is not too surprising since even the simplest symmetrical three electrode system involves the choice of at least five parameters (two hole diameters, two electrode lengths and one spacing). Of particular concern is that the choice of parameters is often such that the data must be given in the form of graphs, often with steep slopes, so that accurate results are not easily obtained. One of the most common methods in use is to characterize the lenses in terms of the diameter of the hole in the central electrode and to calculate the coefficient of spherical aberration in terms of the focal length. Neither of these seems to be a good way to proceed. If one views the lens as being a potential distribution then one can make the same axial distribution in a variety of ways and the hole diameter does not play a direct role. It is always possible to replace a given central electrode with one having a different hole diameter and a different length and still achieve the same potential on the axis. With regard to the spherical aberration, a far more meaningful comparison would be with the cube of the focal length.

The purpose of this paper is to try to simplify the analysis of this type of lens and find a way to present the data in a compact manner. As a part of this analysis, we have also attempted to clarify the theory and provide a way to see what is going on.

In order to try to simplify the analysis. we decided to use a method which has not previously been applied to the Einzel lens and that is to specify a field shape that meets some preferred set of boundary or other conditions and then calculate the fields. If one of the distributions were to be chosen for fabrication, the electrodes could be made by reproducing the equipotentials. It was this kind of approach that was so successful in the Butler accelerating lens. It is the approach that we will use here.

It is now more appropriate to use this method because computer time is no longer as expensive as it used to be and we can afford to experiment with different functions and shapes. We are not constrained by the need to solve differential equations or conserve computer time. In addition, it is feasible to fabricate unusual electrode shapes using numerically controlled machine tools. The flat plate is no longer the only reasonable choice.

One final remark to be made here is that we have performed numerous calculations on the properties of lenses over a number of years. In almost all of the calculations, the main problem has been that of defining the length of the field distribution. It has always proved to be difficult to obtain satisfactory consistency unless the field is known over almost the whole distance between object and image. In order to correct this problem, we take care here to terminate the fields and reduce the end effects.

Basic Principles

The basic equations that we are using are well enough established that we can simply write them down without justification. The potential V(r,z) is assumed to be cylindrically symmetric and -eV gives the kinetic energy of the electrons. All derivatives are with respect to the distance along the z-axis. The first order equation of radial motion is

$$r'' = -\frac{r' V'}{2 V} - \frac{r}{4}\frac{V''}{V} \tag{1}$$

and the spherical aberration coefficient is given by the integral

$$C_s = \frac{1}{16 r_i'^4}\int \left[\left(\frac{5}{4}\frac{V''^2}{V} + \frac{5}{24}\frac{V'^4}{V}\right) r^4 + \frac{14}{3}\frac{V'^3}{V} r^3 r' - \frac{3}{2}\frac{V'^2}{V} r^2 r'^2\right]\sqrt{\frac{V}{V_i}}\, dz \tag{2}$$

while the coefficient of chromatic aberration is given by the integral

$$C_c = \frac{1}{r_i'^2}\int \left[\frac{r' V'}{2 V} + \frac{r}{4}\frac{V''}{V}\right] r\sqrt{\frac{V_i}{V}}\, dz \tag{3}$$

In these equations r and r' inside the integral refer to the unaberrated or Gaussian ray and the subscript i refers to the conditions at the image.

Before proceeding with the numerical results, it is helpful to analyze the equations of motion in order to know what to expect and also to gain some insight into the problem. In this respect, we have found it helpful to transform the equations by using the Picht transformation. This consists of replacing the radius r with

$$R = rV^{\frac{1}{4}}$$

Using this new variable, the first order equation is simplified to

$$R'' = -\frac{3}{16} T^2 R \tag{4}$$

where $T = \frac{V'}{V}$ and the expressions for the two aberration coefficients become

$$C_s = \frac{1}{16 r_i'^4}\int \left[\left(\frac{5}{4}T'^2 + \frac{5}{2}T'T^2 + \frac{35}{24}T^4\right) r^4 + \frac{14}{3}T^3 r' r^3 - \frac{3}{2}T^2 r'^2 r^2\right]\sqrt{\frac{V}{V_i}}\, dz \tag{5}$$

$$C_c = \frac{1}{r_i'^2}\int \frac{3}{8} T^2 r^2 \sqrt{\frac{V_i}{V}}\, dz \tag{6}$$

Putting the first order equation into this form already gives some insight because of the similarity with magnetic lenses where the equivalent equation can be written as

$$r'' = -\frac{U^2}{4} r$$

where

$$U = \frac{B}{3.37\sqrt{V}}$$

The Picht transformation is particularly helpful when we consider long focal lengths, that is to say, the thin lens approximation. Taken to the extreme, if we consider the lens to be so weak that the radius does not change in passing through the lens, the only effect is that the slope of the ray changes. In this case, the focal length is given by

$$\frac{1}{f} = \frac{3}{16}\int T^2 \, dz \tag{7}$$

the expression for the chromatic aberration coefficient becomes

$$C_c = f^2 \int \frac{3}{8} T^2 \sqrt{\frac{V_i}{V}} \, dz \tag{8}$$

and the spherical aberration coefficient is

$$C_s = \frac{f^4}{16}\int \left[\frac{5}{4}T'^2 + \frac{5}{2}T'T^2 + \frac{35}{24}T^4\right]\sqrt{\frac{V}{V_i}} \, dz \tag{9}$$

Further progress can be made if we assume some particular function for T. In fact, it is not likely that this function must be specified with any great precision since we are using an impulse approximation. One function that seems to be appropriate is

$$T = Az \ \exp\left(\frac{-z^2}{a^2}\right) \tag{10}$$

This function has the proper shape and is readily integrated. The numerical constant can be obtained by integrating from 0 to infinity and comparing with the central voltage V_1. This gives

$$A = \frac{2}{a^2}\ln\left(\frac{V_1}{V}\right)$$

By direct integration of the first order equation we can estimate the focal length

$$f = 4.24\frac{a}{\left(\ln\left(\frac{V_1}{V}\right)\right)^2}$$

In addition, using this same function we can perform the aberration integrals. In doing so we ignore the

voltage ratio factor inside the integral since it has the form $(1 + \delta V)$ which we assume is approximately equal to 1. Then the spherical aberration integral is given by

$$C_s = \frac{35f^2}{18a\sqrt{\pi}} + \frac{5f^3}{4a^2}$$

and it is now clear that we should expect the spherical aberration to have an asymptotic value of

$$C_s = \frac{5f^3}{4a^2}$$

while the chromatic aberration tends towards $C_c = 2f$

The exact value of the multiplicative constant will depend upon the precise form of the field function but we would expect that in any case, the asymptotic dependence on the focal length and the dimensions of the lens will be those given above. That is to say, we expect that the chromatic aberration will be very nearly equal to twice the focal length and the spherical aberration will be proportional to the cube of the focal length divided by the square of some characteristic length L. If we take that length to be, for example, the distance between the 10% points of the field T, then in the case of our impulse approximation, we would have $L = 4a$ and then the asymptotic values would be

$$f = 1.06 \frac{L}{\ln(\frac{V_1}{V})} \tag{11}$$

$$C_c = 2f \tag{12}$$

$$C_s = \frac{20f^3}{L^2} \tag{13}$$

These results are not very surprising. In the case of magnetic lenses, it is well known that the asymptotic value for the coefficient of spherical aberration is approximately

$$C_3 = \frac{5f^3}{L^2} \tag{14}$$

where L is the characteristic length of the lens field. This result can be inferred from the data given by Durandeau and Fert (7). This makes it clear that for fields of the same physical length, the magnetic lens is better than the electrostatic one, but only by about a factor of four.

With these expectations, we can proceed with the calculations. It seems clear that it would be helpful to compare the numerical results of our calculations with those to be expected for the asymptotic expressions. In this way, we may expect to limit the range of the various parameters and avoid having to plot the results over many decades.

In all the following calculations, the electron trajectories are obtained by ray-tracing the first order equation, using an input ray $r = 1$, $r' = 0$ unless otherwise specifed. The aberration coefficents are then obtained by evaluating the two integrals.

The ray-tracing was done using a fourth order Runge-Kutta method. All programming was done in APL since this language provided the flexibility that was needed. The field along the axis was calculated at equal intervals. The Runge-Kutta calculation was also performed in equal intervals.

The Fields

For any Einzel lens, it is quite obvious that the potential must follow some form of bell-shaped curve, either erect or inverted, such that it has the same value at the beginning and the end, but a different value in between. There must be apertures on the axis to allow the electrons to pass through and each of these apertures will form an elementary lens because in general, the fields on the two sides of the aperture are different. This makes the properties of the system very dependent on the size and location of these apertures and perhaps also the precision with which the apertures are made. We propose to eliminate this problem by keeping the potential gradient equal to zero in the vicinity of each aperture. In practice this is not difficult to do and it means that the apertures should be tapered at an angle of 54.7 degrees (arctan1.414).

In the calculations that follow, we will take the length of the electrode system to be equal to one. Simple linear scaling can then be used to provide corresponding numbers for any other length. All dimensions, including the aberration coefficients scale properly.

In addition we note that only the ratios of potentials are involved in the calculations, not the absolute values. For this reason, we will assume a potential equal to 1 at the entrance and exit of the lens. The potential given for the central value can then be used as a ratio to find any real value for a real system.

For our first calculations we will also only consider symmetrical lenses. It will be noted, however that the potential may increase or decrease inside the lens and we will consider both possibilities. Taking all this into account, we need to find field distributions that have the following properties.

1. The potential must have a value equal to 1 at $z = 0$ and $z = 1$
2. The potential should have a value V_1 at $z = .5$
3. The potential gradient must equal zero at $z = 0$ and 1

4. The potential gradient will also equal zero at some intermediate point.

It will be noted that we only need to specify the potential along the axis of the lens because the field expansion for points off axis has been assumed in deriving the equations of motion. If we select a field distribution that gives any desired property, we can fabricate the lens by calculating the potential distribution in space and then replace three of the equipotentials with conductors at the appropriate potential.

The simplest distribution that has these four properties is

$$V = 1 - (1 - V_1)[4z(1 - z)]^2 \qquad (15)$$

This distribution is symmetrical about z = .5, where the potential gradient is zero.

We require the first and second derivatives of the field in order to calculate the focal properties of the lens. One way to do this is to write down the analytical expressions for those derivatives. The other way is to form a numerical vector for the potential along the axis and then differentiate numerically. This latter method is preferable because only one line of code needs to be changed if we wish to change the field and all the derivatives. In the following calculations we first compared both methods and found no difference in the results.

The Calculations

After performing many trial calculations, we found that the computational errors can play a very significant role and it is all too easy to misinterpret the data. In particular, the number of steps in the calculation that is needed in order to obtain accurate results is surprisingly large. Even using as many as 1000 steps can lead to significant errors, especially in the case of long focal lengths. Since we think that we know what to expect in the limit of very long focal lengths, this is an important point. In fact, it was only by pursuing this difficulty that we were finally able to verify our results and obtain consistency.

The influence of the number of steps is shown in Tables 1 and 2. In the first example, we investigated the case of $V_1 = .5$. The results indicate there are large inaccuracies until the number of steps reaches 1000 or so. It should be pointed out here that the errors are not "round-off" errors. No evidence of such errors was found, and would not be expected since all calculations were performed to 64 bit precison.

It can also be seen that the source of these errors is in the Runge-Kutta routine itself since there are serious discrepancies in the first order calculation of the position of the focus.

When the number of steps is large enough, (1000 or greater) the results are quite consistent and are therefore probably reliable.

The situation is even more serious in the case of very weak lenses. Table 2 gives the results for the case of $V_1 = 0.95$. Here we see that consistency is not achieved until the number of steps reaches 50,000 or more. These two results may throw some doubt on similar calculations performed by others. In

particular, some authors indicate the use of the Munro program for lens calculations. This is a finite-element program that necessarily uses a very limited number of steps, otherwise the mesh would become too large for the memory of any computer. It seems clear that if one uses a mesh that is too small, the resulting numbers may be good enough for use in a practical device but they may not be accurate enough for detailed interpretation or extrapolation.

It is true that calculations that use the Runge-Kutta routine often use a version where the step size is variable, but it is difficult to see how this change will have a very large effect on the number of steps, in this case, two or three orders of magnitude.

(In subsequent calculations we were able to show that the computational difficulty was the result of using equation 1 for the Runge Kutta routine, instead of equation 4. When the latter was used, the number of steps required was reduced by a factor of 50.)

In view of these considerations the results that follow were obtained using large numbers of steps. For $1.25 \geq V_1 \geq .8$ we used 100,000 steps. For all other cases, we used 5,000 steps. The complete results are shown in Table 3. It will be seen that the agreement with the asymptotic values is very good indeed. The value of C_s varies over 9 orders of magnitude but the value of C_s / f^3 varies very little, barely a factor of 1.5. Similarly, while the focal length varies by almost three orders of magnitude, the value of C_c / f varies by only a factor of two. Perhaps equally important is the fact that $f(\ln V_1)^2$ is very closely equal to 1 throughout this whole range. This agreement seems to confirm the idea that the asymptotic values do not depend very heavily on the particular form of the potential since the impulse approximation that we used is quite different from the potential used in the calculations.

It is interesting that the agreement for the expected value of C_c can be improved if we multiply by $\sqrt{V_1}$. This is admittedly arbitrary and without justification, but it is the only empirical adjustment that we indulge in.

In Fig. 1 we present the same results and plot them as ratios with the asymptotic values for V_1 from .2 to 4. This covers the whole range af operation where the focus is outside the lens. It seems clear that the performance of the symetrical Einzel lens can be estimated with good accuracy without having to perform any extended calculations. The asymptotic values are almost good enough.

The focal length of the lens remains very close to the asymptotic value throughout the whole range of values of V_1 and passes through infinity ($V_1 = 1$) very smoothly. More surprising is that the spherical and chromatic aberration coefficients also pass very smoothly through the same point. There are some minor perturbations in the case of the spherical aberration, but these are probably due to lack of precision and perhaps the number of steps was still too low.

The T Formulation

The simple polynomial for the potential distribution is attractive because of its simplicity but it should be noted that this simplicity disappears when the potential is introduced into the differential equation. In that case, the ratios that are involved become infinite series. While this is not important in

numerical calculations, it is nevertheless troublesome. If we use the T notation, we have already seen that the equations are simplified, and this encourages us to hope that the use of a simple expression for T will lead to other simplifications and perhaps improvements. If we use a simple polynomial for T and apply all our boundary conditions, the simplest function that can be formulated is

$$T = 32z(1-z)(1-2z)lnV_1 \tag{16}$$

and then the potential itself is

$$V = \exp(\ln V_1(4\ z\ (1-z)^2)\ ) \tag{17}$$

Using this potential we repeated all the previous calculations in order to determine whether this change would make any substantial difference. The results of the calculations are given in Table 4. and plotted in Fig 2. It can be seen that there is no substantial difference between these results and the previous ones. The only difference of any consequence is that this lens is better at short working distances in the accelerating mode.

Once again, the three curves pass smoothly through $V_1 = 1$ and the deviations from the asymptotic values are small, although a little larger than in the previous case.

Other Fields

In order to test the sensitivity of these results to the shape of the potential distribution, we can readily try others. One simple way to proceed is to take the polynomial distribution and raise it to some higher power. For example, we can simply square that function.

$$V = 1-(1-V_1)(4\,z\,(1-z))^4 \tag{18}$$

The results of using this potential are given in Fig. 3 where it can be seen that this distribution does not appear to be as good as the simpler version of the polynomial, although the numerical values are surprisingly close.

The chromatic aberration appears to be slightly better for short focal lengths in the decellerating mode but the spherical aberration is considerably worse. In the accelerating mode, the spherical aberration improves and the chromatic aberration becomes worse. It is interesting to note that in all cases, the results are very close to the predicted asymptotic values, in general within a factor of two.

Discussion

The most significant result of all these calculations is that the properties of the symmetrical Einzel lens do not depend very much on the shape of the potential distribution and that we can give very simple approximations to these properties that are good to a factor of two throughout the whole range of practical values of the potential. In fact, if these results are found to obtain for all shapes of the potential, it would appear that there is very little purpose to be served in pursuing design principles any further. The only purpose of performing calculations on any system would be to find the relationship between the potential on the central electrode and the potential on the axis at the center of the lens. Given this relationship, all other properties are known within a factor of two, which is generally good enough.

If it is necessary to know the aberration coefficients more precisely and if we wish to obtain the lowest possible values, these results appear to indicate that the best lens would be the one with the simplest form in the function T. This might be expected from the form of the equations because adding more terms to the polynomial would mean higher powers of z and these would appear to complicate the problem, not improve it.

If we assume that this analysis is correct, it is of some interest to examine the equipotentials to see how we could make such a lens. In Fig. 5 we show these equipotentials. These were obtained by using the poynomial for the potential along the axis and expanding it as a function of the radius r

$$V(r,z) = V(0,z) - (\frac{r^2}{4})V(0,z)'' + (\frac{r^4}{64})\ V(0,z)'''' + \ldots . \qquad (19)$$

The upper figure shows the equipotentials for the simple polynomial for V. The expansion was carried out to the fourth order only because, of course, there are no higher derivatives. It will be appreciated that the minor discontinuities in the curves are artifacts of the contour computation. In computing these contours, V_1 was set equal to 0.5 and the contours are plotted in intervals of 0.1. The lens could be fabricated by replacing the two ends with equivalently shaped electrodes, while any of the equipotentials for $V_1 \leq 0.5$ could be used for the central electrode. It is very likely that any reasonable approximation to these curves would suffice.

The lower curve shows the equipotentials for the simple polynomial for T. In this case, the expansion was carried out to the sixth order in r. It can be seen that the shapes are very different from the previous case, even though the electron optical properties are quite similar. In general, the central electrode is thicker and the field strength in the vicinity of the electrodes is obviously higher. In practice, this will mean that the electrodes will need to be further apart, and this means that the lens will be physically larger, which will negate any advantage of this " T " lens.

Conclusions

These calculations indicate that we can predict the first and third order optical properties of this type of lens by using just two parameters, the physical length of the lens and the potential on the axis at the mid-point. Given these two numbers, all the properties are given by very simple expressions and the results are good to a factor of two. The best lens appears to be the simplest one and could be made by

using some reasonable approximation to the equipotential curves shown in Fig. 5. This characterization of lenses is much simpler than previous ones, which for the most part use the diameter of the hole in the central electrode, a dimension which does not seem to have any real significance.

The calculations have a great deal of internal consistency and the need for a very large number of steps in the ray-tracing routine would seem to throw some doubt on previous calculations of this type, since few people have had the patience or the computational power to perform such lengthy calculations. It is only with the advent of inexpensive computations that these discrepancies have become apparent.

It would appear now that the properties of this type of lens can be easily estimated and that the only real purpose in performing numerical calculations of the internal potential distribution would be to obtain accurate information on the relationship between the potential on the central electrode and the potential on the axis at the mid-point. If the potential to be placed on that electrode is unimportant or is an adjustable parameter, then any convenient hole diameter would suffice. There is an indication that longer central electrodes with smaller gaps between them and the outer electrodes would be preferable if shorter focal lengths are needed. On the other hand , if smaller gaps can be tolerated, it might be possible to make smaller lenses.

As one final note, we should emphasize the simple scaling properties of the lens and the equations. All dimensions scale linearly so that doubling the length of the lens also doubles the focal length and the two aberration coefficients. For any arbitrary electron energy, the values of V_1 given here can be used as a multiplying factor to calculate the potential on the axis at the center of the lens.

Acknowledgements

The author would like to express his gratitude to Lester Su, who performed some preliminary calculations in this field and whose tentative results stimulated this work. This work was supported by a grant from the Department of Energy no. DE-FG02-86-ER60437. The author wishes to thank IBM Corporation for their support in this work.

References

(1) P. Grivet. 'Electron Optics' Pergamon Press. Oxon. (1965), 8455.

(2) G. Liebmann. *Proc. Roy. Soc.*(London) B **62**, (1949), 212.

(3) E. Regenstreif. *Ann. Radioel.* **6**, (1951), pp. 51-164.

(4) W. Lippert & W. Pohlit. *Optik*, **9**, (1952), 456.

(5) G. Kempfer. *J. Appl. Phys.* **57**, (1985), 2385.

(6) A.B. El Kareh, J.C.J. El Kareh, *Electron Beams, Lenses and Optics* Academic Press. N.Y. (1970), p 83.

(7) C.Fert and P.Durandeau *Focusing of Charged Particles* Academic Press. N.Y. (1967), p 309.

Table 1.

The calculated values of the focal length and the aberration coefficients are significantly affected by the number of steps that are used in the Runge-Kutta routine. The results given here are for a short focal length. The central voltage is just one half of the initial voltage. It can be seen that we need at least 1000 steps for good precision.

Table 1

	$V_1 = 0.5$		$L = 1$					
steps	10	50	100	500	1000	5000	10000	50000
f	1.41	1.94	2.14	2.38	2.42	2.45	2.45	2.45
$\frac{Cc}{f}$	.96	1.97	2.29	2.62	2.67	2.71	2.72	2.72
$\frac{C_s}{f^3}$	5.84	12.1	14.3	16.8	17.2	17.5	17.5	17.5

Table 2.

Similar to Table 1 except that these results are for a long focal length, where the central voltage is 0.95 times the initial voltage. In this case, good precision is only obtained when the number of steps exceeds 50,000.

Table 2

$V_1 = 0.95$ $L = 1$

steps	10	50	100	500	1000	5000	10000	50000	100000
f	21.5	59.7	100	251	313	391	404	414	416
$\frac{C_c}{f}$	-.08	.27	.48	1.23	1.54	1.92	1.98	2.03	2.03
$\frac{C_s}{f^3}$	.70	2.45	4.17	10.5	13.1	16.4	16.9	17.4	17.4

Table 3.

Complete results for the potential distribution of equation 15. V_1 is the voltage at the mid-point of the lens, z is the position of the focus for a parallel incoming beam, f is the focal length and C_s, C_c are the aberration coefficients that are obtained from the ray-tracing calculation. If the asymptotic expressions were correct everywhere, the remaining rows would have a value of exactly 1. It can be seen that the approximation is surprisingly good.

Table 3

V_1	.2	.3	.4	.5	.6	.7	.8	.9	.95	1.05	1.1	1.2	1.5	2	3	4
z	1.01	1.37	1.94	2.93	4.86	9.25	22.7	99.3	416	461	121	33.4	7.28	2.89	1.5	1.14
C_S	4.91	15.5	57.7	255	$1.4.10^3$	$1.1.10^4$	$1.9.10^5$	$1.7.10^7$	$1.2.10^9$	$1.7.10^9$	$3.1.10^7$	$6.2.10^5$	$5.4.10^3$	230	21.9	11.4
C_c	2.41	3.1	4.38	6.64	10.9	20.5	49.3	207	848	902	230	60.1	11.1	3.30	1.14	.74
f	.58	.91	1.46	2.45	4.36	8.75	22.2	98.8	416	460	120	32.9	6.79	2.41	1.08	.79
$C_S/20f^3$	1.28	1.02	.90	.88	.86	.85	.87	.87	.87	.88	.88	.87	.86	.83	.87	1.14
$C_c/2f$	2.1	1.7	1.49	1.36	1.25	1.17	1.11	1.05	1.02	.98	.96	.92	.82	.68	.53	.47
$\frac{C_c\sqrt{V_1}}{2f}$	.93	.93	.95	.96	.97	.98	.99	.99	.99	1.00	1.00	1.00	1.00	.97	.91	.94
$f.\ln^2 V_1$	1.5	1.31	1.23	1.18	1.14	1.11	1.10	1.09	1.09	1.10	1.09	1.09	1.11	1.16	1.30	1.53

Table 4.

Similar to the results given in Table 3 except that the potential distribution was that given in equation 17. Once again, the asymptotic expressions are surprisingly good.

Table 4

V_1	.2	.3	.4	.5	.6	.7	.8	.9	.95	1.05	1.1	1.2	1.5	2	3	4
z	1.02	1.38	1.94	2.92	4.82	9.18	22.6	99	415	462	121	33.6	7.37	2.94	1.55	1.19
C_s	5.20	13.7	51.9	242	$1.4.10^3$	$1.1.10^4$	$1.9.10^5$	$1.7.10^7$	$1.3.10^9$	$1.7.10^9$	$3.0.10^7$	$6.0.10^5$	$4.9.10^3$	192	13.8	4.70
C_c	2.43	2.99	4.23	6.45	10.7	20.1	49.0	207	847	904	231	60.4	11.2	3.34	1.14	.68
f	.65	.95	1.48	2.44	4.33	8.68	22.1	98.5	415	462	121	33.1	6.88	2.46	1.09	.78
$C_{S/20f^3}$	.94	.80	.80	.84	.86	.88	.89	.89	.88	.87	.86	.84	.76	.65	.52	.50
$C_c/2f$	1.87	1.58	1.43	1.33	1.24	1.26	1.11	1.05	1.02	.98	.96	.97	.82	.68	.52	.44
$\frac{C_c\sqrt{V_1}}{2f}$	.84	.86	.90	.93	.96	.97	.99	1.00	1.00	1.00	1.00	1.00	1.00	.96	.91	.88
$f.\ln^2 V_1$	1.69	.68	.62	1.17	1.13	1.10	1.10	1.09	1.09	1.10	1.10	1.10	1.13	1.18	1.32	1.49

Figure 1.

This figure gives the same data as Table 3, but in graphical form. The functions plotted are

$$f \ln(V_1)^2 \ (F) \quad ; \quad \frac{C_s}{20f^3} \ (S) \quad ; \quad C_c \frac{\sqrt{V_i}}{2f} (C)$$

It can be seen that the asymptotic value of 1 for each of these quantities is a very good approximation throughout the whole range.

POLYNOMIAL IN V

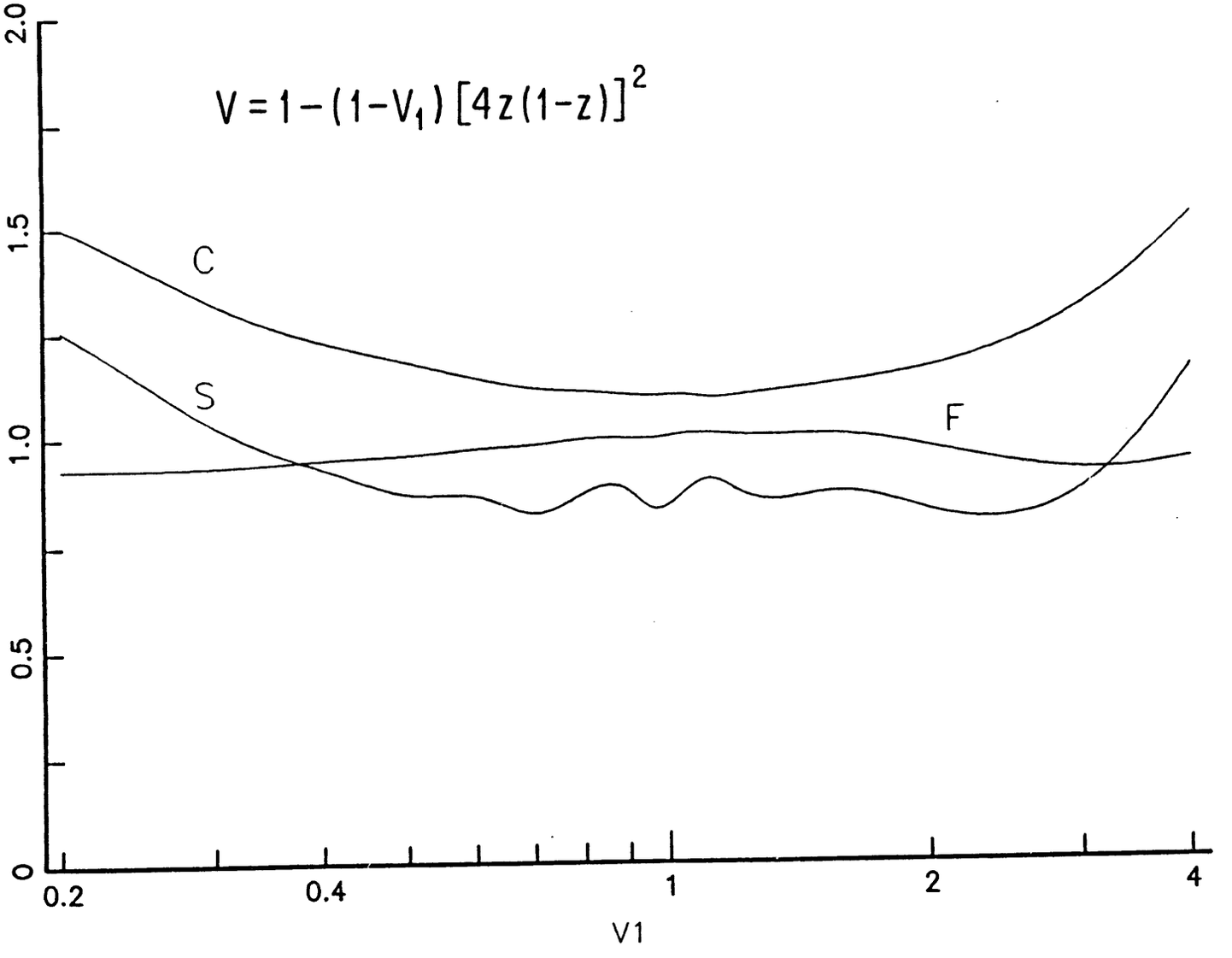

Figure 2.

This is similar to Fig. 1 except that the potential distribution corresponds to equation 17 instead of equation 15. Once again, the asymptotic expressions are very good approximations.

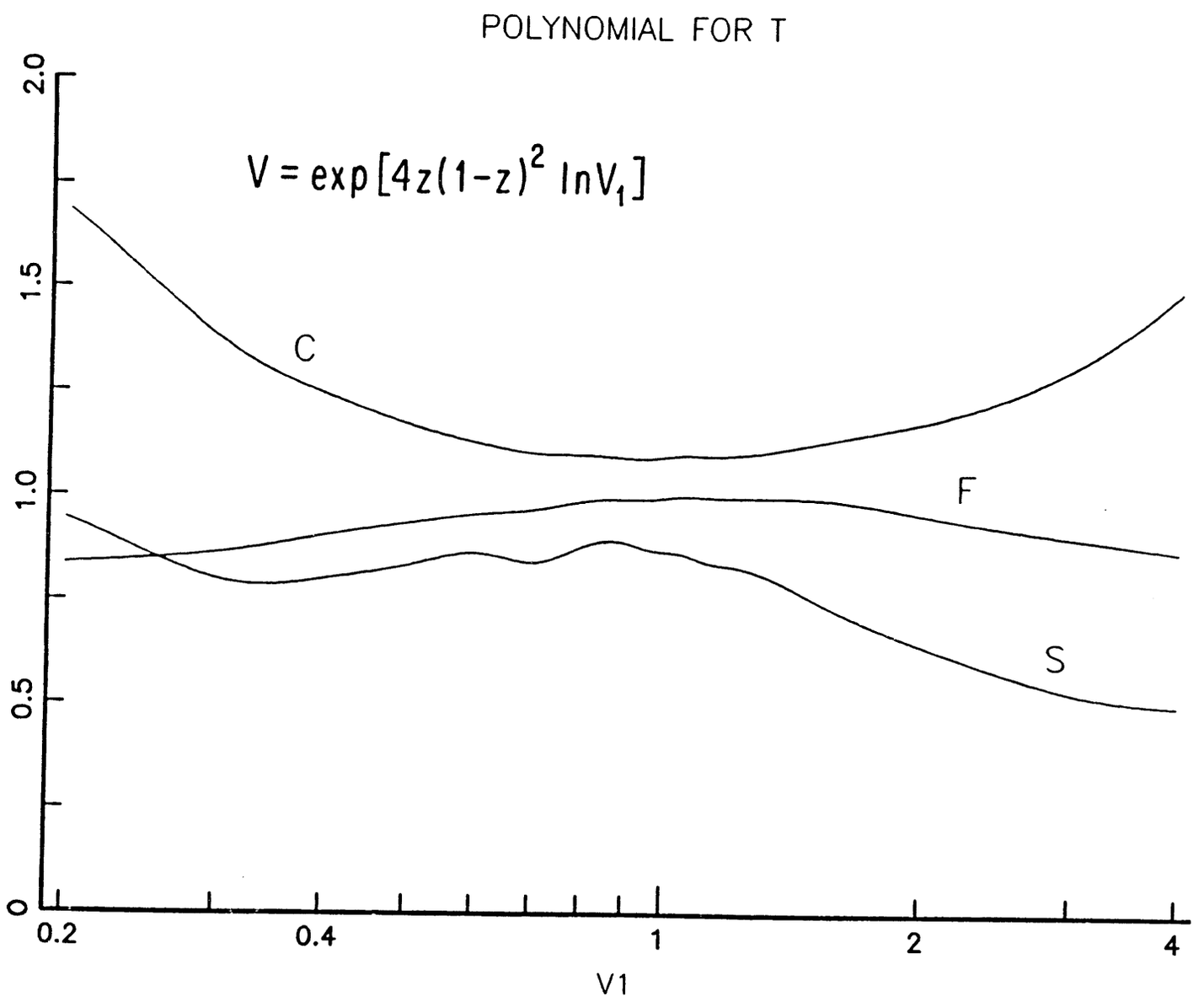
POLYNOMIAL FOR T
$V = \exp[4z(1-z)^2 \ln V_1]$
C
F
S
2.0
1.5
1.0
0.5
0
0.2
0.4
1
2
4
V1

Figure 3.

In this case, the potential distribution corresponds to equation 18. Again, the approximations are very good, considering the very large range af values for the parameters.

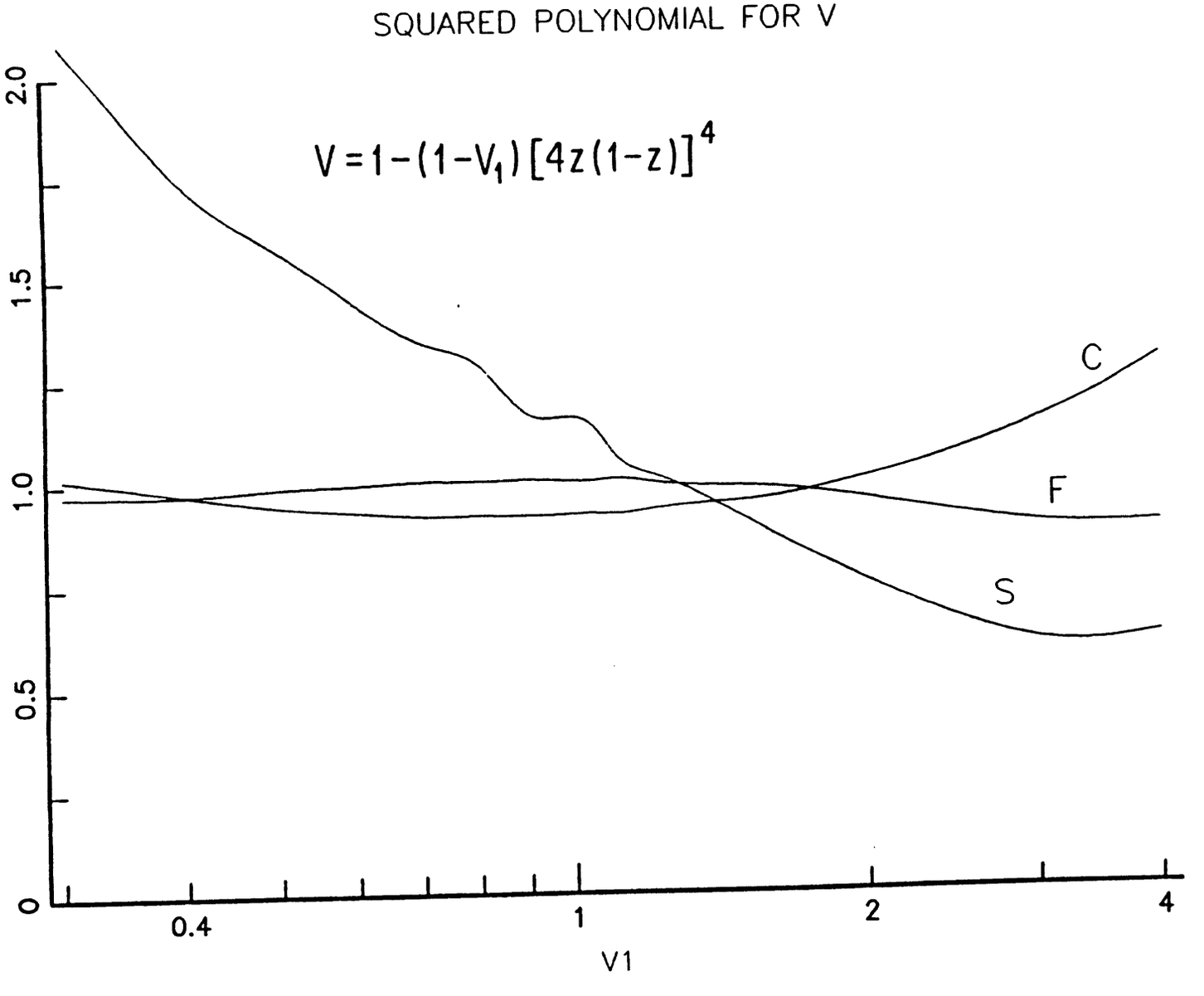
SQUARED POLYNOMIAL FOR V
$V = 1-(1-V_1)[4z(1-z)]^4$
2.0
1.5
1.0
0.5
0
C
F
S
0.4
1
2
4
V1

Figure 4.

This figure shows the equipotentials corresponding to the potential distributions that were used in the calculations. Fig. 4a gives the equipotentials for equation 15 and Fig. 4b gives those for equation 17. The value of V_1 was set at 0.5 and the equipotentials are in intervals of 0.1.

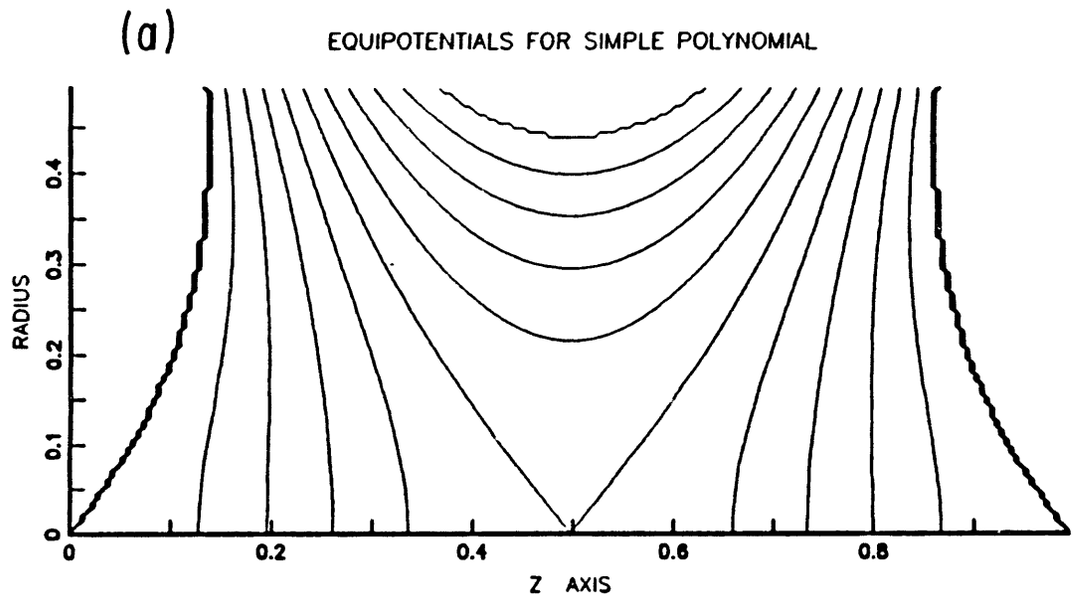
(a)
EQUIPOTENTIALS FOR SIMPLE POLYNOMIAL
RADIUS
0
0.1
0.2
0.3
0.4
0
0.2
0.4
0.6
0.8
Z AXIS

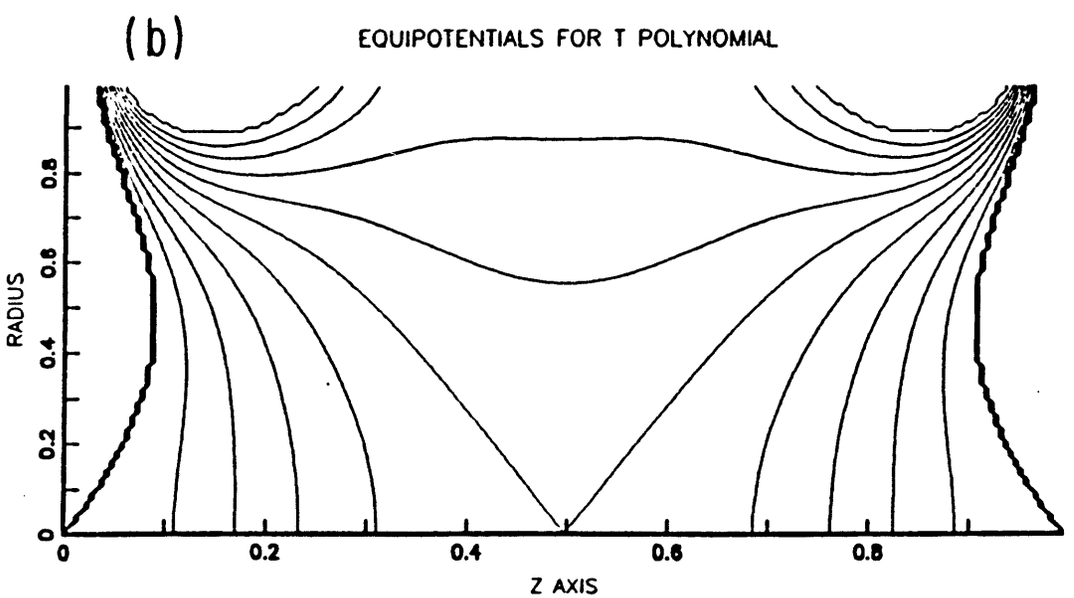
(b)
EQUIPOTENTIALS FOR T POLYNOMIAL
RADIUS
0
0.2
0.4
0.6
0.8
0
0.2
0.4
0.6
0.8
Z AXIS

The Three Element Electrostatic Lens

Introduction

The three element lens is the most common form of electrostatic lens and is very widely used. The properties of these lenses have been widely discussed in the literature (e.g. 1,2) but there is surprisingly little understanding of their characteristics. While it is possible to calculate the relevant performance parameters for any given lens, there are few, if any, general guidelines for designing a lens for a specific purpose. In general,the published work consists of calculations on specific geometries or compilations of numerical data obtained theoretically or experimentally (e.g. 3,4). The published work does not allow one to consider these lenses as a group or as a general component in an optical system, and in fact, even the dependence of the focal length on the physical dimensions and the voltages is not easily understood.

This state of affairs is not surprising since even the simplest three element lens requires knowledge of three voltages, corresponding to the energy of the electron at the entrance and the exit of the gun, together with a focussing voltage. In addition, with regard to the physical dimensions, even in the simplest lens, there are at least eight to be chosen, the thickness of each electrode, the three hole diameters and two electrode spacings. In the event that electrode shapes other than flat plates are to be used, there would be even more numbers to be fixed. All this complication has made it difficult to characterize these lenses or even to simplify the discussion so that general tendencies can be perceived.

The purpose of this paper is to attempt to provide the insight necessary for such general thinking, even at the expense of precision. In a previous paper (5), we succeeded in simplifying the approach to a particular form of this lens, the symmetrical einzel lens, but now we will try to generalize that approach, and include the effect of acceleration of the electrons.

The method that we use has been found to be useful in many other areas of physics. It consists of simplifying the problem by looking at general tendencies as the functions approach some limit or other. By doing this it is often possible to extract from the problem some trivial but annoying factors which can obscure the overall picture. Such is the case, for example, in nuclear or particle physics where it is highly desirable to separate out dynamical and symmetry factors, thereby leaving only the essentials.

In our case, the situation is complicated by the rapid dependence of the desired properties (such as the focal length and the aberrations) with the applied voltages. This often requires plotting the final results of the calculations or the measurements on logarithmic plots over many decades of values, making it difficult if not impossible to interpret the data and certainly making it very difficult to obtain accuracy. We hope to show that by using the asymptotic dependencies as a guide, we can present the data for any given lens in a much more slowly varying form.

In the previous paper, we found it convenient and instructive to use the Picht transformation and to put the equations of motion in the " T " form, that is by using the variables

$$T = \frac{V'}{V} \qquad ; \qquad R = rV^{\frac{1}{4}} \tag{1}$$

where r is the radius, -eV is the electron energy and the derivative are with respect to z, the distance along the axis. Then the equations become very much simpler. The first order equation becomes:

$$R'' = -\frac{3}{16}T^2R \tag{2}$$

and the expressions for the two aberration coefficients are:

$$C_s = \frac{1}{16r_0'^4}\int\left[\left(\frac{5}{4}T'^2 + \frac{5}{2}T'T^2 + \frac{35}{24}T^4\right)r^4 + \frac{14}{3}T^3r'r^3 - \frac{3}{2}T^2r'^2r^2\right]\sqrt{\frac{V}{V_0}}\,dz \tag{3}$$

$$C_c = \frac{1}{r_0'^2}\int\frac{3}{8}T^2\,r^2\sqrt{\frac{V_0}{V}}\,dz \tag{4}$$

In these expressions, the subscript 0 refers to conditions in the image space.

We recognize, of course, that these integrals are given here in "mixed" form, that is, using T and r instead of R, but this particular form will be found to be useful later. The first order equation of motion is now particularly pleasant and is in the same form as that for magnetic lenses so that the function T plays the same role as the magnetic field strength (normalized to the momentum). We can therefore expect lenses of the same shape in those functions to behave similarly.

With regard to the aberration integrals, we now propose to look at the asymptotic behaviour in the limit of very weak lenses. In that case, there is no change in the value of the radius r as the electron passes through the lens and in addition the change in the voltage must be small. It is easiest to consider an entering ray which has unit radius and zero slope. The focal length f can then be obtained directly from the change in the slope. Then, in the limit, the equations reduce to

$$\frac{1}{f} = \left(\frac{V_i}{V_0}\right)^{\frac{1}{4}}\frac{3}{16}\int T^2dz \tag{5}$$

$$C_s = \frac{5f^4}{64}\int T'^2\sqrt{\frac{V}{V_0}}\,dz \tag{6}$$

$$C_c = \frac{3f^2}{8}\int T^2\sqrt{\frac{V_0}{V}}\,dz \tag{7}$$

where the integral is taken over the complete region between image and object. The subscript *i* refers to the conditions at the entrance to the lens.

There is an obvious and pleasing pattern to these integrals, leading us to hope for some simple relationships between them. In order to proceed any further, however, we must make some assumptions about the function T.

The Choice of the Function T

In the limit of a very weak lens we are representing the lens by a simple impulse. In this case, the precise form of the function T is probably not very important. All reasonable choices should give approximately the same answer. In view of this, it is reasonable to look for the simplest function that will work.

In previous work, we have found that the conditions near the various apertures in the system can have profound effects. Near these apertures, the field strength can be small but somewhat indeterminate and it often happens that the energy of the electron is low and may be changing rapidly. In that case, the function T may be difficult to determine accurately. This may not represent a real problem, merely a mathematical inconvenience, but it does interfere with the calculations. In this paper, we will specify the function T and will take care to set it to zero outside the range of integration. In practice this means that the field strength must go to zero at some known location, This condition can be realized in the real world by shaping the electrodes near the entrance and the exit apertures of the lens. Since it is easy to do this and since it is in any case a good thing to do, we can incorporate this principle into the function T.

The central electrode of the lens is the one that provides the additional focusing action. This electrode need not be in the exact center of the lens and the potential may increase or it may decrease in the vicinity of the electrode. This makes it dificult to simulate the electrode mathematically. In order to define the field, we take the simplest approach, which is to specify the potential at the midpoint of the lens. Taking this into account, we are looking for a description of the field that will satisfy the following conditions:

1. The function T must equal zero at $z=0$ and $z=1$.

2. We make the potential V equal to 1 at $z=0$ and equal to V_0 at $z=1$

3. The value of the potential at the midpoint of the region is V_1

The conditions on the potential then correspond to

$$\ln V_0 = \int_0^1 T dz \qquad \ln V_1 = \int_0^{\frac{1}{2}} T dz$$

The simplest way to choose a function for T is to use a polynomial in z and the most elementary one that satisfies all the conditions above is

$$T = \ln V_1\left(32z - 96z^2 + 64z^3\right) + \ln V_0\left(-10z + 42z^2 - 32z^3\right) \tag{8}$$

In spite of the fact that this expression looks complicated, it is in fact, a perfectly reasonable and practical lens. It could be fabricated by choosing the desired operating conditions, plotting the equipotentials and then replacing three of the equipotentials by conductors at the appropriate potential. In general, the equipotentials have very simple shapes, and usually the field can be reproduced by using three electrodes, but in the case of very high voltage ratios, four electrodes may be needed.

Asymptotic Behaviour

If we insert this expression for T into the three asymptotic integrals, we can calculate the focal length and the aberration coefficients. In principle, this could be done exactly, using numerical values, but we are more interested in analytical methods and here the presence of the square root in the integral presents a problem, and we must make some approximations.

The Focal Length

The integral for the focal length can be readily performed. The result is

$$\frac{1}{f} = \left(.453\,(\ln V_0)^2 + .914\,(\ln V_1)^2 - .914 \ln V_1\ \ln V_0\right)\ V_0^{-\frac{1}{4}} \tag{9}$$

In order to simplify the expression a little and to make it easier to compare it with the results in the previous paper for the einzel lens, we make a small approximation and rearrange the terms

$$f = \frac{1.09\ V_0^{\frac{1}{4}}\ I(V_0, V_1)}{(\ln V_1)^2\left(1 - \rho + .5\rho^2\right)} \tag{10}$$

where

$$\rho = \left(\frac{\ln V_0}{\ln V_1}\right) \tag{11}$$

and we have introduced a new function $I(V_0, V_1)$ which we expect to be very nearly equal to unity for the particular potential distribution that we have chosen, but which could be quite different for other distributions. We expect that this function will be slowly varying and will contain all the characteristics of any particular lens. The general characteristics of the lens are included in the explicit dependencies that are shown.

This result compares very well with that for the focal length of the einzel lens

$$f = \frac{1.06}{(\ln V_1)^2} \tag{12}$$

because in that case, $V_0 = 1$ and $\rho = 0$. Note that the focal length is given as a multiple of the length of the lens, which we have set to unity in order to simplify the calculation.

This comparison also shows the effect of the overall acceleration. The lens is always focusing and is weakest when $\rho = 1$ and then $V_1 = V_0$. Additional focusing will occur whenever this condition does not hold. This additional focusing will be present whether V_1 is greater or less than V_0. The properties of the lens are illustrated in Fig. 1 where we plot the function:

$$f\, V_0^{-\frac{1}{4}} \tag{13}$$

for various values of the two voltages in the range from .05 to 10 and assuming that the correction function is equal to one, as it should be for this lens.

This contour plot illustrates the symmetry of the lens action. For any given acceleration (V_0) there is a restricted range of focal lengths available and there are two possibilities for obtaining any given focal length. These correspond to an increase or a decrease in the potential of the electrons, normally called the accelerating and the decelerating modes. Long focal lengths can only be obtained when the acceleration is small.

By using this logarithmic plot, the contours are smooth and elliptical in shape. The contour plot is very simple and the lens action is easy to understand. It might be argued that this simple result is due to the particular choice of the function T, but the general features are surely universal. This makes it difficult to understand why these relationships have not become apparent in previous publications.

The Spherical Aberration

The integral for the coefficient of spherical aberration is difficult to evaluate because of the presence of the square root. In fact, if we are to use the particular function that we have chosen for T, the integral cannot be done. However, we recall that we only expect the integral to be valid for the case of very weak lenses. In that case, the electron energy does not change very much in passing through the lens and the square root has a value that is always close to unity.

This means that we can obtain an approximate value for the integral by assuming, for example, that $V = V_1$. This is true, of course, for only one point in the lens, but it is approximately true over a large region. In any case, the value of the integral must depend upon V_1 and the functional characteristics should correspond to those obtained by taking the square root out of the integral. There is no real justification for doing this, but we can hope that the result will contain all the necessary dependences on the parameters of the problem. Making this approximation, the result is:

$$C_s = 16 f^4 (\ln(V_1)^2)\left(1 - \rho + .3\rho^2\right)\sqrt{\left(\frac{V_1}{V_0}\right)} \qquad (14)$$

The expression in parenthesis is quite close to the one that occurs in the expression for the focal length, well within a factor of two for all except extreme cases. This makes it tempting to write

$$C_s = 17.5 f^3 V_0^{-\frac{1}{4}} V_1^{\frac{1}{2}} m(V_0, V_1) \qquad (15)$$

Where we hope that the major features are spelled out explicitly, leaving a correction factor m which contains all the features particular to one lens only and might be expected to be a simple and slowly varying function, as in the case of the expression for the focal length. From the approximation made above, we would expect that the correction factor m would have a value of 0.6 at $\rho = 1$. If this expression is valid for the particular lens field that we have chosen, we would expect it to be valid for all fields. If so, it would represent a simple and convenient form in which to compare aberrations.

The expression for the spherical aberration is given for the case of a lens of unit length. For a lens of length L, the expression should be divided by L^2. In general, the expression is gratifyingly close to that which was obtained for the symmetrical einzel lens, where the numerical constant was 20 instead of 17.5, in spite of the fact that the potential function was quite different.

The Chromatic Aberration

If we make the same approximation as the one above for the integral for the chromatic aberration, we obtain:

$$C_c = 2 f V_0^{\frac{3}{4}} V_1^{-\frac{1}{2}} n(V_0, V_1) \qquad (16)$$

where we use a new function n to characterize the chromatic properties In general, the coefficient is nearly equal to twice the focal length.

The Calculations

Having established the asymptotic expressions for the focal length and the two aberration coefficients, we now compare them to the results of more accurate calculations using the complete aberration integrals. Taking the contour plot of Fig. 1 as a guide, we selected values of V_0 and V_1 of .1, .2, .5, .9, 95, 1.05, 1.1, 2 ,5 and 10 as being adequate to cover the whole range of usefulness of the lens. This gives us a selection of 100 representative voltage pairs for the electrodes.

For each voltage pair we calculate the asymptotic values for the focal length and the two aberration coefficients, using equations (10), (15) and (16) given above and assuming that the correction functions are equal to one.

Next, we performed a ray-tracing of the first order equation of motion, using the fourth order Runge-Kutta method and using 25,000 points for each trace. This was found to give reasonably accurate results in the previous work, at least good to 5% or so. Using an input ray of unit amplitude and zero slope, the focal length can easily be determined from the slope of the output ray. In addition, the amplitude and slope of all 25,000 points were saved and then used to evaluate the aberration integrals. By dividing the result of this integration by the asymptotic values, we can evaluate the three correction functions.

The calculations were performed using APL because this language is ideally suited for this purpose. It is very flexible and compact. In fact, the entire calculation is contained in only 50 lines of executable code.

Table 1 gives the result of the calculation for the focal length. In Table 1a we give the asymptotic value and in Table 1b we show the ratio between the focal length obtained from the ray-trace to the asymptotic value. This ratio is the correction function $l(V_0, V_1)$. It will be seen that the correction function is always close to unity, even for very small focal lengths. This is somewhat surprising in view of the severe approximations that have been made. The correction function shows no particular trends in the two axes, indicating that we have incorporated all the necessary functional dependencies into the equation for the focal length. What is left is due to the fact that we took the radius out of the integral and also we can presume that the effect of the special potential function that we have used is also included.

In Table 1 and all the other Tables, we present the data in the same geometrical relationship as in Fig.1. The horizontal axis is V_0 and the vertical axis is V_1. As noted above, however, the intervals are not equally spaced.

In Table 2, we give the corresponding results for the coefficient of spherical aberration. Table 2a gives the asymptotic value, and Table 2b gives the correction function. It can be seen that the coefficient varies widely, more than a factor of 10^{10} from the lowest to the highest values. In spite of these variations, the correction function remains reasonably close to unity, except for very short focal lengths. There are some special features of Table 2b that are worthy of note. The central values (near 1,1) are not equal to one and this is to be expected because of the approximation which was made. There are two anomolously low values (underlined) which we cannot explain. They do not appear to be due to calculational inaccuracies since they have appeared consistently and for several different ray-traces, using widely different numbers of points. Finally, it is evident that using the system in an accelerating mode, where V_1 has the higher of the two possible values for any given focal length, gives the lowest value for the aberration. This fact has been pointed out by other investigators.

The results for the coefficient of chromatic aberration are shown in Table 3. Here again, Table 3a gives the value for the asymptotic calculation and Table 3c gives the correction function. It will be noted that once again, the coefficient varies over a very wide range, in this case three orders of magnitude, while the correction function remains everywhere close to one.

Conclusion

A three element electrostatic lens can be characterized by three voltages, corresponding to the entrance energy of the electrons, the exit energy and the potential at the mid-point of the lens. In order to simplify the notation, we can take advantage of the fact that only the ratio of voltages is relevant. The absolute values do not appear in the equations. We therefore take the entrance energy to have value of one and call the other two V_0 and V_1. With regard to V_1, it is important to note that this is in general not the voltage that is applied to the focussing electrode, but, of course, there is a simple relationship between them. The lens will also have some characteristic length L. Using these parameters and also using the simplest potential distribution that will suffice for the problem, we have developed expressions for the three important properties of these lenses, the focal length and the coefficients of spherical and chromatic aberration. These expressions are based upon the values that these numbers would have for large focal lengths, which we take as a guide to the values elesewhere.

Recognizing that these asymptotic expressions cannot be valid everywhere, we incorporate correction factors into the equations. These correction factors will then include the effect of changes of the orbit radius within the lens and the particular geometry of the lens structure. By doing this, we effectively remove general tendencies from these factors making it possible to compare lenses with one another, using functions that are slowly and smoothly varying, instead of the wildly fluctuating coefficients themselves.

The focal length can be written as:

$$f = \frac{1.09\ L\ V_0^{\frac{1}{4}}}{(\ln\ V_1)^2(1\ -\ \rho\ +.5\rho^2)}\, l\ (V_0, V_1) \tag{17}$$

while the coefficient of spherical aberration is given by

$$C_s = 17.5\ L^{-2}\ f^3 V_0^{-\frac{1}{4}} V_1^{\frac{1}{2}}\ m\ (V_0, V_1) \tag{18}$$

and the coefficient of chromatic aberration is

$$C_c\ =\ 2\ f\ V_0^{\frac{3}{4}} V_1^{-\frac{1}{2}}\ n\ (V_0, V_1) \tag{19}$$

In these equations the three correction functions l, m, n are expected to remain close to unity and are represented in Tables 1c, 2c, 3c, for the case of the particular potential distribution that we used here. These functions are not expected to be very different for any other potential distribution.

Acknowledgements

The author would like to express his gratitiude to Dr. Oscar Kapp for his critical reading of the manuscript. This work was supported by a grant from the Department of Energy (DE-FG02-86-ER60437). The author would also like to express thanks to IBM Corporation for their support of this work.

References

(1) P. Grivet.*Electron Optics* Pergamon Press. Oxon (1965).

(2) K.-J. Hanszen and R.Lauer *Focusing of Charged Particles* ed. A. Septier. Academic Press (1967) p. 251

(3) W. Lippert and W.Pohlit *Optik*. 9 (1952), p. 456

(4) G. Rempfer. *J. Appl. Phys.* **57**, (1985), p. 2385

(5) A. V. Crewe Optik (in press)

Table 1.

(a) gives the result of the calculation for the focal length in the asymptotic approximation corresponding to equation (10). Table 1 (b) gives the ratio of the actual focal length obtained by ray tracing to the results given in Table 1(a). It therefore represents the correction factor $l(V_0, V_1)$. As we predicted, this ratio remains very close to one everywhere.

Table 1
A

V_1 \ V_0	0.1	0.2	0.5	0.9	0.95	1.05	1.1	2	5	10
0.1	-	-	-	-	-	-	-	-	-	-
0.2	-	-	-	0.384	0.402	0.439	0.457	0.756	1.26	1.26
0.5	-	0.252	0.763	1.9	2.08	2.46	2.66	5.4	2.47	1.26
0.9	0.213	0.5	2.91	43	70.4	196	246	7.07	1.42	0.794
0.95	0.222	0.53	3.32	81.2	174	927	491	6.21	1.34	0.763
1.05	0.242	0.6	4.42	382	818	174	92.5	4.66	1.18	0.699
1.1	0.253	0.641	5.14	191	153	63.3	43.5	4	1.1	0.667
2	0.399	1.1	3.82	2.57	2.41	2.14	2.03	1.08	0.564	-
5	0.399	0.563	0.534	0.438	0.429	0.413	0.406	-	-	-
10	-	-	-	-	-	-	-	-	-	-

B

V_1 \ V_0	0.1	0.2	0.5	0.9	0.95	1.05	1.1	2	5	10
0.1	-		-	-	-	-	-	-	-	-
0.2	-	-	-	1.6	1.57	1.53	1.51	1.28	1.12	1.16
0.5	-	1.39	1.18	1.09	1.09	1.07	1.07	1.03	1.09	1.16
0.9	1.27	1.14	1.04	1.01	1.01	1.01	1.02	1.03	1.1	1.22
0.95	1.26	1.13	1.03	1.01	1.01	1.03	1.02	1.03	1.11	1.23
1.05	1.23	1.11	1.03	1.02	0.998	0.997	1	1.03	1.13	1.26
1.1	1.21	1.1	1.03	1.01	0.998	1	1	1.04	1.14	1.28
2	1.16	1.09	1.03	1.07	1.07	1.08	1.09	1.18	1.39	-
5	1.16	1.12	1.28	1.5	1.53	1.57	1.6	-	-	-
10	-	-	-	-	-	-	-	-	-	-

Table 2.

In this Table, we give the results of the calculations for the coefficient of spherical aberration C_5. In Table 1(a) we give the results obtained for the asymptotic approximation corresponding to equation (15) and in Table 2(b) we give the ratio of the value obtained from ray tracing to the corresponding value in Table 2(a). This then is the correction function $m(V_0, V_1)$ Although not as good as the predictions for the focal length, the ratio is not far from one, except at very short focal lengths. The two anomolous values (.267 and .241) are not understood.

Table 2

A

V_1 \ V_0	0.1	0.2	0.5	0.9	0.95	1.05	1.1	2	5	10
0.1	-	-	-	-	-	-	-	-	-	-
0.2	-	-	-	2.27E0	2.58E0	3.27E0	3.65E0	1.42E1	52.2	44.3
0.5	-	0.593	13.1	1.74E2	2.26E2	3.66E2	4.57E2	3.27E3	249	28
0.9	0.315	3.43	536	1.50E6	6.48E6	1.37E8	2.66E8	5.46E3	34.9	5.17
0.95	0.347	3.99	777	9.86E6	9.50E7	1.41E10	2.08E9	3.61E3	28.7	4.48
1.05	0.429	5.5	1750	9.78E8	9.46E9	8.95E7	1.32E7	1.45E3	18.8	3.28
1.1	0.48	6.55	2680	1.19E8	6.08E7	4.16E6	1.33E6	8.91E2	15	2.77
2	1.4	24.9	817	2.16E2	1.76E2	1.20E2	1.00E2	1.31E1	1.48	-
5	0.886	2.09	1.42	6.73E-1	6.25E-1	5.46E-1	5.12E-1	-	-	-
10	-	-	-	-	-	-	-	-	-	-

B

V_1 \ V_0	0.1	0.2	0.5	0.9	0.95	1.05	1.1	2	5	10
0.1	-	-	-	-	-	-	-	-	-	-
0.2	-	-	-	1.09	1.04	0.943	0.904	0.542	0.288	0.211
0.5	-	1.15	0.754	0.668	0.66	0.645	0.636	0.403	0.129	0.148
0.9	1.61	1.05	0.822	0.905	0.947	0.902	0.618	0.401	0.422	0.538
0.95	1.59	1.05	0.805	0.868	0.945	0.658	0.241	0.468	0.466	0.596
1.05	1.56	1.03	0.733	0.267	0.633	0.936	0.868	0.611	0.573	0.743
1.1	1.54	1.02	0.669	0.677	0.988	1.03	0.984	0.685	0.639	0.837
2	1.22	0.639	1.07	1.68	1.69	1.7	1.7	1.7	2.24	-
5	2.16	2.62	4.87	8.09	8.51	9.37	9.8	-	-	-
10	-	-	-	-	-	-	-	-	-	-

Table 3.

In this Table we give the results of the calculation for the coefficient of chromatic aberration. Table 3(a) again gives the result of the asymptotic approximation and Table 3(b) gives the correction factor $n(V_0, V_1)$

Table 3
A

V_1 \ V_0	0.1	0.2	0.5	0.9	0.95	1.05	1.1	2	5	10
0.1	-	-	-	-	-	-	-	-	-	-
0.2	-	-	-	0.317	0.346	0.407	0.439	1.14	3.76	6.5
0.5	-	0.107	0.642	2.48	2.83	3.61	4.05	12.8	11.7	10
0.9	0.072	0.285	3.3	75.8	129	388	503	22.7	9.03	8.52
0.95	0.079	0.309	3.85	146	326	1880	1030	20.4	8.73	8.37
1.05	0.082	0.368	5.39	725	1620	371	204	16.1	8.1	8.07
1.1	0.095	0.404	6.44	373	311	138	98.4	14.2	7.79	7.91
2	0.201	0.934	6.42	6.72	6.56	6.28	6.15	5.13	5.33	-
5	0.317	0.753	1.42	1.81	1.85	1.92	1.95	-	-	-
10	-	-	-	-	-	-	-	-	-	-

B

V_1 \ V_0	0.1	0.2	0.5	0.9	0.95	1.05	1.1	2	5	10
0.1	-	-	-	-	-	-	-	-	-	-
0.2	-	-	-	1.4	1.38	1.36	1.35	1.23	1.12	1.02
0.5	-	1.92	1.32	1.06	1.05	1.02	1.01	1	0.71	0.559
0.9	2.84	2.14	1.39	1.06	1.03	1.02	1.02	0.767	0.585	0.54
0.95	2.85	2.15	1.4	1.06	1.04	1.04	0.997	0.763	0.589	0.548
1.05	2.88	2.15	1.39	1.05	0.987	0.97	0.958	0.766	0.602	0.569
1.1	2.88	2.14	1.38	1	0.996	0.977	0.963	0.771	0.611	0.583
2	2.55	1.72	1.07	1.03	1.02	1	0.996	0.877	0.801	-
5	1.38	1.14	1.17	1.27	1.28	1.3	1.32	-	-	-
10	-	-	-	-	-	-	-	-	-	-

Figure 1.

This contour plot shows the behaviour of the quantity $fV_1^{\frac{1}{4}}$ as a function of the two applied voltages, V_0 and V_1 using equation (10). The contours are ellipses and the action of the lens is readily understood. The net acceleration can be positive ($V_0 > 1$) or negative ($V_0 > 1$) and for any given V_0 the focussing provided by the middle electrode can be in the accelerating (upper portion of the ellipse) or decelerating (lower portion) mode.

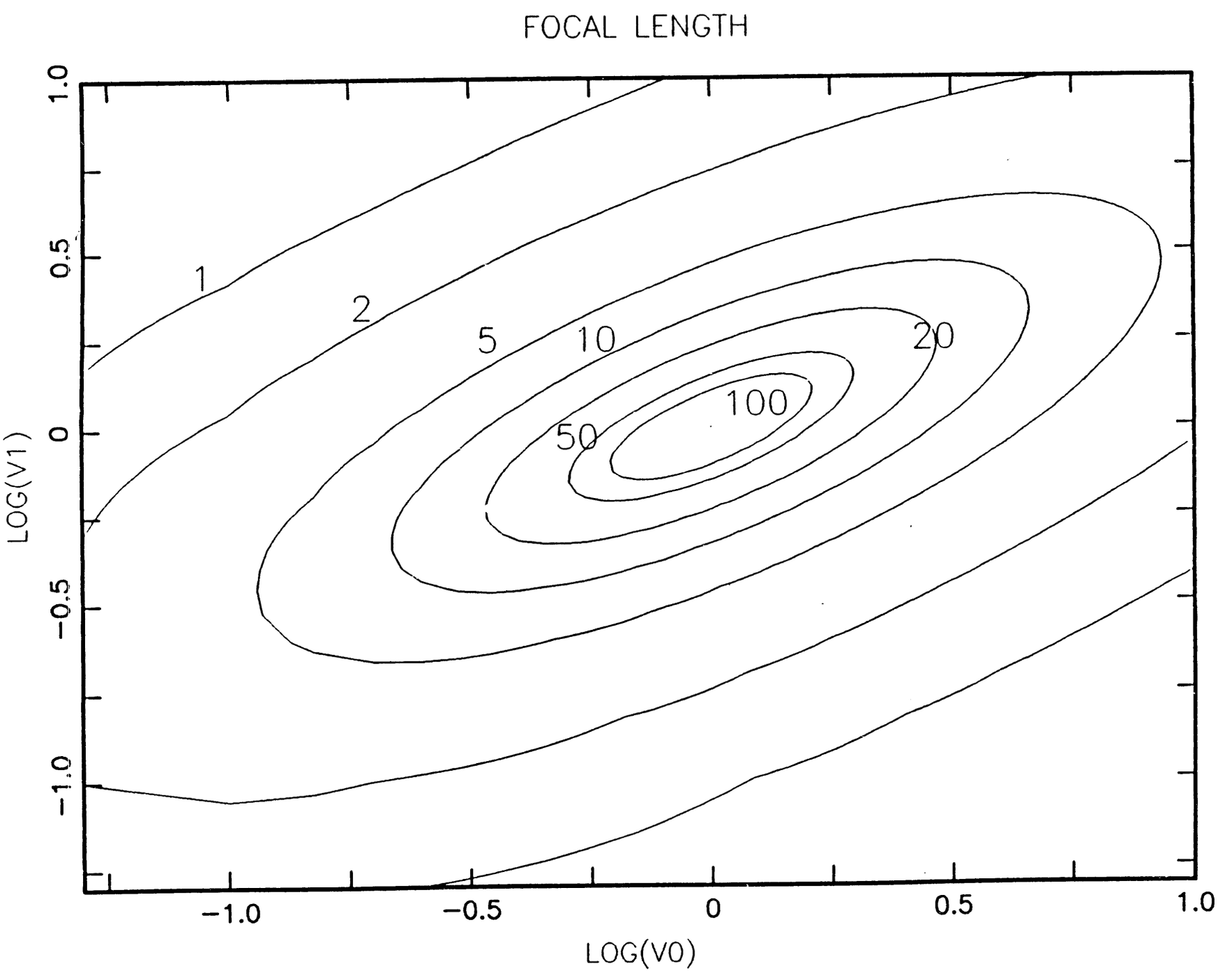
FOCAL LENGTH
1.0
0.5
0
−0.5
−1.0
LOG(V1)
1
2
5
10
20
50
100
−1.0
−0.5
0
0.5
1.0
LOG(V0)

II. BIOLOGICAL STUDIES

The Principal Subunit of Earthworm Hemoglobin

The extracellular Hbs of the annelids are giant molecules with an acidic isoelectric point, a sedimentation coefficent of 60 S and a low iron content of 0.23 ± 0.03 *wt.*% (1-6). In addition, these Hbs have a symmetrical, hexagonal bilayer appearance in electron micrographs (7-9). The extracellular Hb of *Lumbricus terrestris* is the most well-studied Hb of the annelid group with an estimated M_w of about 3.600 kDa (10). SDS-PAGE shows that it consists of four subunits: monomer, *M* (17 kDa), linkers, *D1* and *D2* (*ca.* 30 kDa) and trimer, *T* (50 kDa). The subunits *M* and *T* contain heme and consist of globin chains I and disulfide-bonded chains II, III and IV, respectively. The complete amino acid sequences of these chains are known (11-13). The *D1* and *D2* subunits contain very little heme, and consist of two chains, *VA* and *VB*, and of chain VI, respectively (14). Studies of the dissociation of *Lumbricus* Hb at alkaline pH (15), at acid pH (14) and at neutral pH in the presence of various dissociating agents (16) have shown that, although dissociation products having an estimated M_m of *ca.* 200 kDa were obtained under equilibrium conditions, they never had the same subunit composition as does the native Hb. To explain the results, a heteromultimeric model was proposed (16,17) in which a "bracelet", or scaffolding, of 30 kDa "structural" subunits having little or no heme is decorated by twelve complexes (each of *ca.* 200 kDa) of heme-containing subunits, each complex consisting of three copies of the monomer (17 kDa) and three copies of the disulfide-bonded trimer (51 kDa). In this work, we report the isolation and characterization of the *ca.* 200 kDa complex by mild dissociation of *Lumbricus* Hb at neutral pH.

Materials and Methods

Live *Lumbricus* were obtained from Forest Bait Farm (London, Ontario, Canada). The Hb was prepared as described by Shlom and Vinogradov (18), and was kept in CO-saturated 0.1 M Tris HCl buffer pH 7.2, 1 mm EDTA. Repeated dissociation of *Lumbricus* Hb was carried out according to the method of Vinogradov *et al.* (16) in the presence of urea at neutral pH using columns of Sephadex G-200 and G-100 for gel filtration. Analytical gel filtration was performed on 1 x 30 cm columns of Superose S-6 (Pharmacia, Piscatawauy, NJ, USA) using a low pressure FPLC system (Pharmacia). SDS-PAGE was carried out in 0.1% SDS using 1 mm x 10 cm x 20 cm slab gels and the buffer system of Laemmli (19). The gels were scanned on a Zeineh densitometer and the areas under the peaks determined by weighing. Unstained, freeze-dried specimens were used for mass measurements by the Brookhaven STEM using the method of Wall and Hainfeld (20). The negatively stained samples were examined as described by Kapp *et al.* (21) in the dark field mode with a high-resolution field emission STEM at the University of Chicago.

Results and Discussion

The first generation peak I*b* obtained by gel filtration on a Sephadex G-200 column after the dissociation of *Lumbricus* Hb in 4M urea was subjected to dialysis against 4 M urea and gel filtration on a Sephadex G-100 column to obtain the second generation peak I*b'*. The latter was treated similarly to produce the third generation peak I*b''*.

Figure 1 depicts the SDS-PAGE pattern of unreduced *Lumbricus* Hb (lanes 1 and 5), the first generation peak I*b* (lane 2), the second generation peak I*b'* (lane 3) and the third generation peak I*b''* (lane 4), each obtained by repeated dissociation in 4 M urea. The results of the densitometry of the unreduced SDS-PAGE patterns are shown in Table 1. Peak I*b* is the largest fragment of *Lumbricus* Hb obtained by its dissociation in 4 M urea at neutral pH. Yet, its content of subunits *D*1 and *D*2 is only about 25% of the native molecule, demonstrating clearly that I*b* is not a protomer and that the Hb is heteromultimeric, which is in agreement with previous results (16). Further dissociation results in a decrease in the relative proportions of subunits *D*1 and *D*2 from 6.0 ± 1.9 in peak I*b* to 5.3 ± 2.0 in peak I*b'*, and 2.3 ± 1.4 in peak I*b''*. Analytical gel filtration on a Superose S6 column indicates an increase in the elution volumes by 0.05 ml from peak I*b* to peak I*b'*, and by 0.1 ml from peak I*b'* to peak I*b''*, with the relative changes in mass proportional to the changes in the percent content of *D*1 and *D*2 (Table 1).

The elution profile obtained by analytical gel filtration of peak I*b'* at neutral pH on Superose S6 columns is shown in Figure 2A. Only one peak was observed and its mass, estimated from plots of log *M* versus elution volume, was 191 kDa (Table 2). This particle could be dissociated completely at neutral pH in 4 M guanidine HCl into the constituent subunits *M* and *T* (Figure 2B). Figures 2C and D show the FPLC elution profiles of the subunits *M* and *T*, isolated concurrently with peak I*b'*. As shown in Figure 2E, mixing the subunits *M* and *T* resulted in the partial reassociation into particles the elution volume of which was the same as that of peak I*b'* in Figure 2A, and the mass of which was determined to be *ca.* 182 kDa.

The mean mass of the unstained, freeze-dried specimen of peak I*b'* obtained with the Brookhaven STEM (Figure 3A) was 197 ± 19 kDa (Table 2). Figure 3B shows a micrograph of unstained, freeze-dried *Lumbricus* Hb. It is apparent that some of the hexagonal bilayer molecules have dissociated into particles of a size which corresponds to that of the I*b'* particles. The mean mass of the particles in Figure 3B is 188 kDa (Table 2). Figures 3C and D show micrographs of negatively stained peak I*b'* and peak *R* (Figure 2E) obtained with the STEM. Due to the presence of traces of subunits D1 and D2, it appears that some reassociation into complete hexagonal bilayer molecules has occurred: peak *R* (Figure 2E) has an SDS-PAGE composition similar to that of the native *Lumbricus* Hb (Table 1).

The experimental results clearly show that a particle of *ca.* 200 kDa, consisting of subunits *T* and *M*, exists within the structure of *Lumbricus* Hb. The experimental estimates of its mass are in very good agreement with the theoretical value of 209 kDa for a trimer of the *T* and *M* complex, calculated using the masses from the known amino-acid sequences of the four chains I. II, III and IV (Table 2). Hence, a 209 kDa dodecameric complex, 3(I + II + III + IV), represents the largest subunit of *Lumbricus* Hb. This subunit has been shown recently to have the same oxygen affinity as does the native Hb but only two thirds of its cooperativity (22). The demonstration of the existence of a stable and functional dodecameric complex of globin chains within the quaternary structure of *Lumbricus* Hb, represents an important step in the understanding of the architecture of annelid Hbs and Chls and provides very

convincing support for a model wherein twelve dodecameric subunits arranged in two hexagonal layers are held together by heme-deficient, *ca.* kDa chains (16,17).

References

1. Mangum, C. (1976) In *Adaptations to Environment: Physiology of Marine Animals*, ed. P.C. Newell, 191-278. London: Butterworth's.

2. Weber, R.E. (1978) In *Physiology of Annelids*, ed. P.J. Mill, 393-445. London: Academic Press.

3. Chung, M.C.C. and Ellerton, H.D. (1979) *Prog. Biophys. Mol. Biol.* **35**: 51-102.

4. Vinogradov, S.N., Shlom, J.M., Kapp, O.H. and Frossard, P. (1980) *Comp. Biochem. Physiol.* **67B**: 1-16.

5. Vinogradov, S.N. (1985) *Comp. Biochem. Physiol.* **82B**: 1-15.

6. Vinogradov, S.N. (1985) In *Respiratory Pigments in Animals*, eds. J. Lamy, J.P. Truchot and R. Gilles, 9-20. Berlin: Springer-Verlag.

7. Levin, O. (1963) *J. Mol. Biol.* **6**: 93-99.

8. Kapp, O.H., Vinogradov, S.N., Ohtsuki, M. and Crewe, A.V. (1982) *Biochim. Biophys. Acta* **704**: 546-548.

9. Vinogradov, S.N., Kapp, O.H. and Ohtsuki, M. (1982) In *Electron Microscopy of Proteins*, ed. J. Harris, Vol. 3, 135-163.

10. Vinogradov, S.N. and Kolodzej, P. (1988) *Comp. Biochem. Physiol.* **91B**: 577-579.

11. Garlick, R.L. and Riggs, A. (1982) *J. Biol. Chem.* **257**: 9005-9015.

12. Shishikura, F., Snow, J.W., Gotoh, T., Vinogradov, S.N. and Walz, D.A. (1987) *J. Biol. Chem.* **262**: 3123-3131.

13. Fushitani, K., Matsuura, M.S.A. and Riggs, A.F. (1988) *J. Biol. Chem.* **263**: 6502-6517.

14. Mainwaring, M.G., Lugo, S.D., Fingal, R.A., Kapp, O.H. and Vinogradov, S.N. (1986) *J. Biol. Chem.* **261**: 10899-10908.

15. Kapp, O.H., Polidori, G., Mainwaring, M.G., Crewe, A.V. and Vinogradov, S.N. (1984) *J. Biol. Chem.* **259**: 628-639.

16. Vinogradov, S.N., Lugo, S.L., Mainwaring, M.G., Kapp, O.H. and Crewe, A.V. (1986) *Proc. Natl. Acad. Sci. U.S.A.* **83**: 8034-8038.

17. Vinogradov, S.N. (1986) In *Invertebrate Oxygen Carriers*, ed. B. Linzen, 25-36. Berlin: Springer-Verlag.

18. Shlom, J. and Vinogradov, S.N. (1973) *J. Biol. Chem.* **248**: 7904-7912.

19. Laemmli, U. (1970) *Nature* **227**: 680-685.

20. Wall, J.S. and Hainfeld, J.F. (1986) *Annu. Rev. Biophys.* **15**: 355-376.

21. Kapp, O.H., Qabar, AnN., Bonner, M.C., Stern, M.S., Walz, D.A., Schmuck, M., Pilz, I., Wall, J.S. and Vinogradov, S.N. (1990) *J. Mol. Biol.* **213**: 141-158.

22. Vinogradov, S.N., Sharma, P.K., Qabar, A.N., Wall, J.S., Westrick, J.A., Simons, J.H. and Gill, S.J. (1991) *J. Biol. Chem.* In press.

Figure 1.

Unreduced SDS-PAGE pattern of *Lumbricus* Hb (lanes 1 and 5), first generation peak I*b* (lane 2), second generation peak I*b*′ (lane 3) and third generation peak I*b*″ (lane 4) obtained by repeated dissociation in 4 M urea and gel filtration on a 6.5 x 50 cm Sephadex G-200 column (first generation peak) and a 5.5 x 105 cm Sephadex G-100 column (second and third generation peaks) at neutral pH.

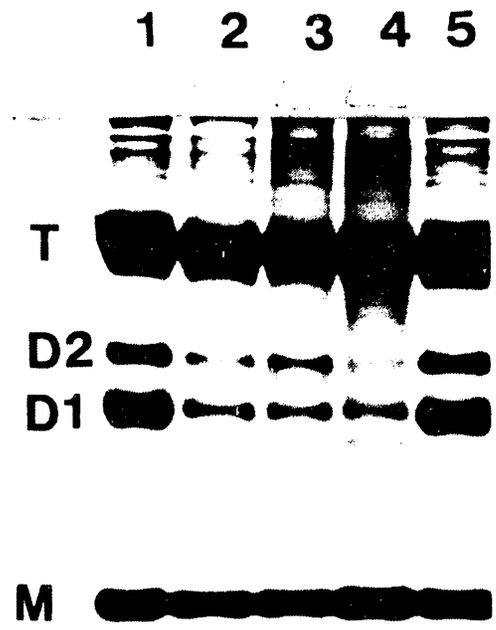
1 2 3 4 5
T
D2
D1
M

Figure 2.

FPLC elution profiles on a 1 x 30 cm column of Superose 6: (*A*) peak *Ib'*; (*b*) peak *Ib'* in 4 M Gdn.HCl; (*C*) peak *II'*; (*D*) peak *III'* and (*E*) an equimolar mixture of peaks II and III.

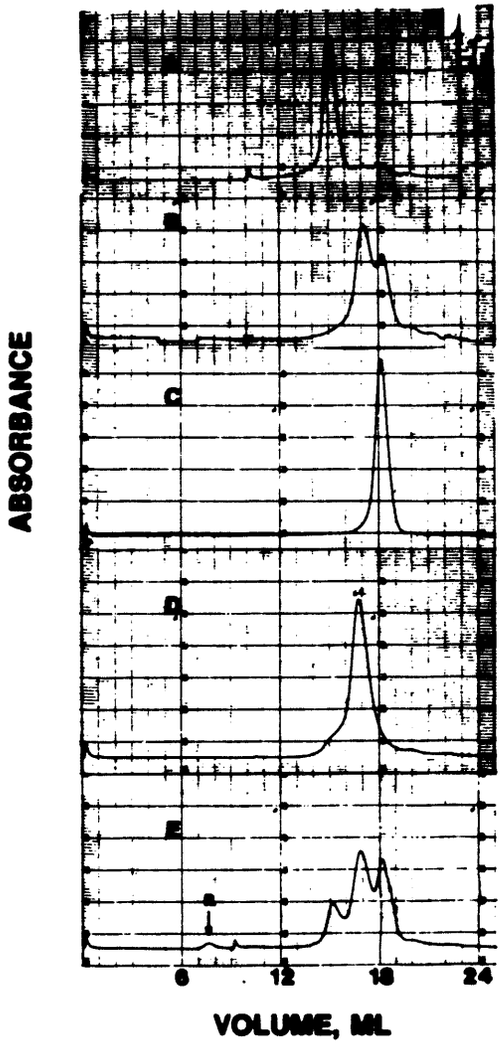
ABSORBANCE
6
12
18
24
VOLUME, ML

Figure 3.

Brookhaven STEM micrographs of unstained, freeze-dried specimens: (*A*) peak I*b*′ and (*B*) *Lumbricus* Hb. The dimensions of the field of view are 1525 x 1525 Å. University of Chicago STEM micrographs of negatively stained specimens: (*C*) peak I*b*′ and (*D*) peak *R* in Figure 2 (magnification x 149,000).

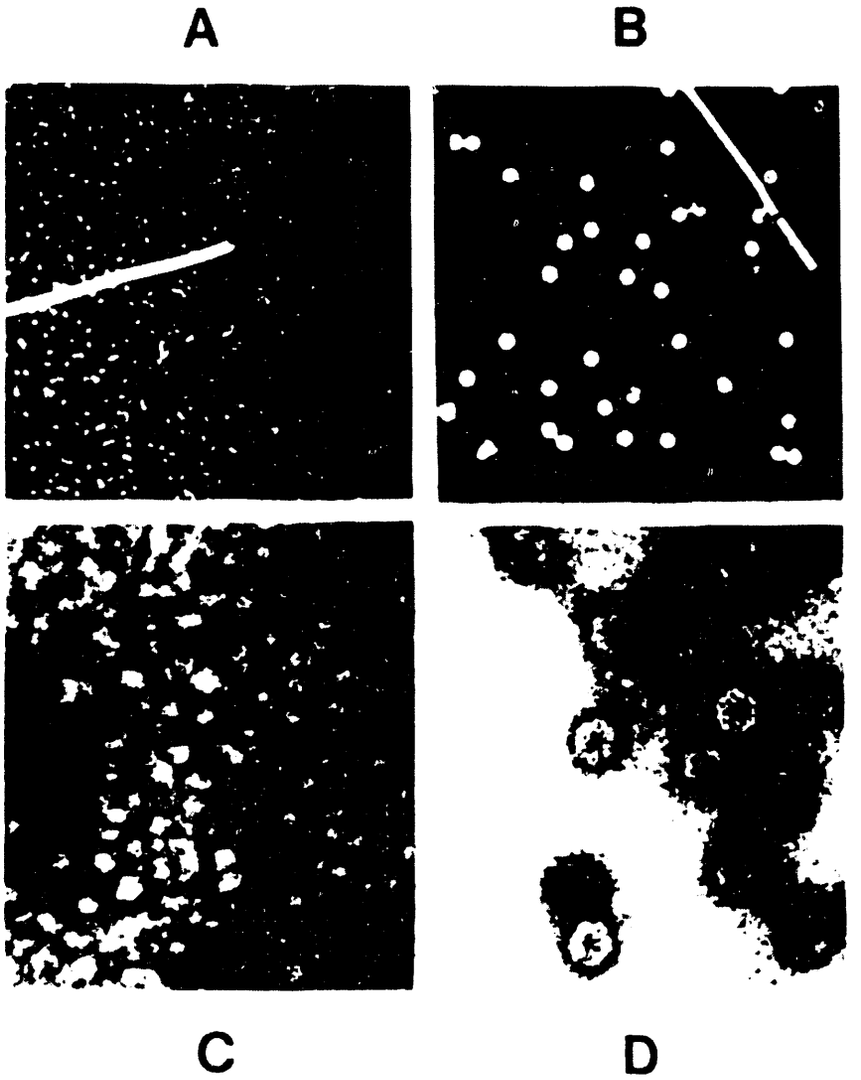
A
B
C
D

Table 1.

Relative proportions (% of total area) of subunits *T*, *D*1, *D*2 and *M* in the three generation peaks I*b*, I*b*′, and I*b*″ obtained by repeated dissociation in 4 M urea and gel filtration at neutral pH, determined by densitometry of unreduced SDS-PAGE patterns.

Subunit	Control (n = 10)	Peak I*b* (n = 6)	Peak I*b*′ (n = 6)	Peak I*b*″ (n = 6)	Peak *R*
M	20 ± 1.6	24 ± 2.5	24 ± 3.2	26 ± 1.9	20
*D*1, *D*2	24 ± 3.3	6.0 ± 1.9	5.3 ± 2.0	2.3 ± 1.4	22
T	56 ± 3.7	70 ± 3.3	70 ± 4.2	71 ± 2.9	58

Table 2.

Results of mass determinations by gel filtration and of STEM mass measurements.

Material	Gel Filtration (kDa)	STEM (kDa)	Calculated [a] (kDa)
Peak *Ib'*	191	197 ± 19 (*N* = 91)	209
Peak II (subunit *T*)	50	-	52.9
Peak III (subunit *M*)	17.?	-	16.75
Peak II + III	182	201 ± 39 (*N* = 65)	-
Lumbricus Hb[b]	-	188 ± 21 (*N* = 18)	-

a From amino acid sequences (12, 13).
b Calculated from the particles present in Figure 3*B* due to the partial dissociation of *Lumbricus* Hb during specimen preparation.

Studies on the Dissociation of Eudistylia Vancouverii Chlorocruorin

Summary

The molecular dimensions of the extracellular, hexagonal bilayer chlorocruorin of the marine polychaete *Eudistylia vancouverii* determined by scanning transmission electron microscopy (STEM) of negatively stained specimens, were a diameter of 27.5 nm and a height of 18.5 nm. STEM mass measurements of unstained, freeze-dried specimens provided a $M_m = 3,480 \pm 225$ kDa. The chlorocruorin had no carbohydrate and its iron content was 0.251 ± 0.021wt.%, corresponding to a minimum M_m of 22.4 kDa. Mass spectra and NMR spectra of the prosthetic group confirmed it to be protoheme IX with a formyl group at position 3. SDS/polyacrylamide gel electrophoresis, reversed phase chromatography and N-terminal sequencing suggested that the chlorocruorin consists of at least three chains of ca. 30 kDa and five chains of ca. 16 kDa; the two types of subunits occur in the ratio 0.26:0.74 (±0.08). Complete dissociation of the chlorocruorin at neutral pH in the presence of urea or Gu.HCl, followed by gel filtration, produced elution profiles consisting of three peaks B, C and D. Fractions B and C consisted of the ca. 16 kDa chains and fraction D consisted of the ca. 30 kDa subunits. Mass measurements of particles in STEM images of unstained, freeze-dried fractions B and C provided M_m of 208 ± 23 kDa and 65 ± 12 kDa, respectively, in agreement with 191 ± 13 kDa and 67 ± 5 kDa obtained by gel filtration. Particles with M_m = 221 ± 21 kDa were also observed in STEM images of unstained, freeze-dried chlorocruorin. These results imply that the chlorocruorin structure, in addition to the ca. 30 kDa linker subunits whihc have 0.26-0.47 heme/chain, comprises ca. 65 kDa tetramers and ca. 200 kDa dodecamers (trimers of tetramers) of globin chains. The stoichiometry of the tetramer and linker subunits calculated from molar amino acid composition is 34 ± 4 and 43 ± 9. The complete dissociation of the chlorocruorin was accompanied by a 50-75% loss of the 55 ± 14 Ca^{2+}/mole protein, and was decrease to ca. 35% by the presence of 10 to 25 mM Ca^{2+}. Reassociation of dissociated chlorocruorin was maximal in the presence of 2.5-5mM Ca^{2+}. The dodecamer and/or tetramer subunits in the absence or presence of Ca^{2+}, exhibited very limited (<10%) reassociation into hexagonal bilayer structures only in the presence of the linker subunit. Although the circular dichroism (200-250nm) of the chlorocruorin and the dodecamer subunit were similar with alpha-helical contents of ca. 50%, the α-helical content of the tetramer and linker subunits were lower. Our results are compatible with a view of the quaternary structure of *Eudistylia* chlorocruorin as a hierarchy of globin complexes, wherein 66 to 75% of the whole molecule is comprised of twelve ca. 200 kDa dodecamers, each consisting of a trimer of tetramers of globin chains having an incomplete "myoglobin fold". The dodecamers are linked into a hexagonal bilayer structure by 30-40 Ca^{2+} and 30-40 heme-deficient, chimeric globin chains.

Introduction

The 60S hemoglobins of annelids represent one of several types of quaternary structure observed among invertebrate, extracellular, oxygen-binding heme proteins (Vinogradov, 1985a). They have two distinctive properties: a low iron content of ca. 0.23 wt.% (two thirds of the normal value of 0.33%), and a hexagonal bilayer appearance in electron micrographs (Antonini & Chiancone, 1977; Chung & Ellerton, 1979; Vinogradov et al., 1980a; Terwilliger 1980). These molecules also exhibit variable cooperativities of oxygen binding and moderate affinities (Mangum, 1976; Weber, 1978). The few chlorocruorins which have been studied, namely those of *Spriographis spallanzanii*, *Eudistylia vancouverii* and *Myxicola infundibulum*, appear to have the same physical and chemical properties as the hemoglobins (Antonini et al., 1962a; Guerritore et al., 1965; Terwilliger et al., 1975, 1976; Vinogradov et al., 1985).

Our investigations of the most studied annelid hemoglobin, that of *Lumbricus terrestris* (Vinogradov et al., 1977; Kapp et al., 1984; Mainwaring et al., 1986) have shown that this giant ca. 3,600 kDa molecule is heteromultimeric, consisting of two types of subunits: four heme-containing chains of ca. 17 kDa whose amino acid sequences have been determined (Shishikura et al., 1987; Fushitani et al., 1988) and at least three chains of ca. 30 kDa which are deficient in heme and whose primary structures remain undetermined (Walz et al., 1987; Fushitani & Riggs, 1988). In contrast, no amino acid sequence information is available for any of the chlorocruorins. Based on our studies, we have proposed a model of *Lumbricus* hemoglobin quaternary structure (Vinogradov, 1986b; Vinogradov et al., 1986), wherein twelve ca. 200 kDa complexes are linked by heme-deficient ca. 30kDa subunits. Substantial support for this model has been provided recently by the isolation, via mild dissociation of the hemoglobin at neutral pH, of a 200 kDa dodecameric globin complex which has the same oxygen affinity but only two thirds the cooperativity of oxygen binding of the native molecule (Vinogradov et al., 1991a). We have sought to extend our studies to a chlorocruorin, because SDS electrophoretic patterns of unreduced, i.e. native, molecules of *Potamilla leptochaeta* (Vinogradov & Orii, 1980) and *Myxicola infundibulum* (Vinogradov et al., 1985) chlorocruorins were different from those of *Lumbricus* hemoglobin and the leech, oligochaete and polychaete molecules (Vinogradov, 1985a, 1985b). We report below the results of determinations of several physical and chemical properties of the chlorocruorin of the marine polychaete *Eudistylia vancouverii*, which suggest that its quaternary structure consists of a hierarchy of globin complexes similar to that of *Lumbricus* hemoglobin.

Results

Molecular Size and Mass

The STEM images of negatively stained *Eudistylia* chlorocruorin obtained in the presence and absence of Ca are shown in Figure 1, A and B, respectively. These images demonstrate that Ca is required for maintenance of the quaternary structure of the hemoglobin. The native hemoglobin is very similar to that of the marine polychaete *Myxicola* chlorocruorin (Vinogradov et al., 1985). The dimensions of the two chlorocruorins are 27.5 x 18.5 nm (diameter x height) and 29.0 x 19.0 nm, respectively, in fair agreement with the dimensions (23.0 x 18.6 nm) of *Spirographis* chlorocruorin (Ghiretti-Magaldi et al., 1983) and somewhat smaller than those of *Lumbricus* hemoglobin (30 x 20 nm) (Kapp et al., 1984).

Figure 2A shows a typical field of view of unstained, freeze-dried *Eudistylia* chlorocruorin and a TMV particle. Mass measurements at the Brookhaven STEM over a period of three years provided the following mean M_m for several different preparations: 3437 ± 252 (n = 266), 3513 ± 217 (n = 44), 3462 ± 232 (n = 53), 3488 ± 152 (n = 105) and 3471 ± 272 kDa (n = 94). The histogram for the first set is given in Figure 3 (left). It can be seen that the distribution of particle mass is asymmetrical with relatively more particles with M_m below the mean; this is not unexpected, since some loss of material from a multisubunit protein can occur during specimen preparation. The shaded portion of the plot represents the distribution of 47 particles (out of the 266) which were selected on the basis of the following two criteria: (1) clean background up to the edge of the particle together with the presence of a central depression and (2), at least 40% of the image power had 6-fold symmetry. From the histogram and the mean, M_m = 3436 ± 173 kDa, it can be seen that this more exacting selection did not provide a significantly different distribution or mass. Minimum crosslinking of the chlorocruorin with glutaraldehyde following the method of CaJacob et al. (1985) (Figure 2B), gave M_m = 3486 ± 262 kDa (n = 90), not significantly different from the foregoing values. The mean M_m of all the results is 3476 ± 26 kDa and the mean S.D. is 225 ± 38 kDa. The excellent agreement between the different determinations makes it very likely that the true M_m of *Eudistylia* chlorocruorin is closer to 3480 kDa than ±225 kDa.

(b) Extinction Coefficients, Iron and Carbohydrate Contents

The extinction coefficients ($\pm SD$) of *Eudistylia* chlorocruorin at 280 nm and 605 nm at neutral pH, were determined to be (2.23 ± 0.17) and 0.472 ± 0.035 $ml.mg^{-1}cm^{-1}$, respectively, based on dry weight determination. The concurrently determined extinction coefficients at 280 nm of *Lumbricus* hemoglobin and sperm whale myoglobin were 2.04 ± 0.14 and 1.74 ± 0.07 $ml.mg^{-1}cm^{-1}$, respectively, in good agreement with the published values for *Lumbricus* hemoglobin, 2.12 $ml.mg^{-1}cm^{-1}$ (Kapp et al., 1984) and for sperm whale myoglobin, 1.70 $ml.mg^{-1}cm^{-1}$ (calculated from 31.2 $mM^{-1}cm^{-1}$: Hanania et al., 1966).

The iron content of *Eudistylia* chlorocruorin 0.251 ± 0.021 wt.%, corresponds to a minimum molecular mass of 22.4 kDa and is higher than the 0.212 wt.% determined by Terwilliger et al. (1975). The two values straddle the range of the published iron contents of other annelid hemoglobins and chlorocruorins (Vinogradov et al., 1991b).

Analysis of the carbohydrate content of *Eudistylia* chlorocruorin showed that it had no mannose or N-acetyl-glucosamine. Since only glucose was detected at very low levels, we conclude that the chlorocruorin does not contain carbohydrate, similar to *Macrobdella* hemoglobin and in contrast to *Lumbricus* hemoglobin (Shishikura et al., 1986).

(c) Determination of the Chloroheme Structure

The chloroheme extract gave prominent visible bands at 412, 380, 512, 548, 600 and 636 nm and the prophyrin ester gave a rhodo-type spectrum with bands at 420, 518, 556, 584, 648 and 688 nm. These are similar to the spectra reported previously for the 3-formyl and the isomeric 8-formyl heme or porphyrin (Inhoffen et al., 1966, 1969; Jackson et al., 1967). Fast atom bombardment mass spectrometry in a thioglycerol matrix consistently produced the $(M + M)^+$ parent ion at 593, in accord with the expected empirical formula of $(C_{35}H_{36}N_4O_5 + H)$. The proton chemical shifts obtained at 500 MHz in deuterated

dichloromethane were consistent with the results reported for the two isomers. Especially critical features were the appearance of the unique aldehyde proton at 11.53 ppm and a single vinyl substituent. The correct isomeric structure was estabished by observation of the distinctive pattern of nuclear Overhauser enhancements among the porphyrin substituents as described previously (Timkovich et al., 1985; Padavanija & Timkovich, 1986).

(d) SDS-polyacrylamide Gel Electrophoresis

The SDS/polyacrylamide gel electrophoretic patterns of the chlorocruorin in the absence and presence of 2-mercaptoethanol are compared with the corresponding patterns of *Lumbricus* hemoglobin in Figure 4. The unreduced chlorocruorin appears to consist of three subunits, of which 1 and 2 are ca. 30 kDa and subunit 3 is ca. 65 kDa. The presence of subunits only in the two mass ranges is in agreement with the unreduced pattern of *Myxicola Hydroides* chlorocruorin (Waxman, 1975; Vinogradov et al., 1985). The patterns of the reduced chlorocruorins of *Eudistylia* and *Myxicola* are very similar to the patterns of the reduced hemoglobins of the oligochaete *Tubifex* and the polychaete *Arenicola* (Waxman, 1971; Terwilliger et al., 1975; Vinogradov et al., 1979, 1980b).

The correspondence between the unreduced and reduced *Eudistylia* chlorocruorin subunits is indicated by arrows in Figure 4. Subunit 1 corresponds to subunit III and both subunits 2 and 3 correspond to subunits I and II. Although the electrophoretic patterns of reduced chlorocruorin were always similar, those of the native or unreduced chlorocruorin were variable in that the abundance of subunit 2 ranged from very little or none to substantial, as shown in Figure 4. Furthermore, storage of chlorocruorin tended to increase the relative amount of subunit 2. These results suggest that the native molecule is composed of nonreducible subunits of ca. 30 kDa nad subunits of 65 kDa, which consist of noncovalently aggregated disulfide-bonded dimers of globin chains and of disulfide-bonded tetramers of globin chains.

(e) Number of Polypepetide Chains and N-terminal Sequences

Figure 5 shows a typical elution profile obtained by reversed phase chromatography of redued, carboxymethylated *Eudistylia* chlorocruorin. SDS/polyacryamide gel electrophoresis of the seven peaks demonstrated that the first group of three peaks corresponded to the ca. 30 kDa subunits and that the second group consisting of at least four peaks, corresponded to subunits I and II. Peak 5 was rechromatographed using a shallower gradient (data not shown) and two peaks were obtained, 5a and 5b: although peak 5a provided a sequence, peak 5b did not. The available N-terminal sequences are provided in Table 1 and compared with the corresponding sequence of the monomer chain (subunit I) of *Lumbricus* hemoglobin (Shishikura et al., 1987). Two of the tetrameric constituent chains, have sequences, KVKLQ in chain 7 and KVK in chain 5a, which are identical to all or part of the KVKLQ sequence of the monomer subunit. The chlorocruorin probably consists of at least eight different chains, five globin chains of ca. 16 kDa and three chimeric globin chains of ca. 30 kDa.

(f) Subunit Stoichiometry from SDS Gel Patterns

The subunit stoichiometries were calculated from densitometric scans of SDS/polyacrylamide gel patterns of unreduced and reduced, native and carboxymethylated chlorocruorin and from the spectrophotometric determination of dye eluted from SDS gel slices containing the individual subunits. The number of copies of the subunits were calculated from the equation:

$$N_j = \frac{(3,500)A_j}{(A_T \times M_j)}$$

where A_j is either the area under the peak of subunit j or the absorbance at 595 nm of the dye eluted from the gel slice containing the *jth* subunit, A_T is either the total area in a densitometric scan or the abosorbance at 595 nm of the dye eluted from all the subunits and M_j is the M_m of the *jth* subunit. The absorbance readings were corrected for the absorbance of blanks in proportion to the mass of the gel slices and checked for linearity versus total protein load. The results, calculated assuming that the subunits have the same binding affinity for the dye, are given in Table 2 as fraction percent contributed by each subunit ($\frac{A_j}{A_T}$) and as N_j calculated assuming M_1 = 26.5 kDa and M_2 = 68 kDa (Table 5). It is evident that the fraction percent of the nonreducible 30kDa subunit is overestimated in the electrophoretic patterns of unreduced material because of overlap between subunits 1 and 2 (Figure 4). The contribution of subunit 2, disulfide-bonded dimers which aggregate noncovalently to subunit 3, the 65 kDa tetramer, can be estimated to be 21% from densitometry and 27% from dye quantitation (Table 2). The proportions of the 65 kDa (tetramer) and ca. 30 kDa (linker) subunits derived from experiments with the reduced material (Table 2) is 0.74:0.26, in good agreement with the ratio of 0.71:0.29 observed by Terwilliger et al. (1975).

(g) Dissociation of *Eudistylia* Chlorocruorin

Figure 6A shows the elution pattern of the chlorocruorin subjected to gel filtration at neutral pH subsequent to dissociation in 4M urea. Three or four peaks were observed, depending on whether dissociation was complete or not. The inset in Figure 6A shows the SDS/polyacrylamide gel electrophoretic patterns of the chlorocruorin and the three peaks representing the dissociated material, obtained in the absence and presence of 2-mercaptoethanol. Unreduced peak B consists of subunits 2 and 3 (lane 2), and reduced peak B consists of subunits I and II (lane 5). Unreduced peak C consists of subunit 2 (lane 3) and reduced peak C consists of subunits I and II (lane 6). Peak D appears to consist of the ca. 30 kDa subunit III (lanes 4 and 7); in the pattern shown some contamination with peak C is evident.

The appearance only of disulfide-bonded dimers (subunit 2) in the SDS electrophoretic pattern of unreduced peak C fraction (Figure 6A, lane 3) as opposed to both disulfide-bonded dimers and disulfide-bonded tetramers (subunit 3) in the peak B fraction (Figure 6A, lane 2), is in agreement with the electrophoretic results (Results, section (d)). The disulfide-bonded dimers represent ca. 43% of the 65 kDa tetramer based on densitometry of the unreduced peak B pattern (lane 2, inset in Figure 6A).

Dissociation of the chlorocruorin at alkaline pH or at neutral pH in the presence of Gu.HCl, followed by gel filtration at neutral pH, produces elution patterns very similar to that in Figure 6A: the elution volumes of the three peaks and their SDS electrophoretic patterns remain remarkably constant.

The isolation of the products of dissociation of *Eudistylia* chlorocruorin subjected to dialysis against 4M urea was achieved on a 5x100 cm column of Sephadex G-100. The fractions corresponding to peaks B, C and D were collected and subjected to SDS electrophoresis in the presence of 2-mercaptoethanol. They were pooled on the basis of their subunit content and subjected to analytical gel filtration at neutral pH on columns of Superose S-12. The results are shown in Figure 6, panels B, C and D. The M_m corresponding to the elution volumes of peaks B, C and D are collected in Table 3: 196 ± 10 kDa and 39 ± 8 kDa, respectively.

Although the elution volumes of peaks C and D were generally constant, the elution volume of peak B was observed to range from 11.9 to 12.4 ml on Superose S-12 and from 15.7 to 16.1 ml on Superose S-6 columns, depending on the duration of exposure of the chlorocruorin to the dissociating agent and the concentration of the latter. On both columns the greater elution volumes correspond to an apparent M_m of 140-150 kDa.

Analytical gel filtration at neutral pH of peak B exposed to 6M Gu.HCl is shown in Figure 7A. It is readily apparent that the ca. 200 kDa complex is partially dissociated into 65 kDa subunits (peak C) and ca. 30 kDa subunits (peak D). Since peak B consists only of globin chains (subunits I and II), peak D in this case consists of the disulfide-bonded dimers of globin chains in agreement with the SDS gel electrophoresis of peak C (lane 3) obtained by 4M urea dissociation (inset in Figure 6A).

STEM Mass Determination of Chlorocruorin Subunits

Numerous small particles of ca. 10 nm in diameter can be observed in fields of view of negatively stained (Figure 1B) as well as unstained, freeze-dried chlorocruorin (Figure 2A). These particles are not observed in the presence of Ca (Figure 1A) or when the chlorocruorin is cross-linked (Figure 2B). A typical histogram of the M_m values of the ca. 10 nm particles observed in several fields of view of unstained, freeze-dried chlorocruorin is shown in Figure 3 (right): mean M_m = 218 ± 28 kDa (n = 159) (Table 3).

STEM examination of unstained, freeze-dried specimens of peak B (Figure 2C) revealed that it consists almost exclusively of ca. 10 nm particles in agreement with observations on negatively stained specimens (Figure 1, B and C). A typical histogram is shown in Figure 8 (left panel), mean M_m = 208 ± 23 kDa (n = 662). Particles of similar size have been observed in a preliminary study of *Eudistylia* chlorocruorin dissociation (Qabar et al., 1991).

STEM images of unstained, freeze-dried peak C (Figure 2D) appear to contain a more heterogeneous distribution of particles, the predominant majority being appreciably smaller than 10 nm. A histogram of 899 such particles is provided in Figure 8 (right): the overwhelming majority of particles have M_m of about 65 kDa. The calculated mean values are 65 ± 17 kDa (n = 635) for the 30-90 kDa range and 64 ± 15 kDa (n = 132), and a smaller number occur in the 100-165 kDA range: mean M_m = 118 ± 20 kDa (n = 90). These results suggest that the 65 kDa particle is stable and can aggregate to ca. 200 kDa trimers of tetramers.

UV-VIS Absorption Spectra and UV Circular Dichroism of Chlorocruorin and its Subunits

The uv/vis absorption spectra of *Eudistylia* chlorocruorin are in agreement with the spectra obtrained for the chlorocruorins of *Potamilla* (Orii & Washio, 1977) and *Spirographis* (Antonini et al., 1962a). The ratios of the Soret band absorbance to the 280 nm absorbance of *Eudistylia* chlorocruorin and of its three subunits obtained by dissociation in 4M urea, are provided in Table 4 for the carbonmonoxy and cyanmet forms. Our results for the whole molecule should be compared with ratios of 1.51 for the oxychlorocruorin of *Sphirographis* (Antonini et al., 1962a) and 1.12 for the ferrichlorocruorin of *Potamilla* (Orii & Washio, 1977). The ratio for peak D, the ca. 30 kDa linker subunit, are much smaller than the ratios for the chlorocruorin and the other two subunits, suggesting that it has less than one heme group per 30 kDa of protein. Since the absorption at 280 nm is due primarily to the number of Trp and Tyr residues, we have sought to estimate the number of heme groups per ca. 30 kDa chain by the following procedure: (1) We assumed that the *Eudistylia* chlorocruorin globin and linker subunits have the same Trp and Tyr contents as the averages for the corresponding subunits of *Tylorrhynchus*, *Lamellibrachia* and *Lumbricus* hemoglobins, calculated from their known amino acid sequences (Table 5). (2) Next, we assumed that the A_{Soret}/A_{280} is proportional to the number of heme groups per subunit, and used the molar extinction coefficients for Trp and Tyr model compounds (Edelhoch, 1967), to estimate the number of heme groups associated with the linker subunits to be 0.26-0.47 heme/ca. 30 kDa chain.

The circular dichroism over the range 200-250 nm, of *Eudistylia* chlorocruorin and its three subunits, obtained by dissociation in 4M urea, are shown in Figure 9. The mean residue ellipticities at 222 nm and the percent alpha-helix calculated according to Chen et al. (1972) are provided in Table 4. The alpha-helical contents of hte chlorocruorin and the dodecamer are higher than the values reported for *Lumbricus* hemoglobin (Harrington et al., 1973; Ascoli et al., 1976) and other annelid molecules (Chung & Ellerton, 1979) and closer to the 51-60% reported for *Nephthys* hemoglobin (Messerschmidt et al., 1983)

(j) Subunit Stoichiometry from Amino Acid Compositions

The molar amino acid composition of the chlorocruorin was calculated by fitting the results of amino acid analyses to the M_m corrected for approx. 150 heme groups (3,480 - 92 = 3,388 kDa) and also for the exclusion of Cys, Met, Tyr and Trp, assumed to contribute 9% of remaining mass (3,388 x 0.91 = 3,083) based on the known amino acid sequences of the globin and linker subunits of *Tylorrhynchus* hemoglobin (Table 5). The M_m's of the tetramer and linker subunits were assumed to be 68 kDa and 26.5 kDa, respectively, again based on the known amino acid sequences of *Tylorrhynchus*, *Lamellibrachia* and *Lumbricus* chains (Table 5). Their molar amino acid compositions were also fitted to these values corrected for the assumed 9% contribution of the excluded amino acids (mean of WYMC%M_m for all the chains in Table 5, 8.8 ± 2.2). The calculated molar amino acid compositions were used to calculate the stoichiometry of the tetramer and linker subunits (Kapp et al., 1990b). For any given amino acid *i*, the number of moles of *i* per mole of chlorocruorin is given by:

$$(A_i)_{Chl} = N_T(A_i) + N_L(A_i)$$

where N_T and N_L are the number of copies of the tetramer and linker subunits, respectively. All combinations of equations in the two unknowns were solved either by Gauss-Jordan elimination or by

the least squares method using the interpreted language, APL (Kapp et al., 1990b). The results are presented in Table 6. For 14 amino acids and 2 unknowns, there are 14!/2!(14 - 2)! = 91 possible sets of equations, of which 57 had positive roots, whose means were N_T = 33 ± 11 and N_L = 47 ± 26. For 35 values within ± SD, the means were 34 ± 4 and 43 ± 9, respectively. These results should be compared to 37 and 28, calculated by the least squares method, which uses all of the data. Based on the number of appearances in sets of equations with positive roots, the calculations were repeated using the data from 8 amino acids: Glu, Gly, His, Arg, Ala, Pro, Val and Lys. Out of 28 possible sets of equations, 26 had positive roots with means N_T = 35 ± 8 and N_L = 43 ± 17. For 17 values within ± SD, the means were 34 ± 3 and 44 ± 5, respectively. The least squares solution was 38 and 36, respectively. It is worth noting that the total M_m for 34 tetramers and 44 linkers, 34 x 68 + 44 x 26.5 = 3,478 kDa, is in excellent agreement with the experimental value.

(k) Effect of Dissociation on the Calcium Content of Chlorocruorin

The calcium content of native chlorocruorin (prepared and stored in the presence of 1 mM EDTA) was found to vary between 36 and 81 moles Ca^{2+}/mole protein, with a mean content of 14 determinations being 55 ± 16 (Table 7). It was also found to be unaffected by exposure of the chlorocruorin to additional calcium such as dialysis against 100 and 500 mM $CaCl_2$, followed by dialysis against 1 mM KCl. The Ca^{2+} content of chlorocruorin subjected to dialysis against 0.1M sodium borate buffer pH 9.8, 1mM EDTA and against 4M urea in Tris.Cl buffer, 1mM EDTA at neutral pH, was reduced by 50 and 75%, respectively.

Chlorocruorin passed successively through 1.5 x 11.5 cm columns of mixed bed ion exchange resin (Dowex MR-3, Signa) and Chelex 100 (Sigma) using only water for elution resulted in >90% dissociation of the chlorocruorin (Figure 7, C and D). Surprisingly, the calcium content remained virtually unchanged (Table 7). The elution volumes of peaks B and C corresponded to the elution volumes obtained earlier in the presence of urea (Figure 6A) and their SDS/polyacrylamide gel electrophoretic patterns (not shown) were similar. Since the proportion of peak D in these elution profiles appeared to be smaller than normal, the protein recovery after passage through each of the two columns was determined as well as the SDS/polyacrylamide gel electrophoresis of the total eluted protein. Recovery was incomplete at each chromatographic step (80 to 90%) and there was a deficit of up to 50% in the ca. 30 kDa linker subunit. Thus, in this case, dissociation was probably due to the partially irreversible interaction of the protein with the column matrices.

(l) Effect of Calcium on the Dissociation and Reassociation of *Eudistylia* Chlorocruorin

The proportions of the undissociated (peak A) and the dissociated species (peaks B + C + D) obtained by dissociation in 4M urea at neutral pH in the presence of 0 to 100 mM $CaCl_2$, were estimated from the peak absorbances of the FPLC profiles. Figure 10 (top) shows a plot of % dissociation (B + C + D/ A + B + C + D) as a function of calcium concentration: the dissociation was reduced from >90% to <40% in the presence of 10 to 50 mM Ca^{2+}. Figure 10 (bottom) shows plots of the relative proportions of

peaks B, C and D. The dodecamer was always the major dissociated species present except at the highest calcium concentration. The observed protective effect of calcium in our experiments mirror the reported effect of 10 mM Mg^{2+} on the dissociation of the chlorocruorin at alkaline pH (Terwilliger et al., 1975).

The effect of calcium on the reassociation of the chlorocruorin dissociated in 4M urea at neutral pH, subsequent to removal of urea by dialysis, was also investigated. The results shown in Figure 11 (top) demonstrate a substantial increase in % reassociation (up to 70%) in the surprisingly narrow range of 2.5-5.0 mM Ca^{2+}. The dodecamer was again found to be the major dissociated species present (Figure 11, bottom).

Because of the unexpected decrease in reassociation observed at Ca^{2+} concentrations greater than 5 mM, we considered two possible explanations: (1) an ionic strength effect and (2), the effect of limited chemical degradation of one or more of the chlorocruorin subunits, perhaps as the result of the activation of a latent proteolytic activity. Additional experiments showed that there was a slight decrease in the extent of reassociation in the presence of 0.2M NaCl but not enough to account for the two-fold decrease observed in 50 mM Ca^{2+} (Figure 11, top). Furthermore, the chlorocruorin mixture reassociated in 25 and 50 mM Ca^{2+} showed an increase in reassociation, when the Ca^{2+} concentration was lowered tenfold to 2.5 and 5.0 mM by dilution with buffer and the volume reduced by ultrafiltration to the original value, but again not enough to account totally for the observed decrease in reassociation. These preliminary results suggest that both effects may occur, although there was no apparent difference between the SDS gel electrophoretic patterns of the reassociated chlorocruorin mixture obtained in the absence of Ca^{2+} and in the presence of 50 mM Ca^{2+} (results not shown). Additional work on the effect of Ca^{2+} as well as other divalent cations such as Mg^{2+} and Sr^{2+} is in progress.

The reassociation of peak B (dodecamer) and/or peak C (tetramer) in the presence of peak D (linker) at neutral pH, in the absence and presence of 5 mM and 15 mM $CaCl_2$, was followed using FPLC. There was limited reassociation (generally $<10\%$) to a species eluting at the same volume as the native chlorocruorin. STEM images of negatively stained specimens shown in Figure 1D, indicate that reassociation of the hexagonal bilayer structure was complete. No reassociation was observed in the absence of peak D (linker). Furthermore, reassociation of peak C (tetramer) and peak D (linker) in the presence of Ca^{2+}, was also accompanied by the appearance of a substantial amount (10-20%) of peak B (dodecamer).

DISCUSSION

(a) Molecular Size and Mass

The dimensions of negatively stained molecules of *Eudistylia* chlorocruorin obtained by STEM (Figure 1, A and B) are somewhat smaller than those of *Lumbricus* hemoglobin, 27.5 x 18.5 nm versus 30 x 20 nm, and other hemoglobins such as *Tubifex*, *Arenicola* and *Macrobdella* molecules (Kapp et al., 1982; Kapp & Crewe, 1984; Kapp et al., 1990a) and in agreement with the dimensions obtained for *Myxicola* chlorocruorin (Vinogradov et al., 1985). In contrast, conventional transmission electron microscope studies of annelid extracellular hemoglobins and chlorocruorins had not revealed any differences in size (Terwilliger et al., 1976; Vinogradov et al., 1982). Thus, the significance of the different sizes observed by STEM for negatively stained molecules remains unclear, particularly in view of the equivalence of the

radii of gyration and maximum dimensions obtained in solution by small-angle X-ray scattering (Pilz et al., 1988; Kapp et al., 1990c).

The six M_m values obtained by STEM mass determination for unstained, freeze-dried *Eudistylia* chlorocruorin over three years and with different preparations cluster closely around 3480 kDa with a S.D. of only 26 kDa, even though the average S.D. of the individual determination is 225 kDa. Our result is compared with the literature values for several chlorocruorins in Table 8. It is appropriate to point out that there is a great deal of scatter among the M_m values of annelid hemoglobins in general, and the M_m of *Lumbricus* hemoglobin in particular: the range is from 2,700 kDa to 4,100 kDa (Vinogradov & Kolodziej, 1988). STEM mass determinations have provided M_m for *Lumbricus* hemoglobin from 3,400 to 3,700 kDa (S.N. Vinogradov and J.S. Wall, unpublished observations). In view of the slightly smaller dimensions of *Eudistylia* chlorocruorin a M_m of 3,480 kDa appears reasonable.

(b) Chemical Properties and Subunit Relationships

The chemical structure of the chloroheme of *Eudistylia* chlorocruorin was determined using the modern techniques of NMR and mass spectroscopy in order to be sure that it was identical to the earlier proposed structure of chlorohemes from *Branchiomma*, *Spirographis*, and *Sabella* (Lemberg & Falk, 1951), which had been confirmed by several synthetic studies (Inhoffen et al., 1966, 1969; Jackson et al., 1967). Our study was prompted by several recent results. The synthetic investigations had also produced an 8-formyl derivative whose absorption spectra were indistinguishable from the 3-formyl isomer. Furthermore, it had been shown that nitrimyoglobin, which has a 3-nitrovinyl protoprophyrin IX as the prosthetic group has a visible spectrum similar to chlorocruorins (Bondoc & Timkovich, 1989) and that the active site hemes of the terminal oxidase and the catalase HPII in *E. coli*, which are indistinguishable by visible spectroscopy, have structures that correspond to different geometrical isomers (Chiu et al., 1989).

The iron contents determined by Terwilliger et al. (1975), 0.212wt.% and by us, 0.251wt.% span the range of the published iron contents of about 30 annelid extracellular hemoglobins and chlorocruorins, 0.211 to 0.265 wt.% with a mean of 0.228 ± 0.013 (Vinogradov et al., 1998b). It is likely that the average of the two values, 0.23wt.% is closer to the true iron content of *Eudistylia* chlorocruorin.

The absence of any carbohydrate is in contrast to the ca. 2.1% carbohydrate (mannose:N-glucosamine = 8:1) found in *Lumbricus* hemoglobin (Shishikura et al., 1986). Because no carbohydrate was found in the hemoglobins of the polychaetes *Amphitrite* and *Arenicola* and in *Myxicola* chlorocruorin (E. Yurewicz & S. Vinogradov, unpublished observations) and in the hemoglobin of the leech *Macrobdella* (Kapp et al., 1990a), it is likely that the presence of carbohydrate is restricted to oligochaete molecules.

SDS/polyacrylamide gel electrophoresis of *Eudistylia* chlorocruorin (Figure 4) and of its subunits obtained by mild dissociation at neutral pH (Figure 6) suggests that it consists of two types of subunits: a nonreducible subunit of ca. 30 kDa and a ca. 65 kDa tetrameric subunit. The presence of two types of subunits was observed earlier by Terwilliger et al. (1975) and also in the chlorocruorin of *Myxicola* (Vinogradov et al., 1985). An early study of *Spirographis* chlorocruorin suggested on the basis of N-terminal determination, that it was made up of 34 and 37 kDa chains (Guerritore & Zito, 1971), while SDS/ polyacrylamide gel electrophoresis indicated that the constituent subunits were 14.8 and 15.3 kDa (Di Stefano, 1977). Although the SDS electrophoretic patterns of unreduced, i.e. native chlorocruorins and

hemoglobins are different (Vinogradov, 1985a, 1985b), their patterns in the presence of 2-mercaptoethanol are similar, hinting at a common structure.

The 65 kDa tetramer subunit consists of at least five different, globin chains (chains 4, 5a, 5b, 6 and 7 in Figure 5 and Table 1), of which one, chain 5b probably has a blocked N-terminus. About 25 to 40% of the 65 kDa tetramers consist of aggregated, disulfide-bonded dimers of globin chains (Figure 4, Table 2 and inset in Figure 6A), which upon dissociation of the chlorocruorin form peak C. Knowledge of the amino acid sequences of the five globin chains will be required before their roles in the structure of the tetramer subunit can be ascertained. Although these five chains appear as two bands of equal intensity but slightly differing mobilities corresponding to apparent M_m of 12-14 kDa (bands I and II, Figure 4), their true M_m are probably in the 16-17 kDa range because of the known anomalous mobility of invertebrate globin chains in the presence of SDS (Vinogradov, 1985a) Table 5 compares the M_m of *Lumbricus* and *Tylorrhynchus* globin chains. We assume the average of 17.0 kDa to be the M_m of a *Eudistylia* globin chain and use 68 kDa as the M_m of the tetramer subunit.

The ca. 30 kDa subunit (subunit 1 in Figure 4) consists of at least three nonreducible chains (chains 1, 2 and 3 in Figure 5 and Table 1). Since the SDS/polyacrylamide gel electrophoretic mobility of these chains is analogous to that of the linker chains in the hemoglobins of the polychaete *Tylorrhynchus* and the vestimentiferan *Lamellibrachia*, it is likely that they will have a M_m in the range of 24.9 to 28.2 kDa (Table 5). In our calculations of subunit stoichiometry we use the mean value of 26.5 kDa.

(c) A Dodecamer of Globin Chains is the Principal Subunit of *Eudistylia* Chlorocruorin

The evidence for the existence of a ca. 10 nm particle, representing a ca. 200 kDa subunit of the chlorocruorin is comprised of the following experimental observations. (1) the presence of ca. 10 nm particles in STEM images of negatively stained and unstained, freeze-dried chlorocruorin (Figures 1B and 2A) and their absence in the presence of Ca (Figure 1A). (2) The presence of peak B in gel filtration elution profiles of chlorocruorin dissociated under a variety of conditions, whose elution volume corresponds to a M_m of 196 kDa (Table 3). (3) The presence of large numbers of uniformly shaped particles of ca. 10 nm in STEM images of unstained, freeze-dried peak B (Figure 2C) with a M_m of 208 kDa (Table 3, Figure 8, left) in agreement with the gel filtration estimate. (4) The M_m of 218 kDa (Table 3, Figure 8, left panel) obtained by STEM mass measurements of the ca. 10 nm particles observed in specimens of unstained, freeze-dried chlorocruorin (Figure 2A). (5) The partial dissociation of peak B exposed to 6M Gu.HCl into peak C (Figure 7A), which is known from SDS electrophoresis, gel filtration and STEM mass measurements to consist of 68 kDa tetramers of globin chains (Figure 4, Tables 1 and 3). (6) The presence of an appreciable number of particles, 132 out of a total of 899, which have a mean M_m of 215 kDa in STEM images of unstained, freeze-dried peak C (Figure 2D and Figure 8, right panel), which suggests that they are formed by self-association of the tetramers. (7) The identity of the reduced SDS electrophoretic patterns of peaks B and C (inset Figure 6), which indicates that both subunits are made up of the same globin chains. (8) Peak B was the major component observed in experiments on the effect of Ca on the dissociation and reassociation of the chlorocruorin (Figures 10 and 11 discussed below). Since the experimental values for the M_m of the ca. 10 nm particle are in excellent agreement with the value of 204 kDa expected for a trimer of tetramers (3 x 68 kDa), we believe that the foregoing results

provide a firm foundation for the existence of a dodecamer of chloroheme-containing globin chains in *Eudistylia* chlorocruorin. This conclusion is in accord with recent results demonstrating that a dodecamer of globin chains is the largest functional subunit in the hemoglobin of *Lumbricus terrestris* (Vinogradov et al., 1991a).

Several studies of the dissociation of *Spriographis* chlorocruorin by Chiancone et al. (1981) and by Mezzasalma et al. (1981, 1983, 1986) have provided results which are in general agreement with our findings. Dissociation at alkaline pH provided a major subunit with a sedimentation coefficient of 9.5S (Chiancone et al., 1981) and M_m of 230 kDa (Mezzasalma et al., 1981). Acetylation with acetic anhydride produced subunits of 240 kDa and sulfitolysis of the acetylated material produced subunits of 60, 30, 21 and 15 kDa (Mezzasalma et al., 1986). Furthermore, gel filtration of the apochlorocruorin in 6M Gu.HCl clearly shows the presence of two components, the major one having a M_m of 15 kDa and the other, 30 kDa. Unfortunately, no satisfactory documentation of the SDS electrophoretic patterns of the various chromatographic fractions and of their physical homogeneity have been presented.

The functional role of the dodecamer in *Eudistylia* chlorocruorin is of great interest in view of earlier contradictory findings concerning *Spirographis* chlorocruorin dissociated at alkaline pH: Mezzasalma et al. (1981) reported that the isolated 230 kDa subunit had a higher affinity for oxygen than the native chlorocruorin and an unchanged Hill coefficient, while Giardina et al. (1981) found that the 9.5S subunit had a higher affinity and a decreased Hill coefficient, while Giardina et al. (1981) found that the 9.5S subunit had a higher affinity and a decreased Hill coefficient. In the case of *Lumbricus* hemoglobin, the dodecameric 200 kDa complex, exhibited an unaltered oxygen affinity and a reduced Hill coefficient (Vinogradov et al., 1991a). It should be noted that there exists only one complete study of the oxygen binding equilibria of a chlorocruorin, namely that of *Potamilla* by Imai and Yoshikawa (1985): although chlorocruorins exhibit a cooperativity of oxygen binding comparable to hemoglobins they have a lower oxygen affinity. Interestingly, the allosteric unit inferred within the framework of the Monod-Wyman-Changeux theory is one consisting of six heme groups (Imae et al., 1986). The delineation of the roles of the various subunits of *Eudistylia* chlorocruorin in its structure and in its oxygen binding will require the measurement of their oxygen binding isotherms, currently in progress.

(d) The Role of Calcium in the Quaternary Structure of Eudistylia Chlorocruorin

Figure 1, A and C, demonstrates graphically the important role of Ca^{2+} in the maintenance of the quaternary structure of *Eudistylia* chlorocruorin. A "structural" role for calcium has been invoked many times in the past, predominantly on the basis of its protection of annelid extracellular hemoglobins and chlorocruorins against dissociation at alkaline pH (Antonini & Chiancone, 1977; Chiancone et al., 1976, 1983; Kapp et al., 1984). In addition, it has been shown that other divalent cations, such as Mg^{2+}, Ba^{2+} and Sr^{2+} exert a similar effect (Polidori et al., 1988). Early determinations of calcium in *Lumbricus*, *Tubifex* and *Tylorrhynchus* hemoglobins showed that exposure to 1 mM-10mM EDTA left the molecules with ca. 40 to 60 Ca per mole of protein (Rokjocz & Vinogradov, 1982; Standley et al., 1986). Similar results were obtained in this study (Table 7). Dissociation at pH 9.8 and at neutral pH in 4M urea was accompanied by loss of about 50% and 75% of the intrinsic calcium (Table 7), respectively. Furthermore, the presence of 10 to 25 mM $CaCl_2$ is sufficient to decrease the dissociation of the chlorocruorin in 4M

urea from ca. 100% to about 40% (Figure 10, top). It appears that about 30 to 40 Ca^{2+} ions, located perhaps at sites between the dodecamer and linker subunits, are involved in the maintenance of the native hexagonal bilayer structure. Attempts at complete removal of calcium by passage through a mixed bed resin column followed by a Chelex 100 column, showed that there was no loss of the intrinsic calcium (Table 7): the complete dissociation of the molecule was evidently due to partially irreversible interaction, particularly of the linker subunits, with the column matrices.

In accordance with its protective effect against dissociation of the chlorocruorin in 4M urea, the presence of calcium enhances the reassociation of the native hexagonal bilayer structure upon removal of the dissociating agent (Figure 11, top). The unexpected observation was the occurrence of maximum reassociation over the narrow range of 2.5-5mM Ca^{2+}. Enhancement of reassociation in the presence of 35 mM Ca^{2+} subsequent to dissocaition at alkaline pH and return to neutral pH, had also been observed in the case of *Spirographis* chlorocruorin (Chiancone et al., 1981). The decrease in the extent of reassociation at higher calcium concentration appears to be caused by an ionic strength effect as well as chemical degradation due probably to the calcium-mediated activation of a proteolytic activity latent in the presence of 1 mM EDTA.

Very limited (<10%) reassociation of the isolated dodecamers and tetramers in the absence and presence of 5 and 15 mM Ca^{2+}, occurs only in the presence of the linker subunit, as demonstrated by FPLC (not shown) and by STEM. The images of the negatively stained reassociated structures appear to be similar to those of the native chlorocruorin (Figure 1D). There appears to be no difference between the products of reassociation from either the dodecamer or the tetramer. Furthermore, reassociation of tetramer and linker in the presence of 5 mM Ca^{2+} leads to the formation of substantial (10-20%) amounts of dodecamer.

(e) Quaternary Structure of *Eudistylia* Chlorocruorin: a Hierarchy of Globin Complexes

Due to the symmetrical hexagonal appearance of annelid hemoglobins and chlorocruorins in electron micrographs, the generally held view has been that they consisted of twelve hexadecamers of globin chains (192-chain model; Suzuki & Gotoh, 1986; Fushitani & Riggs, 1988; Gotoh & Suzuki, 1990). We have demonstrated for both *Lumbricus* and *Macrobdella* hemoglobins (Vinogradov et al, 1986; Kapp et al., 1990a) and now for *Eudistylia* chlorocruorin, that these molecules are heteromultimeric, consisting of both ca. 17 kDa and ca. 30 kDa subunits. Since the overwhelming majority of SDS gel electrophoretic patterns of the hexagonal bilayer hemoglobins which have been published show clearly the presence of the two types of subunits, it appears safe to conclude that the foregoing conclusion holds for all members of the class.

Because the electron microscopic appearance of *Eudistylia* chlorocruorin is so similar to that of *Lumbricus* hemoglobin (Figure 1), it is plausible to assume that it would also possess D_6 symmetry, inferred for the latter from crystal structure data (Royer & Hendrickson, 1988). Consequently, it is logical to assume that twelve large complexes of globin chains form the principal element of their structures. The results obtained earlier for *Lumbricus* hemoglobin (Vinogradov et al., 1991a) and now for *Eudistylia* chlorocruorin, demonstrate clearly that this large complex is a dodecamer and not a hexadecamer of globin chains. Thus, we can consider that the cornerstone of the quaternary structure of these two dissimilar yet alike, molecules is the presence of twelve dodecamers of globin chains carrying a total of 144 heme groups.

The electrophoretic results obtained in this study (Table 2) and by Terwilliger et al. (1975) suggest strongly that the globin chains account for 72 to 76% of the total molecule. That the heme-deficient linker subunits account for 24 to 28% of the whole chlorocruorin, dovetails with the iron content which is 75% of the normal value of 0.33% (1 heme group/17 kDa). The experimental iron content of 0.251 wt% corresponds to 156 heme groups for M_m = 3,480 kDa. The subunit stoichiometry results obtained in this study (Tables 2 and 6) are consistent with there being 30-40 linker subunits, one or more of whose chains contain(s) the additional 12 heme groups.

Table 9 presents several possible distributions of mass and heme in *Eudistylia* chlorocruorin based on the following assumptions: (1), that the functional moiety is represetned by twelve complexes of globin chains, (2), that the M_m of the globin chains is 17 ± 0.5 kDa and that the M_m of the linker chains is 26.5 ± 1.7 kDa (Table 5) and (3), that the proportion of globin to linker subunits is between 0.7:0.3 and 0.75:0.25. The calculated M_m and iron contents of the models have to be compared to the experimental M_m = 3,480 ± 225 kDa and the iron contents, our value of 0.251 wt.% and the 0.212 wt.% reported earlier (Terwilliger et al., 1975).

Model A represents the 192-chain model proposed for *Tylorrhynchus* hemoglobin (Gotoh & Suzuki, 1986, 1990) and *Lumbricus* hemoglobin (Gotoh & Suzuki, 1986, 1990) and *Lumbricus* hemoglobin (Fushitani & Riggs, 1988), calculated for a globin to linker ratio of 0.75:0.25. It can be seen that the resulting mass and the calculated iron content are appreciably higher than the experimental values. The mass left for the linker subunits would allow only 8 to 16 linker chains per molecule of protein. These considerations, together with the evidence produced for the existence of a dodecameric complex in *Eudistylia* chlorocruorin in this work and in *Lumbricus* hemoglobin earlier (Vinogradov et al., 1991a) make the 192-chain model an unlikely one.

Model B, based on 12 dodecamers, fixing the contribution of the globin chains to 2,424 kDa and assuming a globin to linker ratio of 0.75:0.25, provides a M_m which is too low. Model C, calculated using a globin to linker ratio of 0.7:0.3, provides a M_m in excellent agreement with the experimental STEM value and an iron content that is between our value and that of Terwilliger et al. (1975). Of particular note is the good agreement between the calculated stoichiometries of the tetramer and linker subunits (Table 9) with the experimental values obtained in the present study: the SDS electrophoretic values for reduced and reduced/carboxymethylated chlorocruorin in Table 2 (N_T = 38 ± 5, 38 ± 2 and N_L = 34 ± 10, 33 ± 3) and the values calculated from molar amino acid compositions in Table 6 (N_T = 34 ± 4, 37 and 34 ± 3, 36 and N_L = 43 ± 9, 28 and 44 ± 5, 38). It is evident that the experimental results obtained in this study, namely the M_m of the chlorocruorin (3,480 ± 170 kDa), the M_m of the dodecamer (207 ± 11 kDa, average of the 3 values in Table 3), the iron content of 0.251 ± 0.021wt.% and the ratio of globin to linker (0.74:0.26 ± 0.08) can accomodate substantial variation in the calculated stoichiometry of the linker subunits.

Finally, it is necessary to consider here the implication of the results obtained from circular dichroism measurements of the chlorocruorin and its subunits over the 200-250 nm range shown in Figure 9 and Table 4. The similarity of the alpha helix values for the chlorocruorin and the dodecamer suggest that their secondary structures are similar. In contrast, there appears to exist a considerable difference in alpha-helical content between the dodecamer and the isolated tetramer, suggesting that an alteration in secondary structure may accompany its dissociation from the dodecamer. The linker subunit, on the other hand, exhibits much less alpha-helical structure than the tetramer or the dodecamer, as might be expected of a heme-deficient, chimeric globin chain by analogy with the linker chains of *Tylorrhynchus* and *Lamellibrachia* hemoglobins, which appear to be chimeric products of a globin gene duplication event accompanied by loss of all or part of exon 1 in the N-terminal globin moiety and of exon 3 of the other

globin moiety (Suzuki et al., 1990a, 1990b). There is no data available on the extent of heme binding in such chimeric globin chains. Partial heme occupancy has been documented in the two-domain, multisubunit, extracellular hemoglobin of *Ascaris* (Darawshe et al., 1987) and appears also to exist in the hemoglobin of the closely related nematode *Pseudoterranova* (Dison et al., 1991). Although the complete cDNA sequence of the latter is known, it does not provide a clearcut expanation for the deficiency in heme binding.

In conclusion, *Eudistylia* chlorocruorin can be viewed as a hierarchy of complexes of chloroheme-containing globin chains which have retained most if not all of the typical "myoglobin fold" conformation, linked together by 30-40 chimeric, chloroheme-deficient globin chains and an approximately equal number of calcium atoms.

References

Antonini, E., Rossi-Fanelli, A. and Caputo, A. (1962a) *Arch. Biochem. Biophys.* **97**, 336-342.

Antonini, E., Rossi-Fanelli, A. and Caputo, A. (1962b) *Arch. Biochem. Biophys.* **97**, 343-350.

Antonini, E. and Chiancone, E. (1977) *Annu. Rev. Biophys. Bioeng.* **6**, 239-271.

Ascoli, F., Chiancone, E. and Antonini, E. (1976) *J. Mol. Biol.* **105**, 343-351.

Ball, E. H. (1986) *Anal. Biochem.* **155**, 23-27.

Bhatti, R., Chambers, R. E. and Clamp, J. R. (1979) *Biochim. Biophys. Acta* **957**, 370-379.

Boekema, E. J. and Van Heel, M. (1989) *Biochim. Biophys. Acta* **957**, 370-379.

Bondoc, L. L. and Timkovich, R. (1989) *J. Biol. Chem.* **264**, 6134-6145.

Cameron, B. F. (1970) *Anal. Biochem.* **35**, 515-520.

CaJacob, C. A., Frey, P. A., Hainfeld, J. F., Wall, J. S. and Yang, H. (1985) *Biochemistry* **24**, 2425-2431.

Chen, Y. H., Yang, J. T. and Martinez, H. M. (1972) *Biochem.* **11**, 4120-4131.

Chiancone, E., bull, T. E., Norne, J. E., Foorsen, S. and Antonini, E. (1976) *J. Mol. Biol.* **107**, 25-34.

Chiancone, E., Vecchini, P., Ascoli, F., Verzili, D. and Antonini, E. (1981) In *Invertebrate Oxygen Binding Proteins* (Lamy, J. and Lamy, J., eds.), pp. 49-57, Marcel Dekker, Inc., New York.

Chiancone, E., Vecchini, P., Ascoli, F. and Antonini, E. (1983) *Life Chem. Reports, Suppl. 1*, 205-209.

Chiu, J. T., Loewen, P. C., Switala, J., Gennis, R. B. and Timkovich, R. (1989) *J. Am. Chem. Soc.* **111**, 7046-7050.

Chung, M. C. C. and Ellerton, H. D. (1979) *Progr. Biophys. Mol. Biol.* **35**, 51-102.

Crestfield, A. M., Moore, S. and Stein, W. H. (1963) *J. Biol. Chem.* **239**, 622-627.

Darawshe, S., Tsfadyah, Y. and Daniel, E. (1987) *biochem. J.* **242**, 689-694.

DiStefano, M. V., Piazzese, S. and Russo, G. C. (1977) *FEBS Lett.* **79**, 337-339.

Dixon, B., Walker, B., Kimmins, W. and Pohajdak, W. (1991) *Proc. Natl. Acad. Sci. U.S.A.* (in press).

Edelhoch, H. (1967) *Biochemistry* **6**, 1948-1954.

Fushitani, K. and Riggs, A. F. (1988) *Proc. Nat. Acad. Sci. U.S.A.* **85**, 9461-9463.

Fushitani, K., Matsuura, M. S. A. and Riggs, A. F. (1988) *J. Biol. Chem.* **263**, 6502-6517.

Ghiretti-Magaldi, A., Ghiretti, F., Tognon, G. and Zanotti, G. (1986) In *Invertebrate Oxygen Carriers*, (Linzen, B., ed.) pp. 45-49, Springer-Verlag, Berlin.

Giardina, B., Chiancone, E., Ascoli, F. and Antonini, E. (1981) In *Invertebrate Oxygen Binding Proteins* (Lamy, J. and Lamy, J., eds.) pp. 659-664, Marcel Dekker, New York.

Gotoh, T. and Suzuki, T. (1990) *Zool. Sci.* **7**, 1-16.

Guerritore, D., Bonacci, M. L., Brunori, M., Antonini, E., Wyman, J. and Rossi-Fanelli, A. (1965) *J. Mol. Biol.* **13**, 234-237.

Guerritore, D. and Zito, R. (1971) *Biochim. Biophys. Acta* **229**, 720-723.

Hanania, G. I. H., Yegiayan, A. and Cameron, B. (1966) *Biochem. J.* **98**, 189-192.

Harrington, J. P., Pandolfelli, E. R. and Herskovits, T. T. (1973) *Biochim. Biophys. Acta* **238**, 61-73.

Hendrickson, R. I. and Meredith, S. C. (1984) *Anal. Biochem.* **136**,65-74.

Himmel, M. E. and Squire, P. G. (1981) *J. Chromatog.* **210**, 443-452.

Imai, K. and Yoshikawa, S (1985) *Eur. J. Biochem.* **147**, 453-463.

Imai, K., Yoshikawa, S., Fushitani, K., Takizawa, H., Handa, T. and Kihara, H. (1986) In *Invertebrate Oxygen Carriers* (Linzen, B., ed.) pp. 367-374, Springer-Verlag, Berlin.

Inhoffen, H. H., Bliesener, C. and Brockmann, H. (1966) *Tet. Lett.* **31**, 3779-3785.

Inhoffen, H. H., Brockmann, H. and Bliesener, K. (1969) *J. Liebigs Ann. Chem.* **730**, 173-185.

Jackson, A. H., Kenner, G. W. and Wass, J. (1967) *J. Chem. Soc. Chem. Commun.*, 1027-1029.

Kapp, O. H., Vinogradov, S. N., Ohtsuki, M. and Crewe, A. V. (1982) *Biochim. Biophys. Acta* **704**, 546-548.

Kapp, O. H. and Crewe, A. V. (1984) *Biochim. Biophys. Acta* **789**, 294-301.

Kapp, O. H., Polidori, G., Mainwaring, M. G., Crewe, A. V. and Vinogradov, S. N. (1984) *J. Biol. Chem.* **259**, 628-639.

Kapp, O. H., Qabar, A. N., Bonner, M. C., Stern, M. S., Walz, D. A., Schmuck, M., Pilz, I., Wall, J. S. and Vinogradov, S. N. (1990a) *J. Mol. Biol.* **213**, 141-158.

Kapp, O. H., Qabar, A. N. and Vinogradov, S. N. (1990b) *Anal. Biochem.* **184**, 74-82.

Kapp, O. H., Schmuck, M., Pilz, I. and Vinogradov, S. N. (1990c) In *Invertebrate Dioxygen Binding Proteins* (Preaux, G., and Lontie, R., eds.), pp. 219-224, Leuven University Press, Leuven.

Laemmli, U. (1970) *Nature* **227**,680-685.

Lemberg, R. and Falk, J. E. (1951) *Biochem. J.* **49**, 674-683.

Mainwaring, M. G., Lugo, S., Fingal, R., Kapp, O. H. and Vinogradov, S. N. (1986) *J. Biol Chem.* **261**, 10800-10908.

Mangum, C. (1976) In *Adaptations to Environment: Physiology of Marine Animals* (Newell, P. C., ed.), pp. 191-278, Butterworth's, London.

Messerschmidt, U., Wilhelm, P., Pilz, I., Kapp, O. H. and Vinogradov, S. N. 91983) *Biochim. Biophys. Acta* **742**, 366-373.

Mezzasalma, V., DiStefano, L., Russo, G. C. and Salvato, B. (1981) In *Invertebrate Oxygen Binding Proteins* (Lamy, J. and Lamy, J., eds.), pp. 665-676, Marcel Dekker, New York.

Mezzasalma, V., DiStefano, L., Piazzese, S., Zagra, M., Ghiretti-Magaldi, A., Carbone, R. and Salvato, B. (1983) *Life Chem. Rep., Supp. 1*, 187-191.

Mezzasalma, V., Zagra, N., DiStefano, L. and Salvato, B. (1986) In *Invertebrate Oxygen Carriers* (Linzen, B., ed.), pp. 65-68, Springer-Verlag, Berlin.

Orii, Y. and Washio, N. (1977) *J. Biochem.* **81**, 495-503.

Padavanija, P. and Timkovich, R. (1986) *J. Chem. Soc. Perkin Trans.* **II**, 1785-1787.

Pilz, I., Schwarz, E., Suzuki, T. and Gotoh, T. (1988) *Int. J. Biol. Macromol.* **10**, 356-360.

Polidori, G., Mainwaring, M. G. and Vinogradov, S. N. (1988) *Biochem. Physiol.* **89A**, 541-545.

Qabar, A. N., Kapp, O. H., Wall, J. S. and Vinogradov, S. N. (1991) In *Structure and Function of Invertebrate Oxygen Binding Proteins* (Vinogradov, S. N. and O. H. Kapp, eds.), pp. 81-90, Springer-Verlag, New York.

Rokocz, M. and Vinogradov, S. N. (1982) *Biochim. Biophys. Acta* **707**, 291-293.

Royer, W. E., Jr. and Hendrickson, W. A. (1988) *J. Biol. Chem.* **263**, 13762-13765.

Shishikura, F., Mainwaring, M. G., Yurewicz, E., Lightbody, J. L., Walz, D. A. and Vinogradov, s. N. (1986) *Biochim. Biophys. Acta* **869**, 314-321.

Shishikura, F., Snow, J., Gotoh, T., Vinogradov, S. N. and Walz, D. A. (1987) *J. Biol. Chem.* **262**, 3123-3131.

Standley, P. N., Mainwaring, M. G., Gotoh, T. and Vinogradov, S. N. (1988) *Biochem. J.* **249**, 915-916.

Suzuki, T., Takagi, T. and Gotoh, T. (1982) *Biochim. Biophys. Acta* **708**, 253-258.

Suzuki, T., Furukohri, T. and Gotoh, T. (1985a). *J. Biol. Chem.* **260**,3145-3154.

Suzuki, T., Yasunaga, H., Furukohri, T., Nakamura, K. and Gotoh, T. (1985b) *J. Biol. Chem.* **260**, 11481-11487.

Suzuki, T. and Gotoh, T. (1986a) *J. Biol. Chem.* **261**, 9257-9267.

Suzuki, T. and Gotoh, T. (1986b) *J. Mol. Biol.* **190**, 119-123.

Suzuki, T., Takagi, T. and Gotoh, T. (1990a) *J. Biol. Chem.* **265**, 12168-12177.

Suzuki, T., Takagi, T. and Ohta, S. (1990b) *J. Biol. Chem.* **265**, 1551-1555.

Teale, F. W. J. (1959) *Biochim. Biophys. Acta* **35**, 43-45.

Terwilliger, R. C. (1980) *Amer. Zool.* **20**, 53-67.

Terwilliger, R. C., Garlick, R., Terwilliger, N. B. and Blair, D. P. (1975) *Biochim. Biophys. Acta* **400**, 302-309.

Terwilliger, R. C., Terwilliger, N. B. and Schabtach, E. (1976) *Comp. Biochem. Physiol.* **55A**, 51-55.

Timkovich, R., Cork, M. S. and Taylor, P. V. (1984) *J. Biol. Chem.* **259**, 1577-1585.

Timkovich, R., Cork, M. S., Gennis, R. B. and Johnson, P. Y. (1985) *J. Am. Chem. Soc.* **107**, 6069-6075.

Vinogradov, S. N. (1985a) *Comp. Biochem. Physiol.* **82B**, 1-15.

Vinogradov, S. N. (1985b) In *Respiratory Pigments in Animals* (Lamy, J., Truchot, J. P. and Gilles, R., eds.), pp. 9-20, Springer-Verlag, Berlin.

Vinogradov, S. N. (1986a) *Meth. Enzymol.* **123**, 320-323.

Vinogradov, S. N. (1986b) In *Invertebrate Oxygen Carriers* (Linzen, B., ed.), pp. 25-36, Springer-Verlag, Berlin.

Vinogradov, S. N., Shlom, J. M., Hall, B. C., Kapp, O. H. and Mizukami, H. (1977) *Biochim. Biophys. Acta* **492**, 136-155.

Vinogradov, S. N., Hersey, S. L., Frohman, C. and Kapp, O. H. (1979) *Biochim. Biophys. Acta* **578**, 216-222.

Vinogradov, S. N. and Orii, Y. (1980) *Comp. Biochem. Physiol.* **67B**, 183-185.

Vinogradov, S. N., Shlom, J. M., Kapp, O. H. and Frossard, P. (1980a) *Comp. Biochem. Physiol.* **67B**, 1-16.

Vinogradov, S. N., Kosinski, T. and Kapp, O. H. (1980b) *Biochim. Biophys. Acta* **621**, 315-323.

Vinogradov, S. N., Kapp, O. H. and Ohtsuki, M. (1982) In *Electron Microscopy of Proteins* (Harris, J., ed.), vol. 3, pp. 135-163, Academic Press, New York.

Vinogradov, S. N., Standley, P. R., Mainwaring, M. G., Kapp, O. H. and Crewe, A. V. (1985) *Biochim. Biophys. Acta* **828**, 43-50.

Vinogradov, S. N., Lugo, S., Mainwaring, M. G., Kapp, O. H. and Crewe, A. V. (1986) *Proc. Nat. Acad. Sci. U.S.A.* **83**, 8034-8038.

Vinogradov, S. N. and Kolodziej, P. (1988) *Comp. Biochem. Physiol.* **91B**, 577-579.

Vinogradov, S. N., Sharma, P. K., Qabar, A. N., Wall, J. S., Westrick, J. A., Simmons, J. H. and Gill, S. J. (1991a) *J. Biol. Chem.* (in press).

Vinogradov, S. N., Sharma, P. K. and Walz, D. A. (1991b) *Comp. Biochem. Physiol.* **98B**, 187-194.

Wall, J. S. and Hainfeld, J. F. (1986) *Annu. Rev. Biophys. Biophys. Chem.* **15**, 355-376.

Wall, J. S., Hainfeld, J. F., Bartlett, P. A. and Singer, D. J. (1982) *J. Ultramicrosc.* **8**, 397-402.

Walz, D. A., Snow, J., Mainwaring, M. G. and Vinogradov, S. N. (1987) *Proc. Fed. Amer. Soc. Exp. Biol.* **46**, 2266.

Waxman, L. (1971) *J. Biol. Chem.* **246**, 7318-7327.

Waxman, L. (1975) *J. Biol. Chem.* **250**, 3790-3795.

Weber, R. (1978) In *Physiology of Annelids* (Mill, P. J., ed.), pp. 393-446, Academic Press, London.

Figure 1.

STEM images of negatively stained specimens. General field of view of *Eudistylia* chlorocruorin: (A) in 50 mM $CaCl_2$ and, (B), in the absence of Ca. Galleries of individual molecules: (C) chlorocruorin peak B and (D), reassociation product of peaks B and D. The dimensions for A, B and D are 199 x 199 nm. The arrow in (B) points to an individual particle such as the ones portrayed in (C) at approximately 3.4 fold magnification.

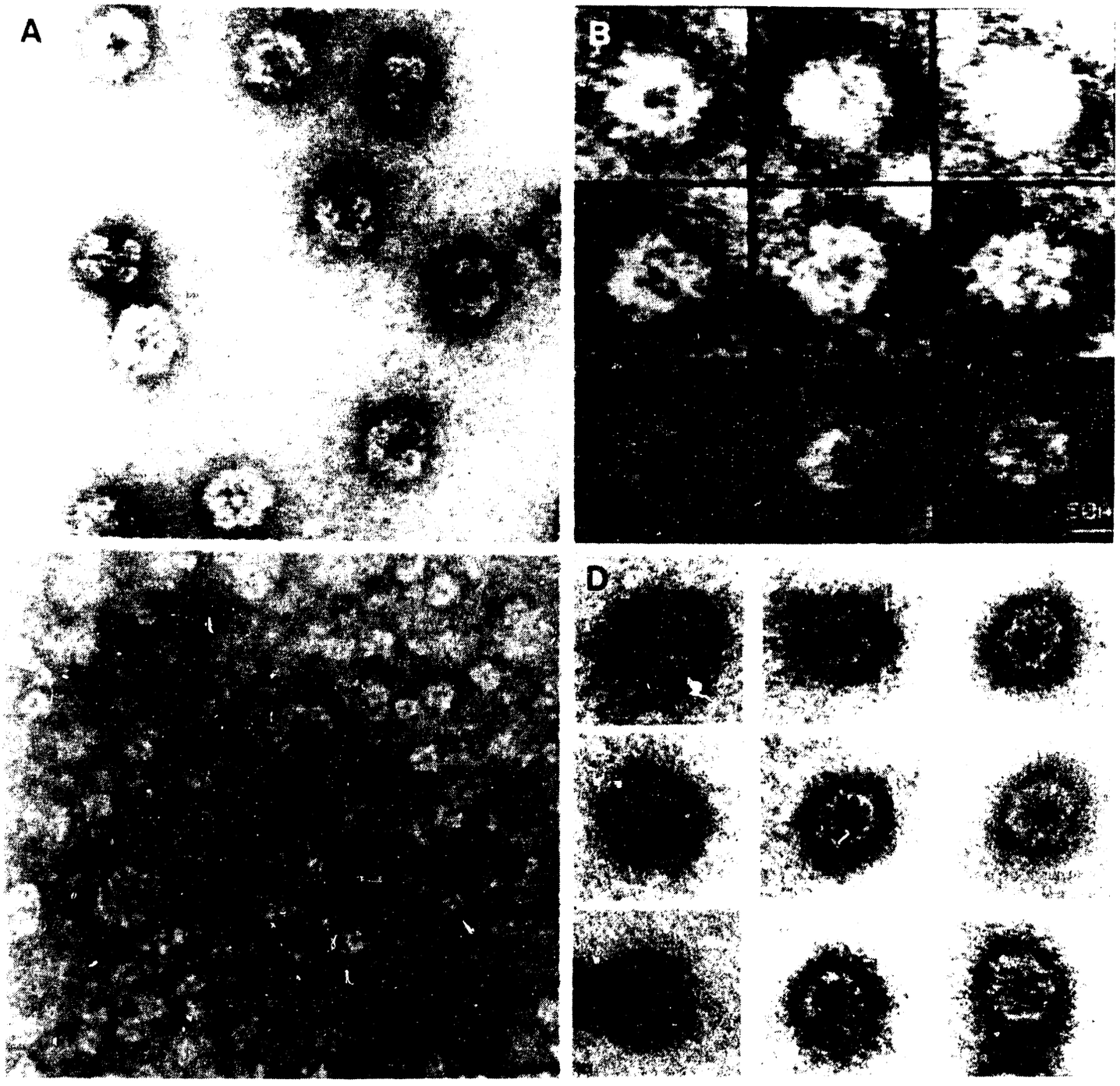
A
B
D

Figure 2.

STEM images of unstained, freeze-dried specimens. (A) *Eudistylia* chlorocruorin; (B) Crosslinked chlorocruorin; (C) and (D), Peaks B and C, respectively, of chlorocruorin obtained by gel filtration subsequent to dissociation in 4M urea at neutral pH (Figure 6, B and C). Dimensions are 1024 x 1024 nm for (A) and 512 x 512 nm for (B), (C) and (D).

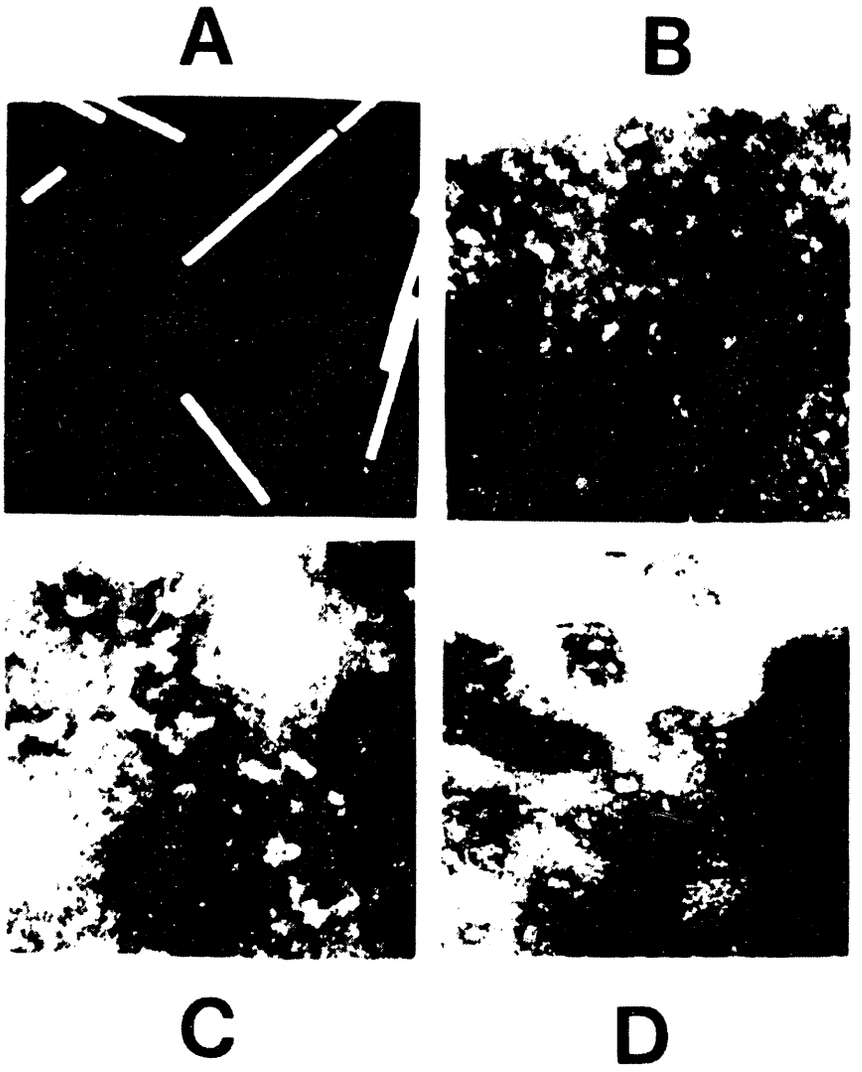
A
B
C
D

Figure 3.

Histograms of M_m obtained by STEM mass measurements of unstained, freeze-dried specimens: (A), native chlorocruorin; (B), small particles observed in specimens of native chlorocruorin. A representative STEM image is provided in Figure 2A.

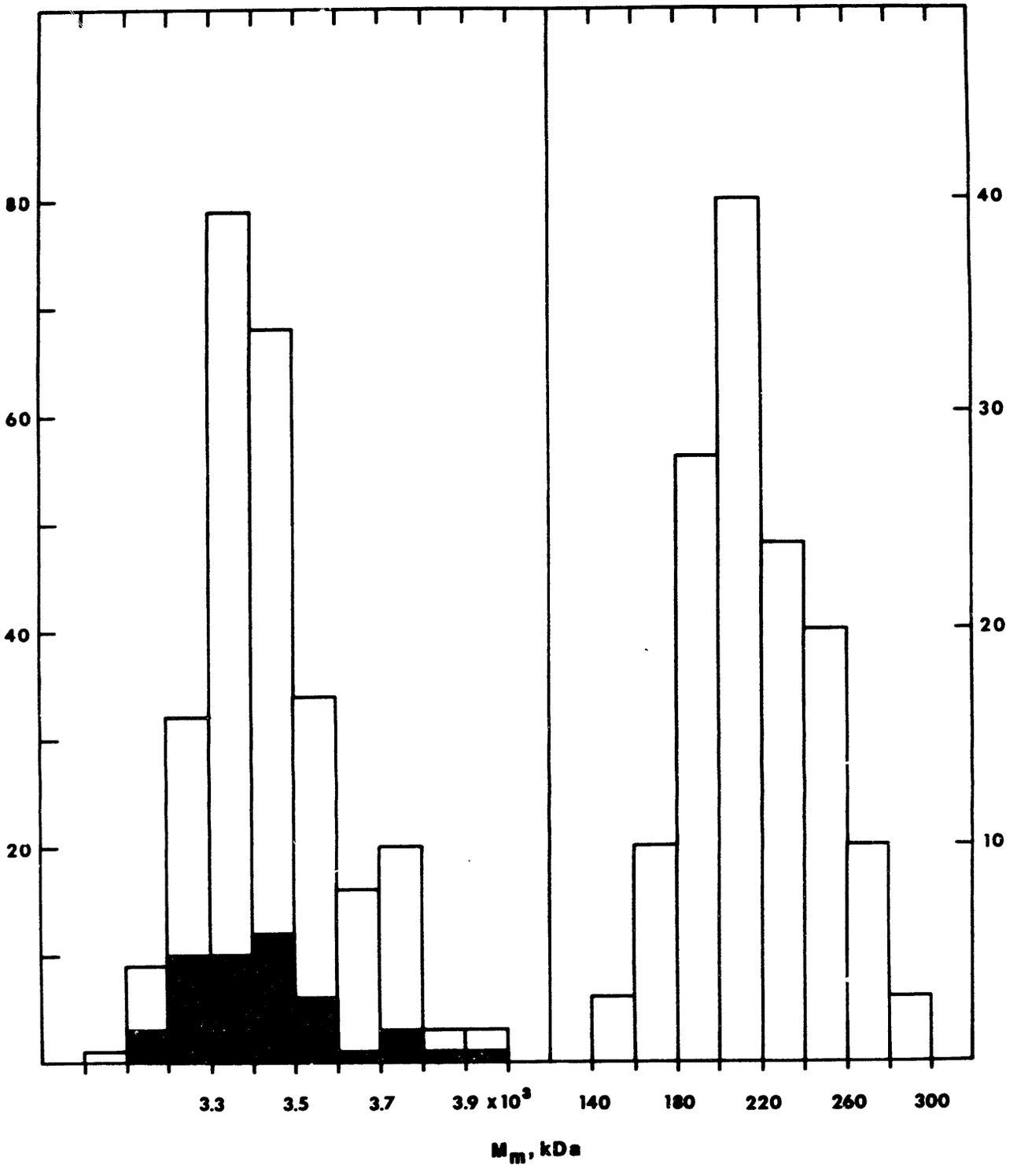
80
60
40
20
40
30
20
10
3.3
3.5
3.7
3.9 x10³
140
180
220
260
300
Mm, kDa

Figure 4.

SDS/polyacrylamide gel electrophoretic patterns of (A), unreduced, i.e. native, *Lumbricus* hemoglobin, (B), unreduced and (C), reduced *Eudistylia* chlorocruorin; (D) reduced *Lumbricus* hemoglobin. The arrows indicate the relationships between the subunits of the native and reduced chlorocruorin. The corresponding relationships in *Lumbricus* hemoglobin are $M \rightarrow I$, $D1 \rightarrow V$, $D2 \rightarrow VI$ and $T \rightarrow II + III + IV$.

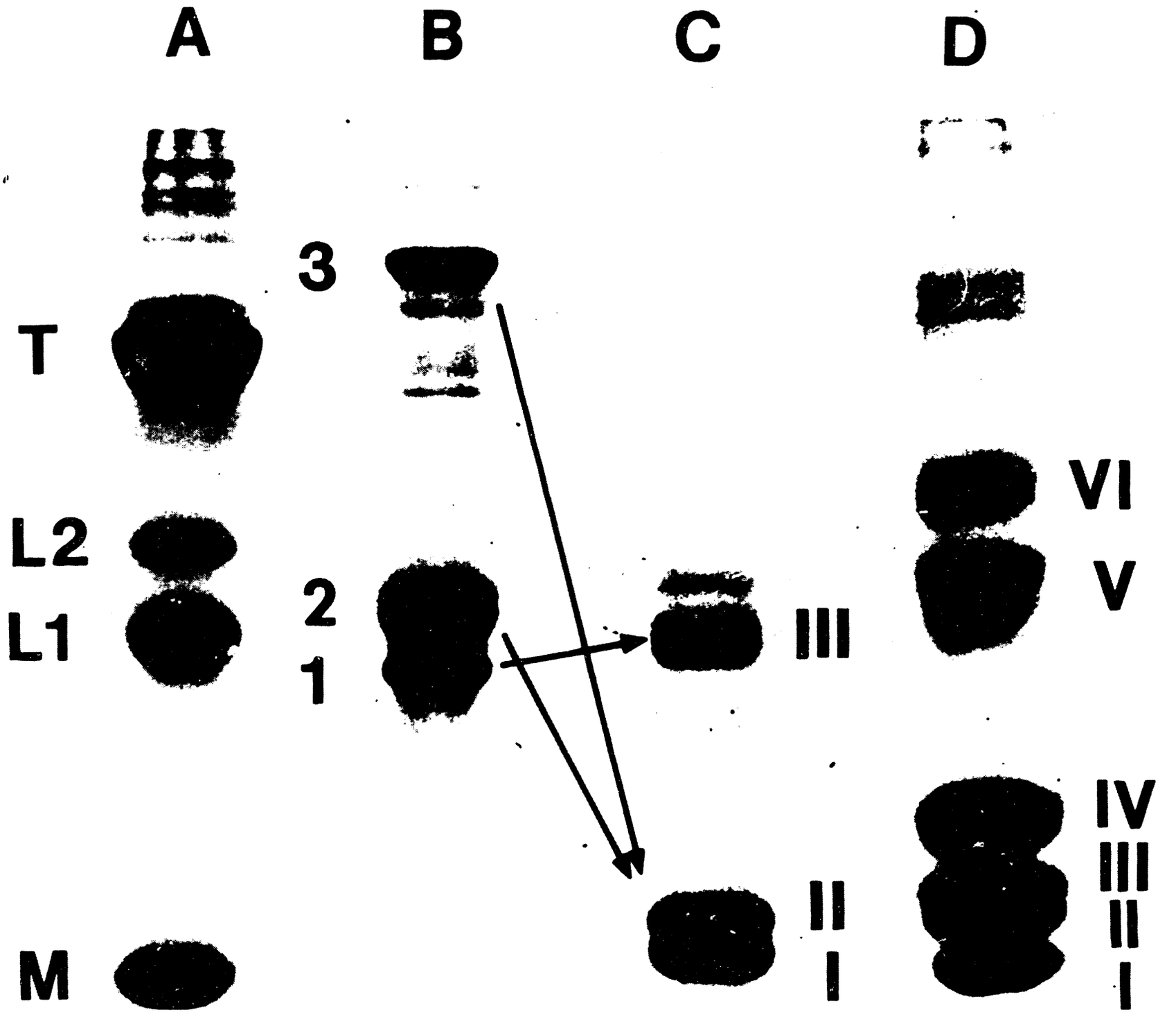
A
B
C
D
T
L2
L1
M
3
2
1
III
II
I
VI
V
IV
III
II
I

Figure 5.

Reversed phase chromatography of reduced, carboxymethylated chlorocruorin on a C_{18} column (RPCHR5/5, Pharmacia), using a 30 to 60% acetonitrile gradient in 0.1% trifluoroacetic acid.

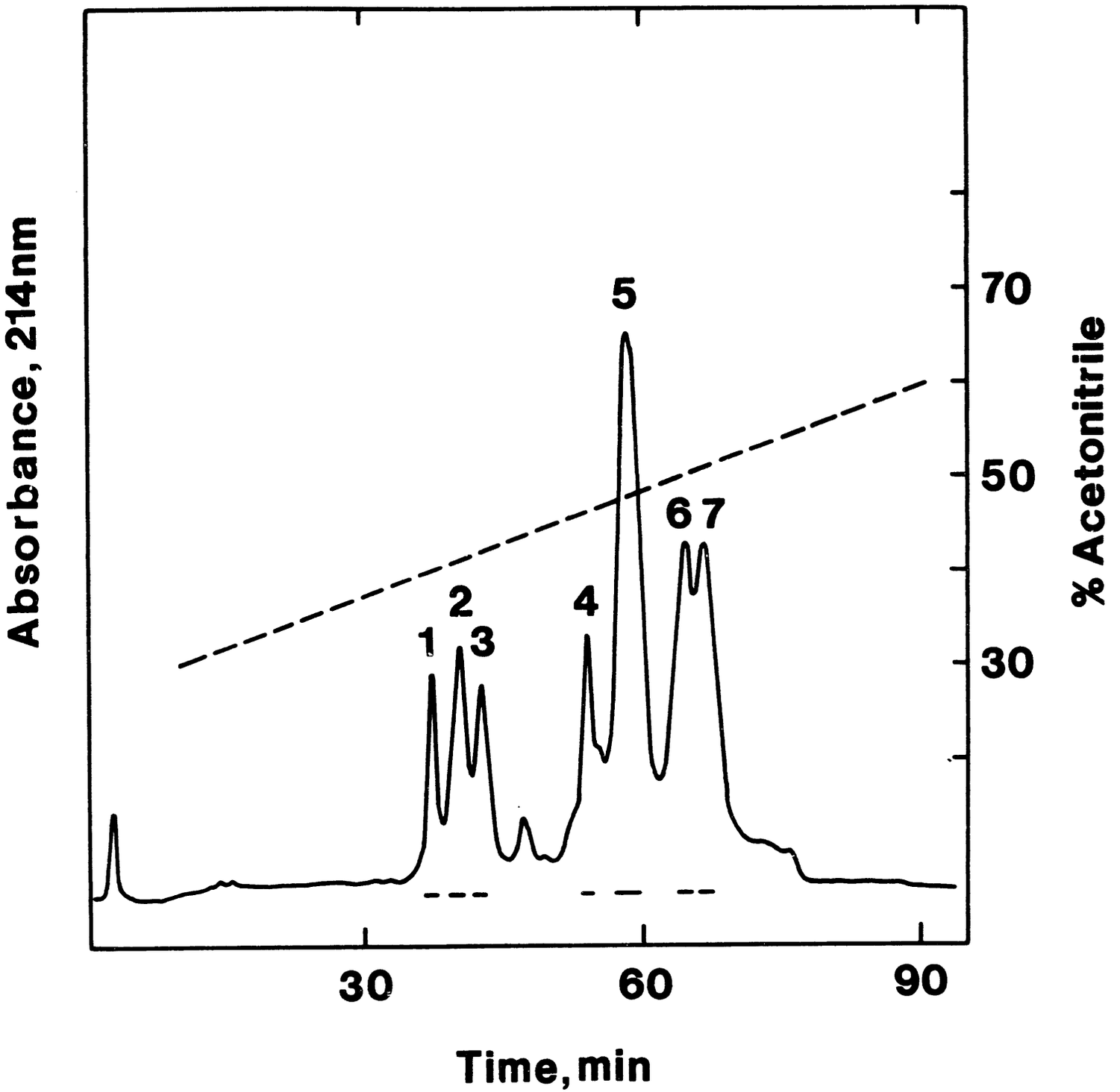
Absorbance, 214nm
% Acetonitrile
70
50
30
1
2
3
4
5
6
7
30
60
90
Time, min

Figure 6.

FPLC elution profiles at 280 nm obtained with a 1 × 30 cm column of Superose S-12: (A), chlorcruorin in 0.1 M Tris.Cl buffer pH 7.2, 1 mM EDTA following dialysis against 4M urea in the same buffer; (B), (C) and (D), elution profiles at neutral pH of pooled fractions under peaks B, C and D, respectively, obtained by preparative gel filtration at neutral pH, on a 5 × 100 cm column of Sephadex G-100, following dissociation of the chlorocruorin in 4M urea. The insets provide the SDS/polyacrylamide gel electrophoretic patterns of the chlorocruorin (lane 1, unreduced and lane 8, reduced) and peaks B, C and D (lanes 2-4, unreduced and lanes 5-7, reduced).

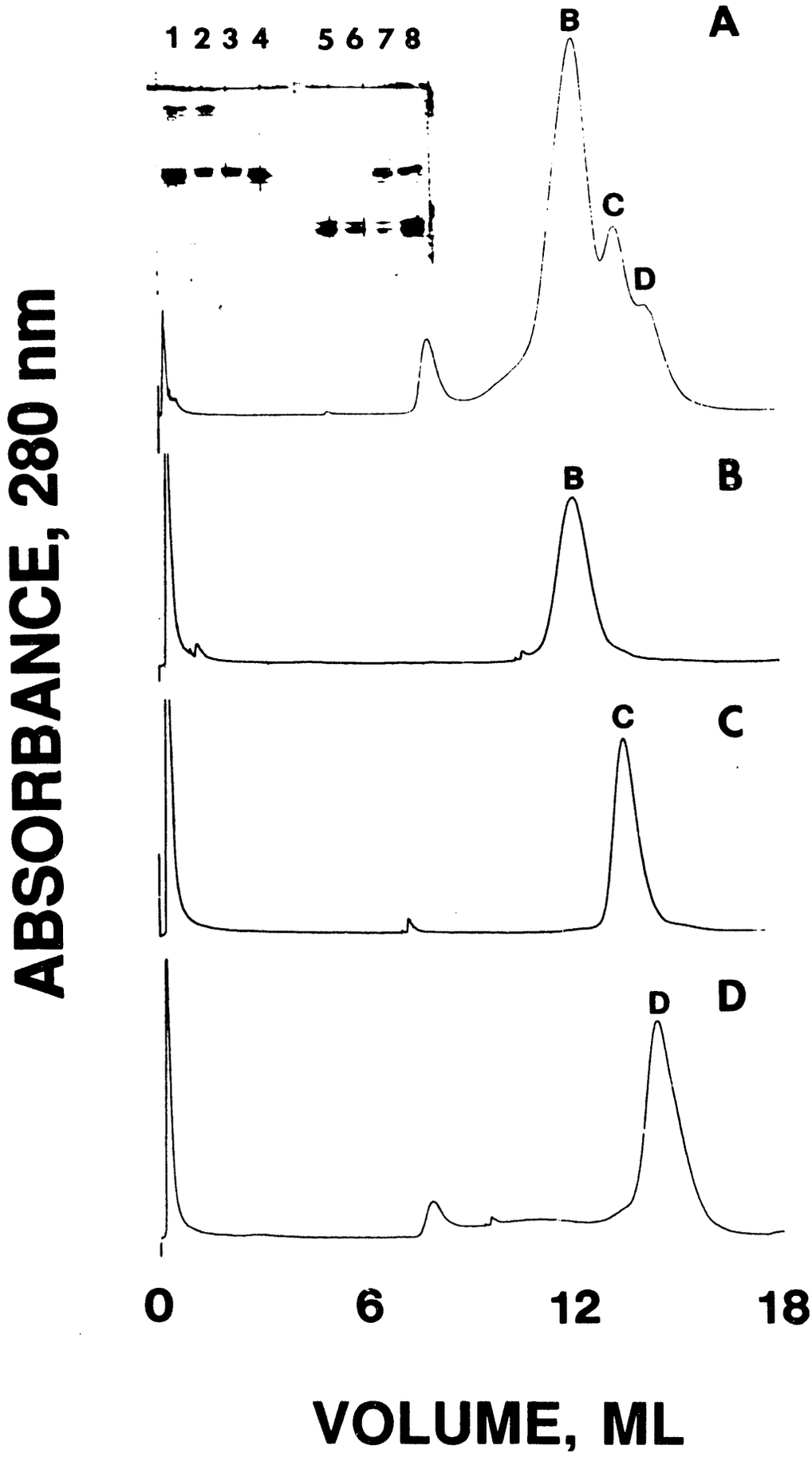
1 2 3 4 5 6 7 8
A
B
C
D
B
B
C
C
D
D
ABSORBANCE, 280 nm
0
6
12
18
VOLUME, ML

Figure 7.

FPLC elution profiles at 280 nm obtained with a 1 × 30 cm column of Superose S-12 at neutral pH: (A), peak B from Figure 6B exposed to 6M Gu.HCl; (B), native chlorocruorin; (C), chlorocruorin passed through a column of mixed bed ion-exchange resin and (D), chlorocruorin passed successively through columns of mixed bed ion-exchange resin and Chelex 100.

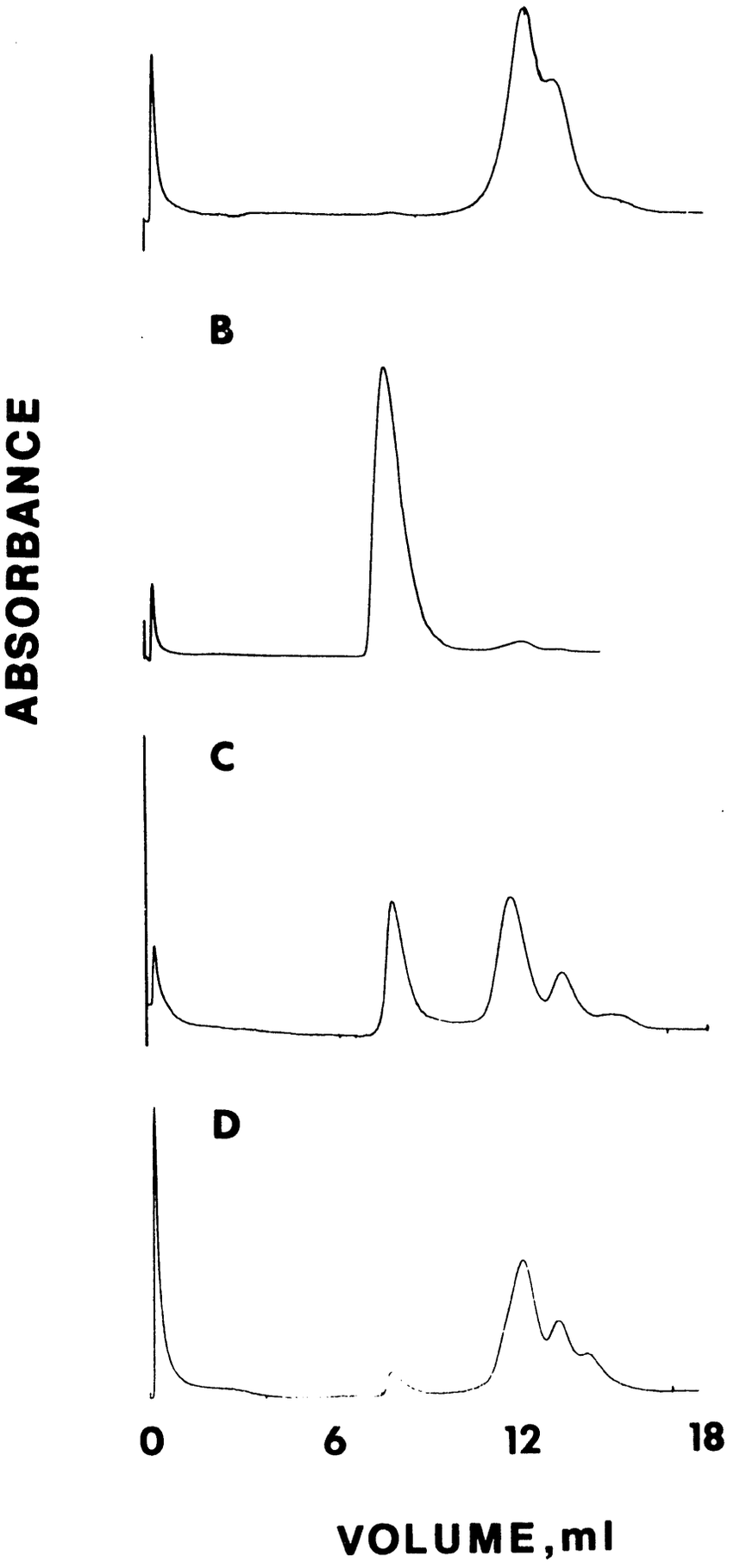
B
C
D
ABSORBANCE
0
6
12
18
VOLUME, ml

Figure 8.

Histograms of M_m values obtained by STEM mass measurements of unstained, freeze-dried specimens: (A), peak B and (B), peak C, obtained by gel filtration following dissociation in 4M urea at neutral pH (Figure 6, B and C). Typical STEM images are provided in Figure 2, C and D.

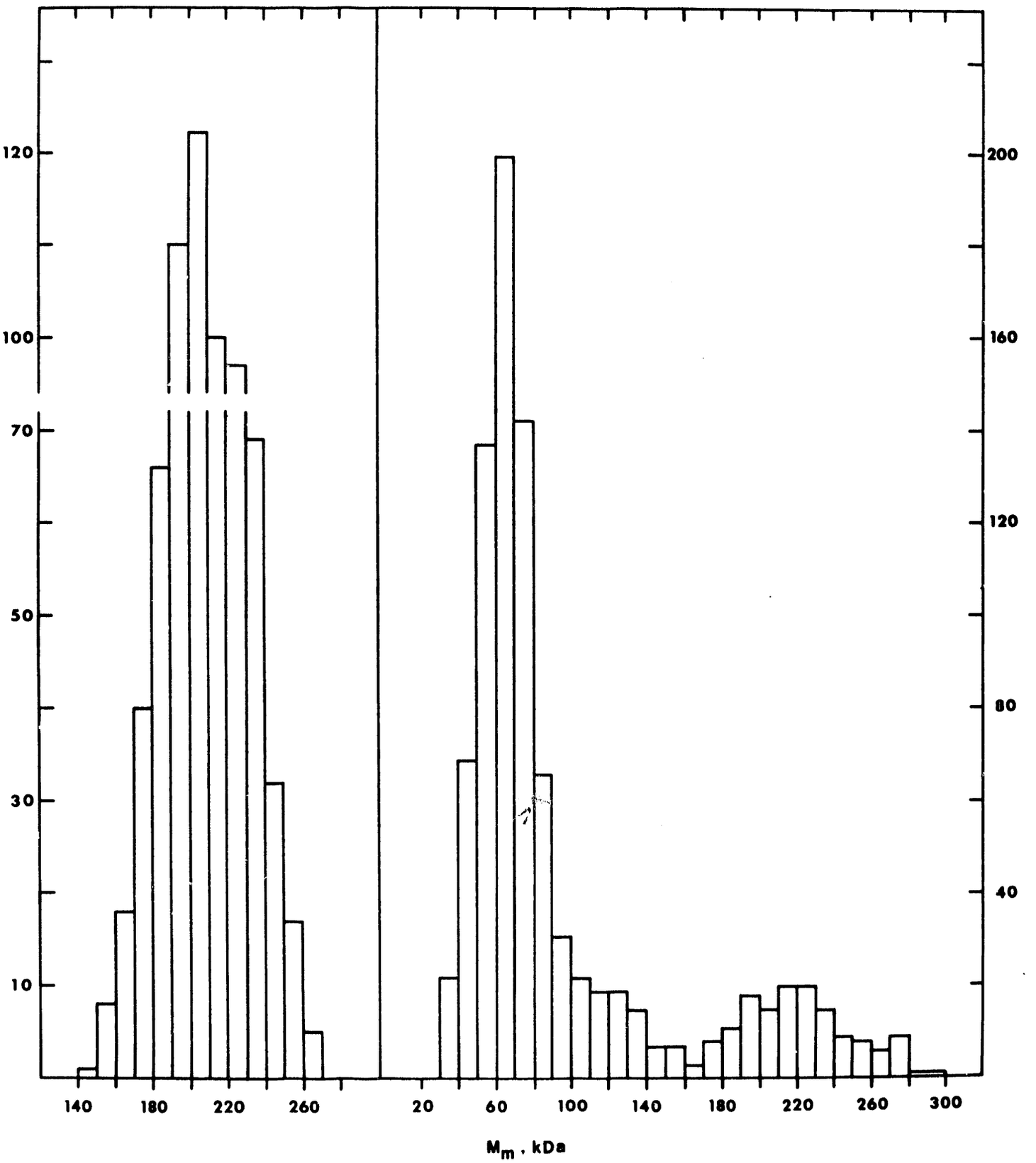
120
100
70
50
30
10
200
160
120
80
40
140
180
220
260
20
60
100
140
180
220
260
300
M_m , kDa

Figure 9.

Circular dichroism over 200-250 nm of (A), *Eudistylia* chlorocruorin and the products of its dissociation in 4M urea (Figure 6). (A), chlorocruorin, (B), peak B (dodecamer), (C), peak D (linker) and (D), peak C (tetramer).

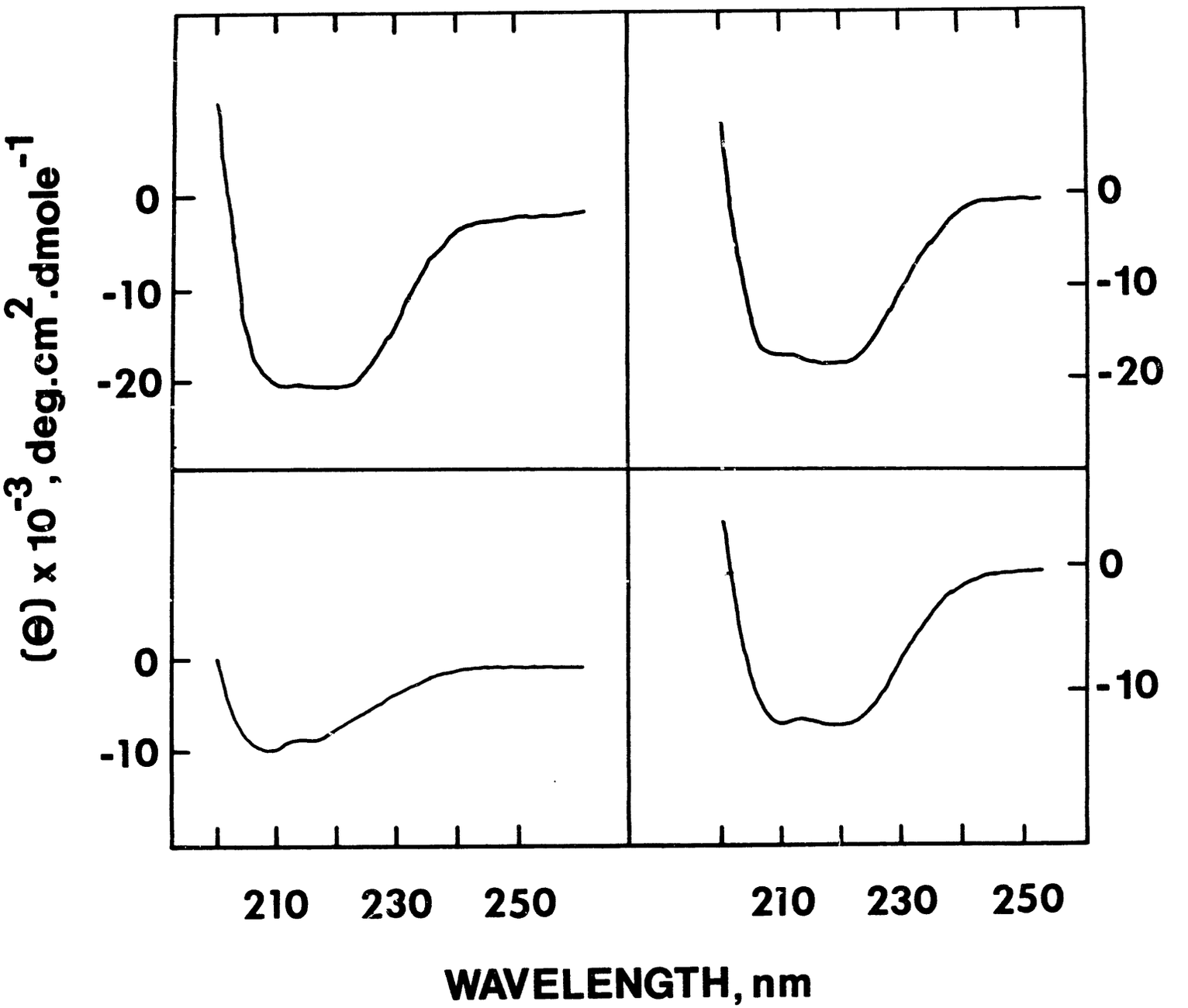
(Θ) x 10^-3, deg.cm^2.dmole^-1
0
-10
-20
0
-10
-20
0
-10
0
-10
210
230
250
210
230
250
WAVELENGTH, nm

Figure 10.

Effect of calcium on the dissociation of *Eudistylia* chlorocruorin in 4M urea at neutral pH. (Top) Percent dissociation, calculated from the absorbances of the peaks (A/A + B + C + D). (Bottom) Percent of total area represented by peaks B (dodecamer), C (tetramer) and D (linker) versus $CaCl_2$ concentration. Each point is an average of three data points obtained at 14.5-20.5, 44.5-50.5 and 238-244 hours subsequent to addition of urea with or without $CaCl_2$.

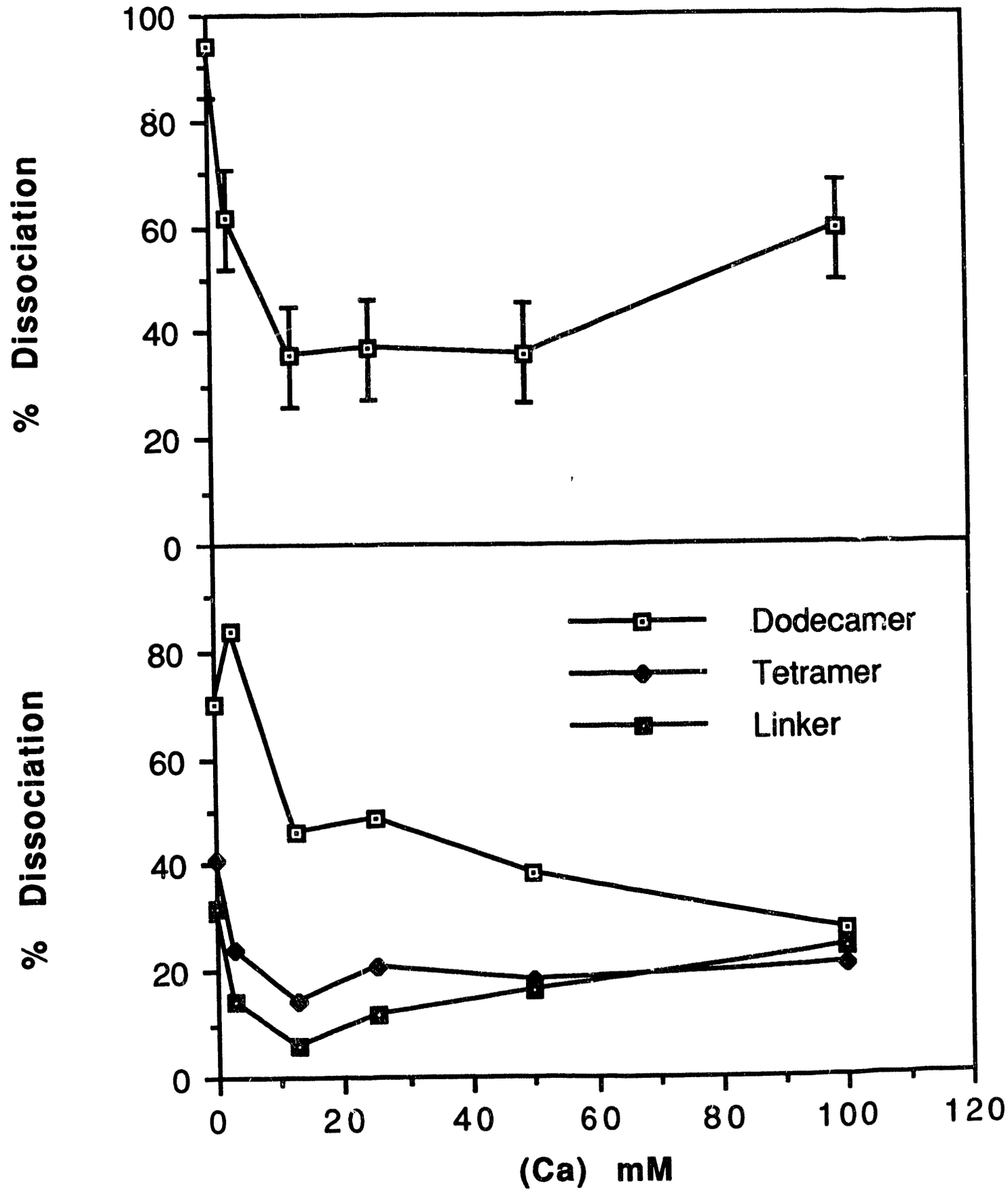
% Dissociation
100
80
60
40
20
0
% Dissociation
80
60
40
20
0
Dodecamer
Tetramer
Linker
0
20
40
60
80
100
120
(Ca) mM

Figure 11.

Effect of calcium on the reassociation of *Eudistylia* chlorocruorin subsequent to dissociation in 4M urea at neutral pH. (Top) Percent reassociation, calculated from peak absorbances (A/A + B + C + D). (Bottom) Percent of total area represented by peaks B (dodecamer), C (tetramer) and D (linker) versus $CaCl_2$ concentration. Each point is an average of three data points obtained at 0-6, 25-31 and 72-78 hours subsequent to removal of urea and addition of $CaCl_2$.

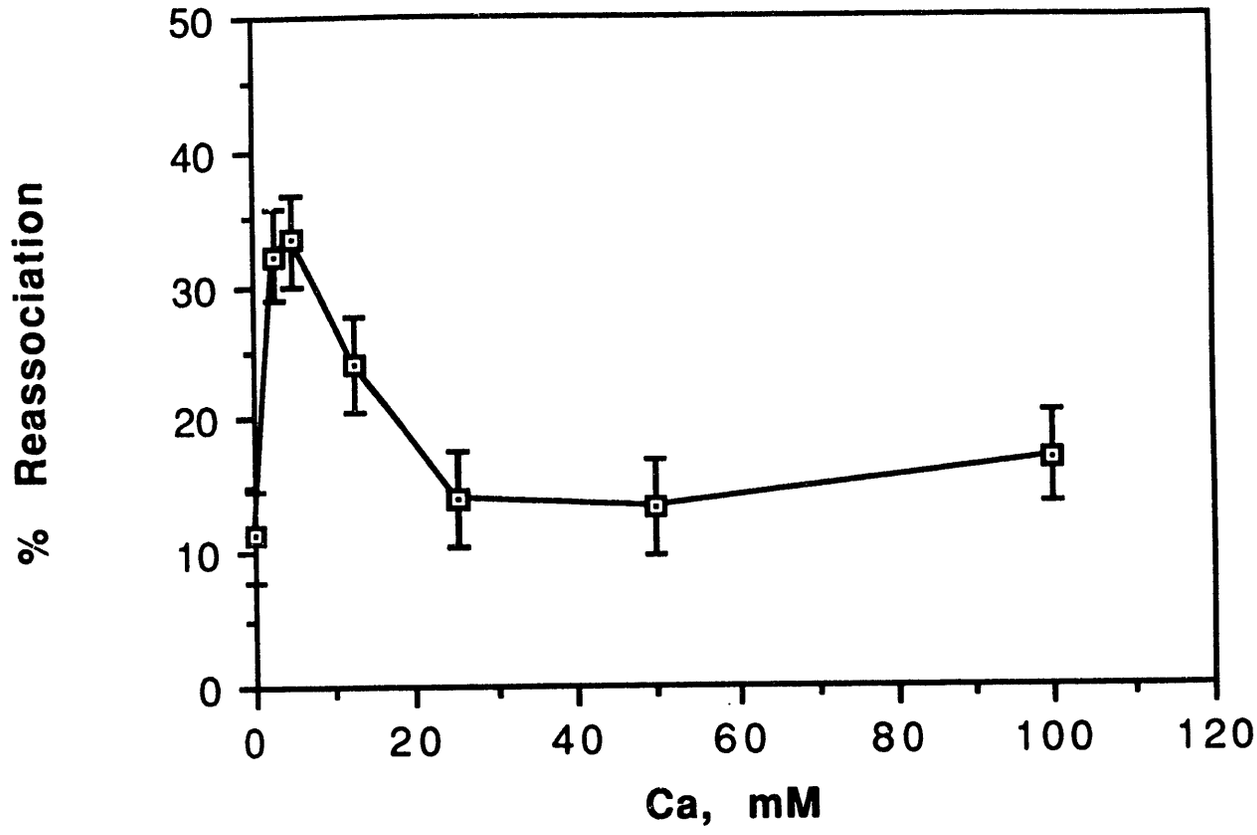
% Reassociation
50
40
30
20
10
0
0
20
40
60
80
100
120
Ca, mM

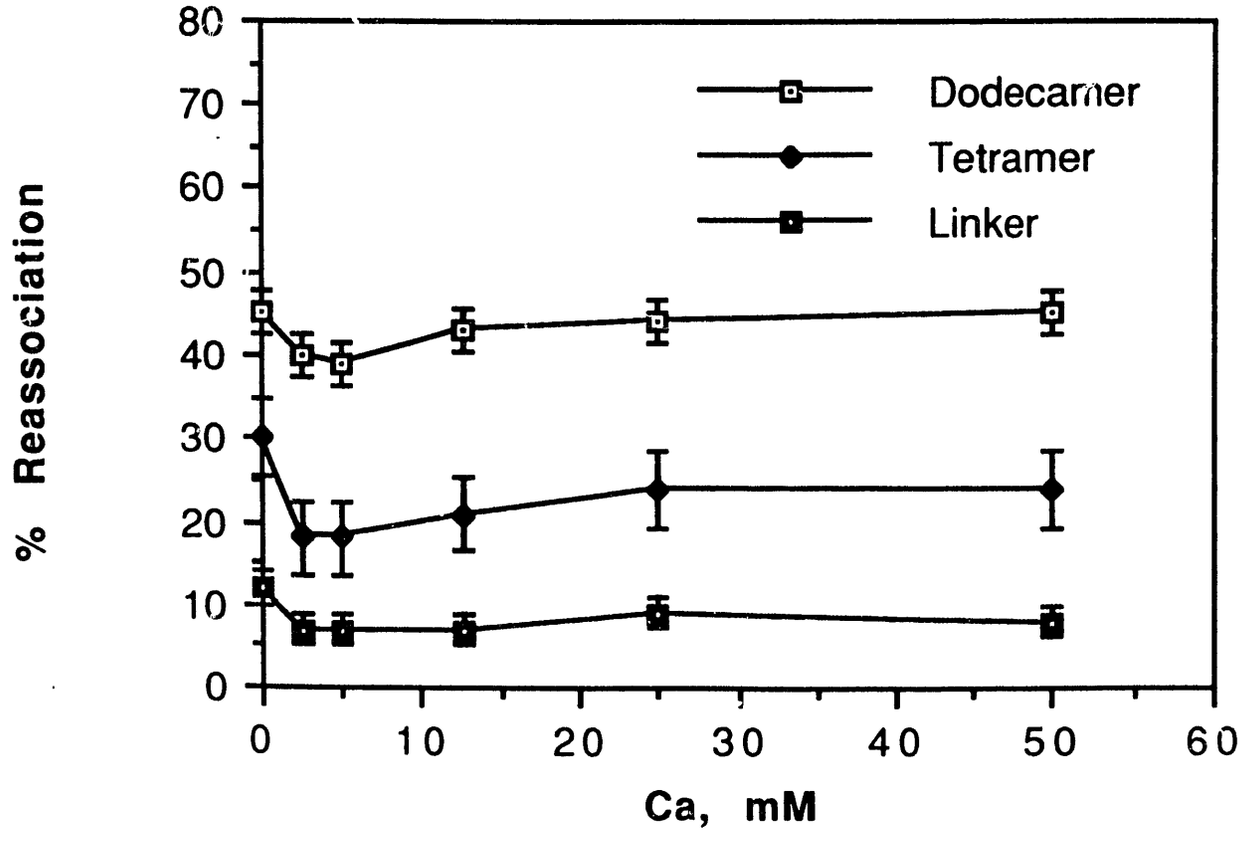
% Reassociation
80
70
60
50
40
30
20
10
0
0
10
20
30
40
50
60
Ca, mM
Dodecamer
Tetramer
Linker

Table 1. N-terminal sequences of *Eudistylia* chlorocruorin polypeptide chains.[1]

Subunit [2]	Peak [3]	Sequence
I	7	GQNEIKG LKVKLQWAQSFG
I	5a	GQNKMRR LKVKQQWSMAYG
II	4	GMKXXSMEDRKTVLADW
II	6	GSNEHDRQSIGDRQNLLSME
III	3	GATGGRGFSYALARIDGXNM
III	2	ALEGAVDXEX
III	1	ELSSEEVKRIDANGKKGDKL
Lumbricus [4]		ECLVTEG LKVKLQWASAFGH

1 Obtained by reversed phase chromatography of dehemed, reduced and carboxymethylated chlorocruorin.

2 Reduced SDS electrophoretic pattern (Figure 4C).

3 Numbered as in Figure 5. Peak 5 was rechromatographed using a 40 to 55% acetonitrile gradient to produce two peaks 5a and 5b. Peak 5b could not be sequenced by Edman chemistry suggesting a blocked N-terminus.

4 From Shishikura et al. (1986).

Table 2. Stoichiometry of *Eudistylia* chlorocruorin subunits from analyses of SDS-gel electrophoretic patterns.[5]

A. Densitometry	Linker [6]		Tetramer [6]	
	Percent	N_L	Percent	N_T
Unreduced Chl	48 ± 3	63 ± 4	52 ± 3	27 ± 2
Reduced Chl	27 ± 11	35 ± 12	73 ± 11	37 ± 6
Reduced, CM-Chl	25 ± 3	33 ± 3	75 ± 3	38 ± 2
B. Dye quantification				
Unreduced Chl	53 ± 6	70 ± 7	47 ± 6	24 ± 4
Reduced Chl	26 ± 9	34 ± 10	74 ± 9	38 ± 5

5 In the unreduced patterns the values provided for the linker (30 kDa) subunit represent the sum of subunits 1 and 2 (Figure 4). In the reduced patterns the values provided for the tetramer (65 kDa) subunit represent the sum of subunits I and II (Figure 4).

6 The number of copies were calculated using M_m of 3,480 kDa for the chlorocruorin, 26.5 kDa for the linker and 68 kDa for the tetramer (Table 5).

Table 3. Results of mass measurements [7]

Fraction\subunit [8]	Gel filtration [9] kDa	STEM kDa
Peak B (dodecamer)	196 ± 8 (4)	208 ± 23 (662)
Peak C (tetramer)	68 ± 10 (6)	65 ± 17 (635) [10]
		64 ± 15 (547) [11]
Peak D (linker)	39 ± 8 (6)	-
ca.10 nm particles [12]	-	218 ± 28 (159)

7 Mean ± SD (number of determinations\particles).

8 Obtained by dissociation at neutral pH in 4M urea.

9 FPLC on Superose S6 for band B and Superose S12 for peaks C and D.

10 Mean of values in 30-90 kDa range (Figure 2D).

11 Mean of values in 40-80 kDa range (Figure 2D).

12 The ca.10 nm particles in unstained, freeze-dried chlorocruorin (Figure 2A).

Table 4. Ratios of Soret and 280 nm band absorbances, ellipticities at 222 nm and estimated α-helical contents of chlorocruorin and its subunits.

Material	$A_{Soret}\backslash A_{280}$		$[\theta]_{222}$ [13]	Percent
	CO	CNmet		α-helix [14]
Chlorocruorin	1.46	1.16	-18,200	52
Peak B	1.63	1.24	-17,600	50
Peak C	1.44	1.19	-12,300	33
Peak D	0.43	0.62	-6,900	15

13 Mean residue ellipticity in deg.$cm^2.dmol^{-1}$.

14 Calculated from $f_h = -([\theta]_{222} + 2340)\backslash 30300$ (Chen et al., 1972).

Table 5. M_m of globin and linker chains of *Tylorrhynchus*, *Lumbricus* and *Lamellibrachia* hemoglobins, their Trp and Tyr concentration and percent mass contribution of Trp + Tyr + Met + Cys.

Globin	*Tylorrhynchus*[15]				*Lumbricus*[16]				Mean
	I	IIA	IIB	IIC	I	II	III	IV	
M_m, kDa	16.3	17.3	17.2	17.4	16.8	16.3	17.3	17.5	17.0
Trp	2	4	4	3	3	3	3	3	3.1
Tyr	4	3	1	1	1	3	1	3	2.1
WYMC%M_m / M_m	9.2	11.9	7.8	6.5	7.1	8.3	6.0	6.5	7.9

Linker	*Tylorrhynchus*[17]		*Lamellibrachia*[18]	Mean
	T1	T2	LV	
M_m, kDa	28.2	26.3	24.9	26.5
Trp	2	1	3	2
Tyr	5	5	7	5.7
WYMC%M_m	10.0	9.0	12.7	10.6

15 From Suzuki et al. (1982, 1985a, 1985b) and Suzuki and Gotoh (1986).

16 From Shishikura et al. (1987) and Fushitani et al. (1988).

17 From Suzuki et al. (1990a).

18 From Suzuki et al. (1990b).

Table 6. Calculation of subunit stoichiometry from the molar amino acid compositions of *Eudistylia* chlorocruorin and its tetramer and linker subunits.

Amino acid	Tetramer	Linker	Chlorocruorin
Asp	76.5	35.2	3,577
Glu	69.9	27.5	3,667
Ser	69.3	18.7	2,300
Gly	99.7	22.0	4,260
His	10.5	12.8	0,880
Arg	26.2	13.0	1,418
Thr	30.9	13.3	1,432
Ala	98.0	18.2	4,636
Pro	16.2	06.2	0,844
Val	37.9	12.4	1,777
Ile	22.4	09.0	1,185
Leu	36.7	15.4	1,925
Phe	21.0	07.7	1,374
Lys	13.1	11.8	1,008
M_m, kDa	61.88 [19]	24.115 [19]	3,083 [19,20]

No. Aa	No. eqs.	Eqs. with positive roots	N_T	N_L
14	91	57	33 ± 11	47 ± 26
		35 [21]	34 ± 4	43 ± 9
Least squares			36	38
8	28	26	35 ± 8	43 ± 17
		17 [21]	34 ± 3	44 ± 5
Least squares			36	38

19 Corrected for missing Trp, Tyr, Cys and Met.

20 Corrected for 150 heme groups (Section (j) in Results).

21 Average of positive roots within ± SD of the first mean.

Table 7. Calcium content of *Eudistylia* chlorocruorin [22]

Protein	Moles Ca\mole protein	Range	n
Native [23]	55 ± 16	36-81	14
Dissociated at pH 9.8	26	25-27	2
Dissociated in 4 M urea	13 ± 8	7-27	8
Mixed bed resin + Chelex 100	49		1
100 mM $CaCl_2$ [24]	51		1
500 mM $CaCl_2$ [24]	52		1

22 Chlorocruorin solutions were dialyzed prior to analysis against 1 mM KCl in order to avoid precipitation of the protein.

23 Prepared and kept at neutral pH in Tris.HCl buffer containing 1 mM EDTA.

24 Dialyzed extensively against $CaCl_2$ solution and then against 1 mM KCl.

Table 8. Molecular masses of *Eudistylia* and other chlorocruorins.

Molecule	$s_{20,w}$	M_m	Method [25]	Reference
Spirographis	57.5	2,800	LS, SD [26]	Antonini et al., 1962b
Spirographis	52.6	3,000	GF	Mezzasalma et al., 1983
Potamilla	56.3	2,900	SD [27]	Himmel and Squire, 1981
Eudistylia		3,480	STEM [28]	This work
Eudistylia	56.5	3,100	SEQ [29]	Terwilliger et al., 1975

25 LS = light scattering; SD = sedimentation and diffusion; SEQ = sedimentation equilibrium; GF = gel filtration.

26 Assuming v = 0.740.

27 Assuming v = 0.746.

28 Mass measurements of unstained, freeze-dried specimens.

29 Using v = 0.725, calculated from amino acid composition.

Table 9. Distribution of mass and heme in models of the quaternary structure of *Eudistylia* chlorocruorin.[30]

Subunit	M_m (kDa)	# Heme groups\ subunit	# Copies	Subunit Contribution # Heme Groups	Subunit Contribution Mass (kDa)
Model A [31,32]					
Linker	26.5	0.26	41	11	1,088
Tetramer	68	4	36	192	
Hexadecamer	272	16	16	192	3,264
Total				203	4,352
Calculated Fe content: 0.261 wt.%					
Total no. of polypeptide chains: (48 × 4) + 41 = 233					
Model B [32,33]					
Linker	26.5	0.26	30	8	808
Tetramer	68	4	36	144	
Dodecamer	204	12	12	144	2,424
Total				152	3,232
Calculated Fe content: 0.263 wt.%					
Total no. of polypeptide chains: (36 × 4) + 30 = 174					
Model C [33,34]					
Linker	26.5	0.26	39	10	1,039
Tetramer	68	4	36	144	
Dodecamer	204	12	12	144	2,424
Total				154	3,463
Calculated Fe content: 0.248 wt.%					
Total no. of polypeptide chains: (36 × 4) + 39 = 183					

30 Calculated using M_m of 17 kDa for globin and 26.5 kDa for linker subunits (Table 5).

31 Assuming 12 hexadecamers (12 × 16 = 192 globin chains).

32 Based on a globin to linker ratio of 0.75 : 0.25.

33 Assuming 12 dodecamers (12 × 12 globin chains).

34 Based on a globin to linker ratio of 0.7 : 0.3.

Cancer Cytogenetics

Introduction

In collaboration with Prof. Janet Rowley we are using our image processing capabilities to visualize fluorescence images of various nonradiolabeled DNA probes. This group is presently mapping the order of various genes and cosmid probes in human metaphase cells containing both a normal chromosome pattern or an abnormal pattern.

The abnormalities studied include gains or losses of whole chromosomes as well as various structural rearrangements including translocations and deletions in cells from patients with leukemia. DNA probes are being used to map their location relative to the chromosome breakpoints and ultimately to identify the genes that are affected by these chromosome abnormalities. At the present time, a Zeiss fluorescence microscope fitted with the appropriate excitation and emission filters is being used. In addition, this group has confocal fluorescence microscopes equipped with sophisticated fluorescence signal detectors and the data are processed and displayed on computer enhanced digital screens. These laboratories can integrate the data obtained from analyzing a single metaphase cell using several different fluorochromes or different probe detection systems. The location along the chromosome of these various signals can be displayed as a single image which allows the investigator to determine the position of the various probes along the chromosome. At the current facility at the UofC, separate photographs are taken and their sequence has to be compared visually to try to construct the most likely position of the probes relative to one another. Moreover, reproduction of these photographs is very difficult because of the problem of enhancing the intensity of the specific signal relative to the background.

We are digitizing and processing these images using our recently developed image processing system (1) and an example is shown in Figure 1. Here we use the superior processing power of the IBM RS-6000 530 workstation to enhance a very low contrast image of labeled human metaphase chromosomes.

For the future we intend to connect the output of these microscopes directly to the high-speed network via the node that is in place in the Franklin McLean Institute. We can then provide a more rapid turnover for this research, and streamline the data analysis significantly.

References

1. Development of an image processing system on a second generation RISC workstation. M.J. Ryan and O.H. Kapp. *SPIE Proceedings*, **1396**, 335-339 (1991).

Figure 1.

Image processing of human metaphase chromosomes.

Algorithm Development for Alignment of Proteins and Nucleic Acids.

Introduction

We have begun a program to develop new algorithms for the alignment of protein amino acids and DNA and RNA base sequences. This work sprang from a perceived inflexibility in the canned programs that are available from the PIR (Protein Identification Resource, National Biomedical Research Foundation). One such program is the algorithm called "ALIGN". As is typical of these programs, this algorithm is written in FORTRAN and is used uncritically by most individuals making use of the growing protein and DNA database. ALIGN is based on the well-known Needleman and Wunsch algorithm (1) and relies on a single scoring matrix created by Dayhoff (2). In the past few years various attempts have been made to refine this algorithm using a variety of techniques and by generating more sophisticated scoring matrices (3-17). A particularly important new approach to this work is the efforts that have been put forth to use the crystal structure data of homologous structures to perform the alignment in three dimensions. Thus, the matter of steric constraints is considered in addition to reference to tables of substitution probabilities based on somewhat circular evolutionary arguments (10).

We have rewritten ALIGN in the interpreted language APL. This language allows us a much faster turn-over time in algorithm development and provides us with a more immediate ability to try "what-if" experiments without having to recompile the source code. In addition, we can now exploit the advanced graphics capabilites of our high-performance IBM RISC workstations (530 and 730) to compare space-filled models of structures (whose crystal structure is known) to the primary sequences of unknown structures. The aim is to predict the three-dimensional morphology of an unknown structure from consideration of its primary sequence and by comparison with the primary sequence and crystal structure of an homologous structure.

The ease with which various experiments can be carried out is demonstrated by the following example. It is known that the 'linker' proteins of the invertebrate extracellular hemoglobins are unusual in being larger (31-37 kDa) than the basic myoglobin-sized building block of which most other invertebrate hemoglobins and all vertebrate hemoglobins are comprised. It is attractive to speculate that this unusual size is caused by an anamolous arrangement of exons. Whereas in the usual myoglobin subunit we observe three gene products, (exon1, exon2, exon3) connected together covalently to generate the native functioning protein, in the linker subunit, a possible arrangement may be exon2-exon3-exon1-exon2.

As a test we match the sequence of sperm whale myoglobin against a linker from *Lamellibrachia* hemoglobin using the Needleman algorithm with the gap penalty set to 8. The "linker" sequence is:

AAVQPLSVSDAMGARVDAQAWRVDRLTKQFQAISDAADTSIGAAKSGGDIARHMLNSHLDD

HWCPSKYH,
PQCMSNMAFCDGVNDCKNHFDEDENRCVVPVTANSTWIGYPAYDHCTQRRPYEMVISITSAP
S,
VHQPLKVQVDLFSKKGGLKQSASLHGDAVYCKGSQRLIVAPPEDDRLEIIGQFDGVSNDRFK
G,
MSGDKCAEFRFFKQ

The sequence of sperm whale myglobin is:

VLSEGEWQLVLHVWAKVEADVAGHGQDILI-RLFKSHPETLEKFDRFKHLKTEAEMKASEDL
KKHGVTVL,
ILKKKGHHEAELKPLAQSHATKHKIPIKYLE-FISEAIIHVLHSRHPGDFGADAQGAMNKALEL,
AAKYKELGYQG

The three exons are delineated by the dashes. The results of the alignment are shown in Figure 1. Clearly, for reasons of difference in size alone, this is not a particularly good alignment.

In Figure 2 we create a hypothetical sequence made up of the myoglobin exons in the order 2-3-1-2. In this particular program the names of the exons are "exon1", "exon2" and "exon3". The required APL2 expression to effect this alignment trial requires the simple imput "exon2,exon3,exon1,exon2". In APL the commas indicate that the respective parts are to be connected linearly in the order given. The results of this alignment (Figure 2) are clearly of more interest that those shown in Figure 1.

Figure 3 shows a 3D spaced filled model of *Glycera* hemoglobin, obtained from Prof. Warren Love at Johns Hopkins. The image is displayed on our IBM model 530 high-resolution monitor and can be manipulated interactively using subroutines from the GL library. We are presently integrating the two and three dimensional analysis, all written in APL, to create a highly interactive tool for alignment and structural analysis.

References

1. Needleman, S.B. & Wunsch, C.B. (1970) *J. Mol. Biol.* **48**, 443-453.

2. Dayhoff, R.M. Schwartz, R.M. and Orcutt, B.C. (1978). *Atlas of Protein Sequence and Structure.* Silver Spring, Maryland: National Biomedical Research Foundation.

3. Myers, E.W. and Miller, W. (1989). *Bulletin of Mathematical Biology* **51**, 5-37.

4. Landau, G.M. and Vishkin U. (19[illegible] *Jour. of Algorithms* **10**, 157-169.

5. Barton, G.J. and Sternberg, J.E. (1987) *J. Mol. Biol.* **198**, 327-337.

6. Devereux J.R. Doctoral Thesis, (1988) University of Wisconsin-Madison.

7. Barton, G.J. and Sternberg, J.E. (1988) *J. Mol. Graphics* **6**, 190-198.

8. Ponder, J.W. and Richards, F.M. (1987) *J. Mol. Biol* **193**, 775-791.

9. Bryant, S.H. (1989) *Proteins* **5**, 233-247.

10. Risler, J.L., Delorme, M.O., Delacroix, H. and Henaut, A. (1988) *J. Mol. Biol.* **204**, 1019-1029.

11. Lipman, D.J., Altschul, S.F. and Kececioglu, J.D. (1989) *Proc. Natl. Acad. Sci.* **86**, 4412-4415.

12. Altschul, S.F., Carroll, R.J. and Lipman, D.J. (1989) *J. Mol. Biol.* **207**, 647-653.

13. Islam, S.A. and Sternberg, M.J.E. (1989) *Protein Engineering* **2**, 431-442.

14. Pastore, A., Lesk, A.M., Bolognesi, M. nad Onesti, S. (1988) *Proteins* **4**, 240-250.

15. Gribskov, M., McLachlan, A.D. and Eisenberg, D. (1987) *Proc. Natl. Acad. Sci.* **84**, 4355-4358.

16. Blundell, T.L., Sibanda, B.L., Sternberg, M.J.E. and Thornton, J.M. (1987) *Nature* **326**, 347-352.

17. Bashford, D., Chothia, C. and Lesk, A.M. (1987) *J. Mol. Biol.* **196**, 199-216.

Figure 1.

Alignment of the sequence of sperm whale myoglobin versus the sequence of a "linker" subunit from *Lamellibracia* hemoglobin

**PIECE 3 224 CHARACTER

```
          10        20        30        40        50        60        70
VLSEGEW----------------------------------------------------QLVLHVWAKVEADVAGHG
AAVQPLSVSDAMGARVDAQAWRVDRLTKQFQAISDAADTSIGAAKSGGDIARHMLNSHLDDHWCPSKYHRCGNS

          80        90       100       110       120       130       140
QDILIRLFKSHPETLEKFDRFKHLKTEAEMKASEDLKKHGVTVLTALGAILKKKGHHEAELKPLAQSH
PQCMSNMAFCDGVNDCKNHFDEDENRCVVPVTANSTWIGYPAYDHCTQRRPYEMVISITSAPSDIVYK

          150       160       170       180       190       200       210
ATKHKIPIKYLEFISEAIIHVLHSRHPGDFGADAQGAMNKALELFRKDIAAKYKELGYQG--------
VHQPLKVQVDLFSKKGGLKQSASLHGDAVYCKGSQRLIVAPPEDDRLEIIGQFDGVSNDRFKGYIVRE

          220
----------
MSGDKCAEFRFFKQ
```

**NAMEINDEX 1 60 MIXED

Figure 2.

Alignment of the sequence of the 3 exons of sperm whale myoglobin in the order 2-3-1-2 versus a "linker" subunit from *Lamellibracia* hemoglobin

**PIECE 3 152 CHARACTER

```
         10        20        30        40        50        60        70
RLFKSHPETLEKFDRFKHLKTEAEMKASEDLKKHGVTVLTALGAILKKKGHHEAELKPLAQSHATKHKIPIKYL
AAVQPLSVSDAMGAR-----VDAQAWRVDRLTKQFQAISDAADTSIGAAKSGGDIARHMLNSHLDDHWCPSKYH

            80        90       100       110       120       130       140
      EFISEAIIHVLHSRHPGDFGADAQGAMNKALELFRKDIAAKYKELGYQGVLSEGEWQLVLHVWAKVEA
      RCGNSPQCMSNMAFCDGVNDCKNHFDEDENRCVVPVTANSTWIGYPAYDHCTQRRPYEMVISITSAPS

           150
      DVAGHGQDIL
      DIVYKVHQPL
```

**NAΔMEINDEX 1 67 MIXED

Figure 3.

Space-filled model of the hemoglobin of *Glycera* from the crystal structure obtained by Prof. Warner Love. The heme moiety is in the lower left backside of the structure.

III. 0.5Å STEM

Progress on the Sub-Angstrom STEM: July 1990 - June 1991

Our two goals for this year were to produce a steady, quiet electron beam and to examine the electron-optical properties of the sub-angstrom STEM. Unfortunately, financial constraints required that we employ only one person to accomplish these goals. Dr. Shengyang Ruan, our electronics engineer, worked alone on this project, and---in spite of the strained financial situation---has realized these two goals.

Summary of Activitiy

1. This year, we have improved the system vacuum by reducing the original pressure of 1×10^{-9} torr to 3×10^{-11} torr. To accomplish this, we modified the design of the tip carrier and reduced its surface area; we attached two getters as associate absorbing pumps; and we eliminated three tiny leaks on the electron source chamber.

2. In completing his microscope control computer program, Dr. Ruan has added a feature that will trim and temper the tip with precision in the high vacuum chamber. This program uses a multi-looped trial cycle to determine the best flash level. Each time the tip is flashed, the flash level is corrected using information gleaned from the last flash. During each cycle, the computer gauges the amount of gas that escapes during the flashing, monitors the tip running process, chooses the most advantageous moment to re-flash and initiates a new cycle of tip tempering. The use of this program enables us to maintain workable tips at the best conditions for electron emission, thus saving us the great time, energy and material necessary to pursue the same aim manually.

3. The modification in the tip carrier design and the completion of Dr. Ruan's computer program has enabled us to both obtain a steady, quiet tip emission current persisting for several hours after each flash, and locate an electron beam at the top of the accelerator and at the first condenser lens.

4. The tip carrier driving system in the vacuum chamber is now completely operational. Before our repairs, it would consistently jam; now it may be successfully used for tip alignment.

5. We have tested the focusing effect of the condenser lens and have found it to be satisfactory.

In the next year, we will trace the beam to the top of the microscope. In addition, we will reorganize and test the image acquisition system and all electronic units together with the electron optical components (i.e., lenses, coils and the two sextupoles).

Improving the Pressure of the High Vacuum Chamber

The problem with the vacuum chamber has plagued us for some years. This STEM has a very complex structure, and every valve, fringe, gasket, feed-through insulator, bellow, or welded seam may leak. The surfaces of all components in the high vacuum chamber and the inner wall of the cavity may release gas, but detecting such leaks and pumping the system to its proper pressure are extreme time- and energy-consuming tasks. For instance, system inspection, the search for leaks, part replacements and

design modifications required that we open the chamber seven times this past year, each instance taking three to four-and-a-half weeks to complete the necessary repairs and restore the pressure.

Even a clean tip in a constant, low-pressure environment will absorb surrounding gases and form a gas atom layer on its surface. This layer reduces the emission efficiency of the tip, causes its decay, and eventually prohibits the production of a tip current. As the tip is heated, the gas layer becomes increasingly thick, and a microdischarge arc forms, causing the tip current to abruptly increase and to become widely variant and noisy. The arc bombardment on the tip surface will ruin the tip as it becomes rough, blunt and incapable of emission. However, if the tip is flashed properly, at the best current and most appropriate moment, its clean surface will be restored and the current will remain steady.

The duration of a stable emission current is dependent upon the pressure of the gas surrounding the tip. The most advantageous pressure achieved before the end of last year was 1×10^{-9} torr. In that environment, the tip had to be flashed frequently, the flash level necessarily increasing at each flash to clean and restore the tip's smooth surface. As this flash level increased, the tip surface would eventually melt and become blunt. Thus we experienced much difficulty in finding a tip with sufficient emission stability and duration for use with a microscope.

Since so many components leaked, it was extremely difficult to lower the vacuum chamber's pressure to below 1×10^{-9} torr. We disassembled and reassembled many of the microscope components over and over again in search of leakages. We finally found three leaks on the back and top sides of the vacuum chamber. One was due to a faulty valve, and the others were attributed to problems with the fringe gaskets.

We acquired additional improvements in pressure by modifying the tip carrier design. The original carousel carried eight tips and was rotated by a driving system for tip changing. Unfortunately, this carousel was complex in structure and provided numerous surfaces from which gas could leak. We replaced this carousel with a much simpler design carrying only one tip, and have consequently lowered the pressure in the vacuum chamber. We also installed two getters to absorb the residual gases at the final stage, when the pressure cannot be further reduced by any of the other methods.

These modifications have helped us to achieve an excellent record. After cleaning every inner component of the tip chamber, baking and pumping for one week, and firing the getters at the final stage, we have achieved a pressure inside the vacuum chamber as low as 3×10^{-11} torr. The equilibrium pressure returns to 1×10^{-10} torr a few days later, but is still satisfactory for our use.

Program for Trimming and Flashing the Tip

As mentioned above, a tip must be flashed at a particular moment during normal operation of the STEM. A new tip fashioned through chemical etching must also be flashed to develop a tip semispherical in shape with a clean surface. Selection of a flash level for these functions is quite critical: flashing at too high of a level will degenerate and perhaps even ruin a tip, but flashing at too low of a level will not result in the required outcome. In addition, since no method exists to assure that every tip is identical in size and shape (complicated by the fact that the head of the tip is very tiny, only about 0.2 micron), the flash level for each must be individually chosen.

Ordinarily, microscope operators use a "trial" method to flash the tip at the proper level. The trials begin at an absolutely safe level and are gradually advanced to a high flash level. The emission light color may ordinarily be seen through the window on the vacuum chamber so that the tip's flashing temperature may be roughly determined. However, the exact measurements for each flash may be obtained only by determining the transient pressure change and the function of tip emission current vs. time after the flash and equilibrium of pressure have been restored---a time- and energy-consuming task.

Since our new electron microscope does not have a window in its vacuum chamber wall, we are not able to use even the imprecise method of judging temperature by the color of the emission light while flashing. The computer program written by Dr. Ruan not only helps us to gauge the temperature of the tip, but also provides a method to precisely condition the tip without resorting to manual measurements and calculations. This program enables a PC-AT to control all devices for status measurement and operation of the electron source on the high-voltage terminal. The following basic functions and procedures for tip flashing and trimming have been included in the computer program.

1. The anode may be grounded and the extracting voltage (V1) power supply discharged. This very important subroutine protects the tip from being damaged by strong pulses of tip emission current. As the microscope is turned on or the tip flashed, these pulses of tip emission current may result in a V1 surge or in the tip appearing incandescent. This protective subroutine is automatically performed any time a pulse of this nature may occur.

2. The tip emission current, ion pump current, extracting voltage, tip carrier position and battery group voltage, etc. may be measured. All signals to be measured are converted to digital data by a D-A converter and are then sent to the computer quiet bus by way of an opto-coupler assembly to isolate the high voltage. Some weak signals, such as the tip or pump current, must be amplified by a multi-channel electrometer before the A-D converter may receive them. The V1 regular board is equipped with another electrometer to measure high extracting voltage. To amplify the weak input signal to a desired and accurate level, the program automatically directs the electrometer adjusting range and measurement speed.

3. All control and measurement functions are directed through a timing device to ensure proper timing and maximum efficiency. A real-time clock is displayed on the screen for the duration of the experiment. In addition, information regarding times and dates are typed on the record chart and written to the computer disk along with other experimental flash parameters for future reference.

4. The functions for relay group control and those for grounding the anode and discharging the V1 power supply, measuring experimental parameters and timing procedures all work together to monitor the electron source status and investigate the effect of flash. Together, these routines produce high-resolution graphs of: the transient pressure change measured by the pump current and the amount of gas released while flashing, curves of the tip current vs. V1, and emission current vs. time, and the change in the extracting voltage vs. time when the constant current mode is set.

5. The original tip flash data may be recalled from the computer hard disk, and new data is saved on the hard disk. The tip flash data is recorded each time the program starts and a new flash is performed.

6. The data may be sent to a printer and/or be processed in chart or graph form. This function may be performed at the end of one test cycle, and a new cycle will automatically begin.

7. The flashing of the tip is one of the principal functions controlled by this computer program. At the beginning of the procedure, the system is inspected for tip safety: the program confirms that the anode has been grounded, that the extracting voltage has been lowered to zero (or to a given level), that the carousel is set to the correct position and that the system vacuum pressure is low enough for the tip to be safely flashed. Once these details have been confirmed, the computer will initiate the flash by driving a series of electronic and relay switches and a comparator to charge a large capacitor. This capacitor will then be discharged to produce a transient current in the tip filament. Simultaneously, a transient pressure change and information regarding gas release are collected and displayed on a graph. The pressure will be monitored for about 30 seconds until it returns to its normal state.

   The program will also check for abnormalities in the flashing procedure (for example, it will make sure that the charging process is normal and that the tip filament is still intact, etc.). If the flash was successful, relevant data (including the number of times the tip has been flashed, the flash level, the date and the time) will be recorded on the computer hard disk in a tip record file.

   It is very important in evaluating the effectiveness of the flash to determine the transient pressure change and the amount of gas released during the procedure. A peak pressure within the order of a micro torr and the area under the curve within the range of 10^{-8} torr.min. would be considered adequate.

8. In the investigation of flash effectiveness, the program will also direct the V1 power supply to gradually increase its output to the anode and will draw a graph of the tip current in relation to the extracting voltage. The noise level, the position of the intersection at which the curve rises from the horizontal axis and the slope of the curve are all dependent upon the applied flash level. A good flash level should achieve a curve near the intersection, a sharp slope and little noise. If the flash level is too low, the noise will not be eliminated, but if it is too high, the intersection will be un-reversibly pushed further and the gradient of the curve will be reduced, thus lowering the efficiency of emission and the lifetime of the tip.

9. The last and most important step in investigating flash effectiveness is to actually flash the tip and then to gauge how long the flashed tip is able to perform its function. As the tip is being flashed, the program monitors the noise level and the curve of the emission current vs. time is drawn. If the sum of the jumping altitude over 10 percent reaches a point higher than 0.8, the computer will discontinue the function and disconnect the anode power immediately. The computer determines a new level for the next flash by analyzing the measured flash effects.

   If a slow shift in amplitude of more than 100 percent is discovered, the computer will respond in the same manner.

10. The program includes a constant tip current mode in which the computer adjusts the extracting voltage to its advantage. This mode is useful for seeking a beam above the accelerator and the first condenser lens, as will be elaborated later.

11. The tip may be aligned either automatically or manually. The manual mode permits the user to drive the motors by pressing the arrow keys. The automatic scan mode drives the tip carrier in a set pattern. To protect the stepping motors, the computer will disconnect the power supply for the motors if the mechanical system has approached its travel bounds or is becoming jammed.

12. The computer will verify each step of operation. If there is any difference between the data sent to a control device and that read back from it, all operation will cease and the address of the faulty register will be displayed so that the problem can be quickly remedied.

13. The program's signal system still displays numerous warning signals and error messages, such as "bad vacuum," "no power to pump," "slow charge . . .," "filament broken," "must charge batteries," "reach boundary," and "jam" in addition to the signals that report register errors. Sound signals are given in some special cases. A grinding sound indicates that the motor is running normally. The frequency of the sound will change with changes in direction or with a change in the motors used for tip carrier driving. A series of three beeps indicates that the mechanical travel boundary has been reached. An alarm will sound to warn against motor jamming.

    Use of this program has helped us to acquire several satisfactory tips through 20 to 30 hours of conditioning, and 200 to 300 flashes. The tip will run quietly for eight to twenty hours after a flash (see Figure 1).

Tip Alignment System

We have experienced numerous problems with the tip alignment system. Although we modified the motor driving circuits to enable the user to preset the traveling range and monitor the position of the tip carrier, the system was still plagued by mechanical difficulties. Some moving parts produced too much friction, but we could not use a lubricant to alleviate this problem without jeopardizing the high vacuum environment. After repairing the system several times to no avail, we finally removed the carousel driving parts as they were not well-designed for our purposes.

At first the condition seemed to be alleviated; but then the problems recurred. After the system "died," we realized that the lubricant applied to the motor gear box was solidifying when the system was baked (baking is a necessary procedure in establishing a high-vacuum state; to obtain a high-vacuum environment, the system must be baked for several days while the chamber is pumped). We removed and cleaned all of the components in the gear boxes, and then applied a moly-base, high-temperature lubricant to the motor. The reassembled system now works efficiently and smoothly. It has undergone extensive baking twice now, and is still in good working order.

Locating the Beam and Testing the First Condenser Lens

To obtain an electron beam and to test the electron gun, the accelerator and the first condenser lens, we installed a YAG converter and a photomultiplier at the top of the first condenser lens. A post-amplifier with a filter was installed in order to produce a clearer signal which could be recorded in chart format; and the system was also equipped with an alarm that will sound when a beam is found. We used constant current- and tip auto-scan modes to search for the beam. After a few hours of scanning, with the acceleration voltage at 15 kV and tip current at 150 nA, we have for the first time found a very sharp peak in the recorded spectrum. The finer scanning and an estimation of the peak width indicates that the peak is attributable to the electron beam.

To get the beam spot image and to test the focusing, we increased the acceleration voltage to 25 kV and the tip current to 500 nA. The spot of the beam could even be seen by the naked eye.

We employed a CCD camera with display to help us to more precisely align the tip. The shape of the beam spot may be observed on the monitor as we use a keyboard to adjust the tip carrier's position.

A test of the first condenser lens indicated that focusing was satisfactory. The original spot was 2 mm in diameter and was focused to a much smaller size (difficult to measure) by applying 140 mA of lens current. Figure 2 depicts the focused beam spot obtained with the first condenser lens.

Figure 1.

Computer display showing stable field emission.

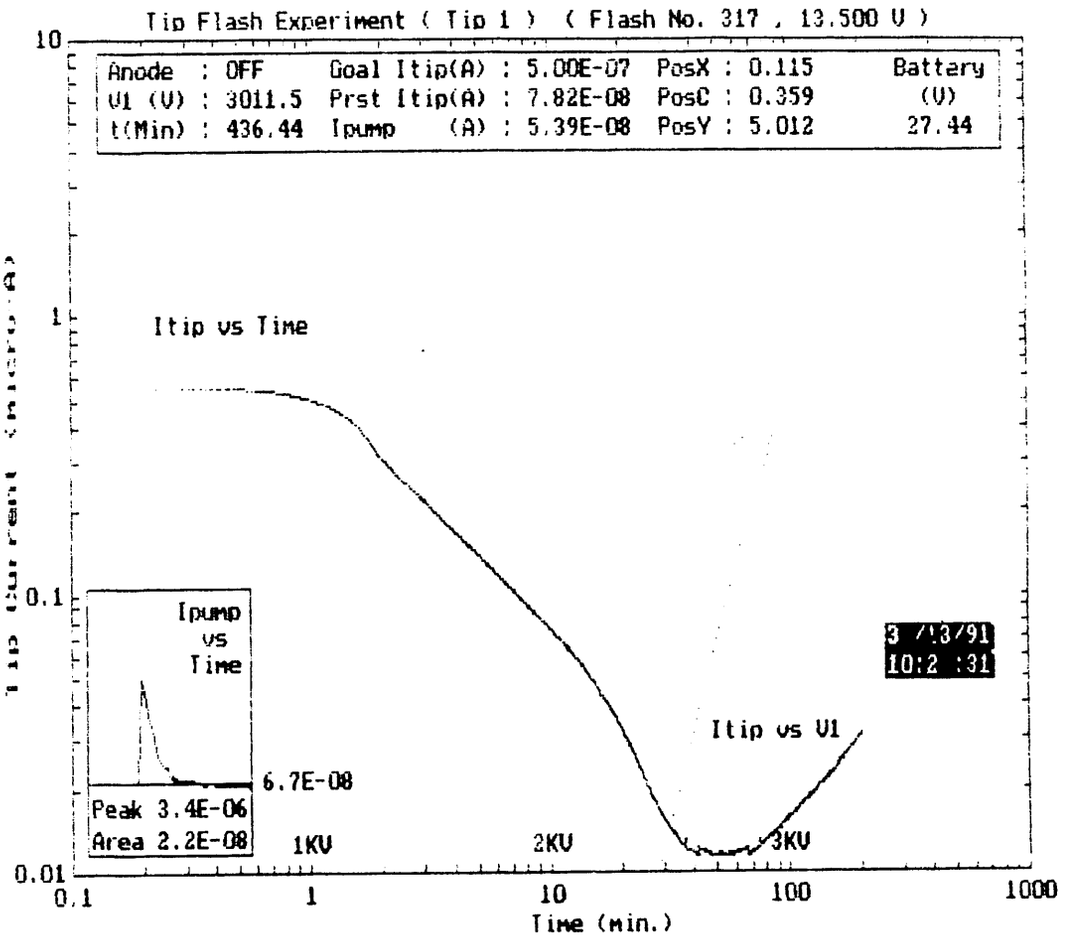
Tip Flash Experiment (Tip 1) (Flash No. 317 , 13.500 V)
Anode : OFF
V1 (V) : 3011.5
t(Min) : 436.44
Goal Itip(A) : 5.00E-07
Prst Itip(A) : 7.82E-08
Ipump (A) : 5.39E-08
PosX : 0.115
PosC : 0.359
PosY : 5.012
Battery (V) 27.44
Itip vs Time
Ipump vs Time
6.7E-08
Peak 3.4E-06
Area 2.2E-08
1KV
2KV
3KV
Itip vs V1
3 /13/91
10:2 :31
10
1
0.1
0.01
0.1
1
10
100
1000
Time (min.)

Figure 2.

CCD display of focused beam spot obtained with first condenser lens.

IV. LABORATORY COMPUTER SYSTEMS

Development of an image processing system on a second generation RISC workstation

Introduction

The new generation of RISC workstations are characterized by improved graphics capabilties, enhanced CPU floating-point performance, and larger available random access memory (RAM). Numerically intensive calculations, once limited to execution on mainframes, can now be routinely performed on in-lab personal workstations.

In our lab images obtained from the microscopes are stored on the 5 Gbyte disk sub-system of our in-lab IBM 4381 mainframe in 512 x 512 pixel format with 8 bit precision. A typical session at the microscope may generate several hundred images. Many of the image processing tasks are performed on data sets numbering in the thousands of images. Thus there is a need for both image processing capability and also exceptional CPU floating-point performance. In the past we have relied on the 0.96 MFLOPS (LINPACK) performance of the mainframe but have found that for tasks involving large amounts of data we needed more speed.

A wide range of standard image processing techniques are required due to the interdisciplinary nature of this laboratory and the extensive range of specimen types observed in the STEM. Examples would include the observation of single atoms and small cluster growth, intercalated graphite and biological specimens such as high density lipoproteins, ribosomes, and proteins. Algorithms making use of the high performance of the CPU include simulations (e.g. diffusion-limited aggregation (DLA)), three-diemnsional reconstruction techniques and movie sequences. Particular examples include the 3D reconstruction of proteins from STEM images and the demonstration of single atom motion by movie sequence display of successive atom images generated on the microscope.

Hardware

We have acquired an RISC 6000-530 workstation under agreement with IBM. This is a multi-user, multi-tasking UNIX computer with a 25 MHz (IBM SGR 2564 processor), 10.9 MFLOPS (100 x 100 double-precision LINPACK) speed, and 48 Mbytes of RAM. It is configured with one Gbyte of disk and has access to an additional 5 Gbytes via connection to the lab 4381 disk sub-system. It has a 1280 x 1024 pixel IBM 6091 19 inch 60 Hz non-interlaced display. With this configuration this workstation provides exceptional performance for both numerically intensive and memory intensive applications.

The workstation was equipped with IBM's high-performance 24-bit 3D color graphics processor. This is a mid-range graphics adapter which supports 24-bit pixels, 24-bit true color, overlay planes, window

control planes, arbitrarily-shaped windows, multiple, colored, local, and infinite lights, diffuse ambient, and specular (Phong) lighting models, flat and smooth (Gouraud) shading, 8- or 12-bit dithered RGB shading, anti-aliased lines, 6-axis clipping, pan and zoom of images, programmable cursor and integer, and 32-bit floating-point coordinate systems.

This processor is capable of executing four instructions per clock cycle: one branch operation, one condition-register operation, one fixed-point operation, and one floating-point operation. There are 184 instructions including string operations and a floating-point multiply and add operation (A x B + C). Data cache is 64 Kbytes and memory bus width is 128 bits.

The RISC RS/6000 uses IBM's UNIX-based operating system AIX Version 3 which is based on AT&T System V Release 2 with some additional features from Berkeley Software Distribution (BSD) 4.3. This system conforms to POSIX (Portable Operating System for Computer Environment), IEEE Standard 1003.1-1988. along with additional extensions. Therefore we decided to utilize this UNIX environment to, for instance, take full advantage of its multi-tasking capabilities. The AIX system has C, FORTRAN, and Pascal compilers. Since C is the native language of UNIX, it was the natural choice for development of our system. Strong typing and limited support for system-level operations precluded the use of Pascal. AIX FORTRAN has many extensions to allow it to be used as our system language, however, its methods of dealing with character strings and abstract, multi-type structures are cumbersome. The languages C, FORTRAN, and Pascal are all compiled into identical executable object code and link with the same math libraries, so there is no performance difference between FORTRAN and well written C code.

The Image Processing System

We choose to use the X-Windows system for display of images because it is well-documented and very extensible (allowing this application to be run on different machines). The X-Window System is a network-transparent window system developed at MIT as a general purpose, distributed graphics system which is hardware independent. With this system one can generate multifont text and two-dimensional graphics (lines, arcs, etc.) in a hierarchy of rectangular windows. In a previous imaging system we created a windowing system that allowed windows to overlay each other and be moved, resized, and restacked according to the directions of the operator (1). This same capability is found in X-Windows and thus much of the strategy employed in this earlier system could quite easily be invoked without change using the X system. X display servers can operate with either monochrome or color bitmap displays and can distribute user input to and accept output requests from various client programs located either on the same machine or at a remote machine located on the network. Thus, we will be able to extend our image processing capabilities by acquisition of several inexpensive IBM Xstation 120x which are desktop LAN-attached X-Server terminals.

The performance of a RISC system running UNIX, from the standpoint of the user, is greatly enhanced by the ability to do multi-tasking (the ability to have many tasks executing simultaneously). Thus, for our purposes much of our processing is done in a pipelined configuration; the standard method of doing things in a UNIX environment, that is, to string many small useful building block tools (sub-routines) into a line for execution. The particular sequence order depends on the particular processes involved. For instance, if one wishes to zoom, rotate, and edge-detect, it is often better to put image zoom as the last step because in its present position the array that has to be rotated and filtered would be larger and thus slow the process with unnecessary computation. On the other hand, if an image is to

be zoomed rotated, filtered, and grey scale expanded, rotation should be performed last, because, during rotation, areas of the resultant (rectangular) image that are undefined in the original image are set to intensity level 0 (black). If the previous minimum pixel value was greater than zero, improper grey scale expansion will result. These optimizations are not automatic: they are left to the descretion of the user. However, because modules are small and independent, they can be strung together in many ways not possible with a single, large general purpose program.

Using the pipeline the operator can specify a series of images to be processed according to a selected pipeline and have this process running in the background while he continues with other work. A large (but obviously not unlimited) number of such processes may be running in the background.

Image processing commands can be executed directly from the AIX command line or from within the X-Window image display program. When the user wishes to see the resultant images immediately, for instance, when trying to decide what function/parameters best enhance an image or class of images, the display pipeline is adequate. However, when the user wishes to batch process a series of images through the same pipeline or process a single image many times with slightly varying pipeline parameters, (e.g. amount of rotation), the stand-alone programs are more useful. In this case, UNIX shell command scripts can be used to execute the batch pipes. The command script may be run in the background, allowing overnight execution. Also, the stand-alone programs do not require a display terminal, and, therefore, may be initiated from any remote source.

Examples of common pipeline functions would include zoom (regular and interpolated), rotate with interpolation, filters (Laplace, Sobel, etc.), and gray-scale-expand (either direct or a statistically-based function in which the number of standard deviations is specified). Additionally, if the pipe is initiated from the display program, a function exists to display intermediate results.

Image data is stored in virtual memory in a proprietary format. This is to reduce overhead associated with standard X-Window image formats such as XImages and Pixmaps. One should note that "image" refers not to a displayed image, but rather to the image data structure and the associated data. Of course, before displaying an image, it must be converted to a proper X-Window format. The images are identified in memory by name (a character string). When reading and writing images to disk, this name is used to specify the file name.

Figure 1 shows a negatively-stained image of the hemoglobin of *Lumbricus terrestris* displayed on the high-resolution monitor (top-left) (2). This is a raw image obtained directly from the microscope; full scale is 4185 Å. Individual images of this hemoglobin are extracted, placed in sub-classes according to orientation and used to perform a three-dimensional reconstruction of the original object (3). Shaded images of the reconstructed hemoglobin are shown in the bottom-right area of the screen. This is a rotation sequence with increments of 6°. Movie sequences of the hemoglobin in rotation can be shown by simply displaying the successive rotations in sequence at an appropriate rate (e.g. 30 frames/second). Several of the menu boxes and windowing functions can be seen in other parts of the screen.

Figure 2 shows a sequence of two images of single atoms of gold that have been distributed on an amorphous carbon substrate. Each small round spot in these images corresponds to a single gold atom and has a diameter of 2.4 Å, a dimension limited by the diameter of the electron probe of the STEM. These atom images are recorded from the microscope in 17 second intervals and motion of the individual atoms can be observed by movie rate presentation of successive images. The original movies of atoms in motion, created in this lab in the middle 1970s, utilized a 16 mm camera with frame-by-frame advance.

Computer technology was not generally available at that time to either store the gigabytes of data that were contained in even a short movie or to display them at an appropriate rate. In addition, at that time computers were not powerful enough to process this amount of data in a timely fashion. For instance, the background carbon film can now be removed by digital techniques, and the motions of the individual atoms tracked quantitatively. Today we are looking at this problem again with renewed enthusiasm based on the availability of ever more powerful computing tools coupled with continued reductions in cost.

References

1. G. McNamara, O.H. Kapp, and A.V. Crewe. A new image processing system for STEM images. *13th International Congress of Biochemistry*, Amsterdam, The Netherlands, Aug. 25-30, p. 155 (1985).

2. O.H. Kapp, G. Polidori,, M. Mainwaring, A.V. Crewe, and S.N. Vinogradov. The reassociation of *Lumbricus terrestris* hemoglobin dissociated at alkaline pH. *J. Biol. Chem.* **259**, 628-39 (1984).

3. O.H.Kapp, M.G. Mainwaring, S.N. Vinogradov, and A.V. Crewe. A scanning transmission electron microscopic examination of the hexagonal bilayer structure formed by the reassociation of three of the four subunits of the extracellular hemoglobin of *Lumbricus terrestris*. *Proc. Natl. Acad. of Sci. USA*, **84**, 7532-7536 (1987).

Figure 1. View of the high resolution monitor displaying images of *Lumbricus terrestris* hemoglobin.

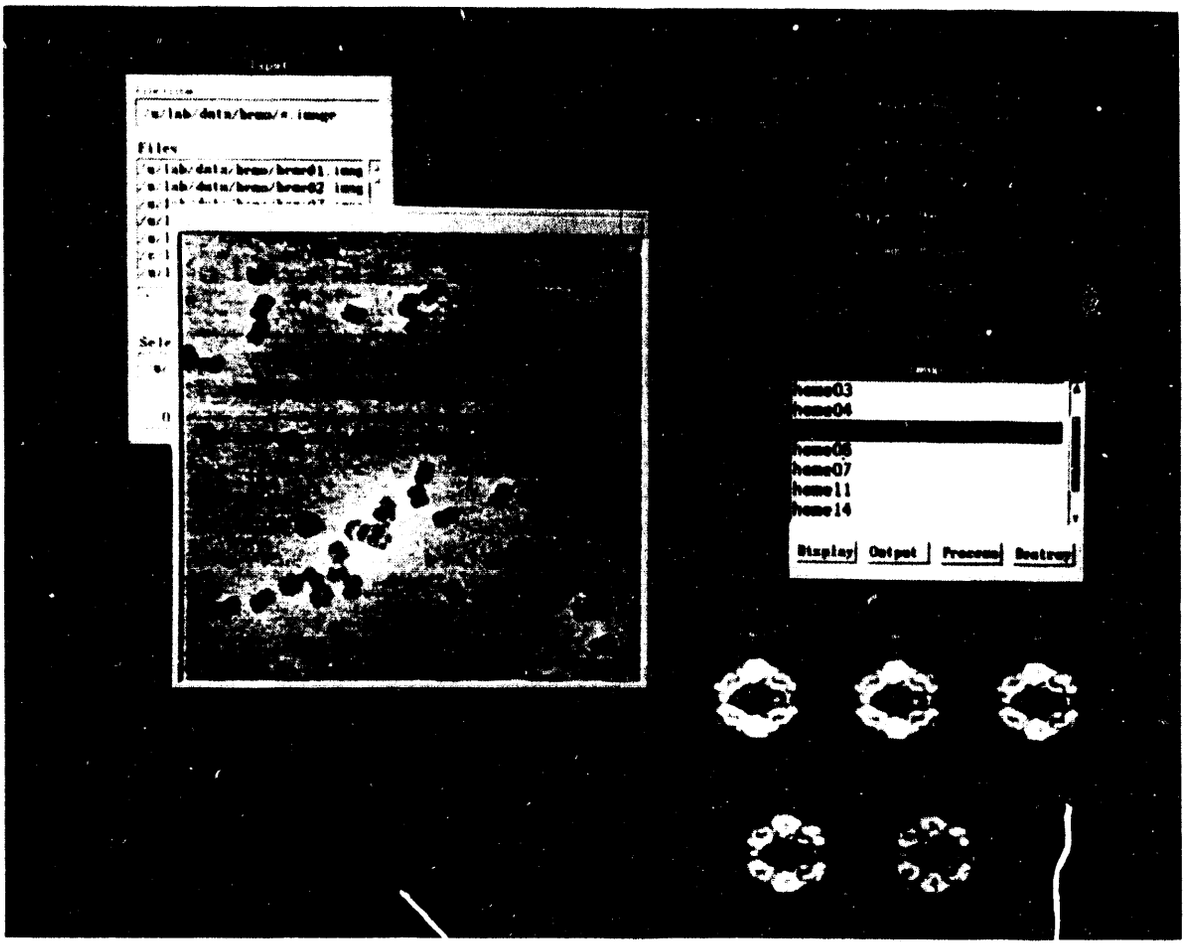
Files
Display
Output
Process
Bootmap

Figure 2. View of the high resolution monitor displaying single atom images. Full scale is 120 Å.

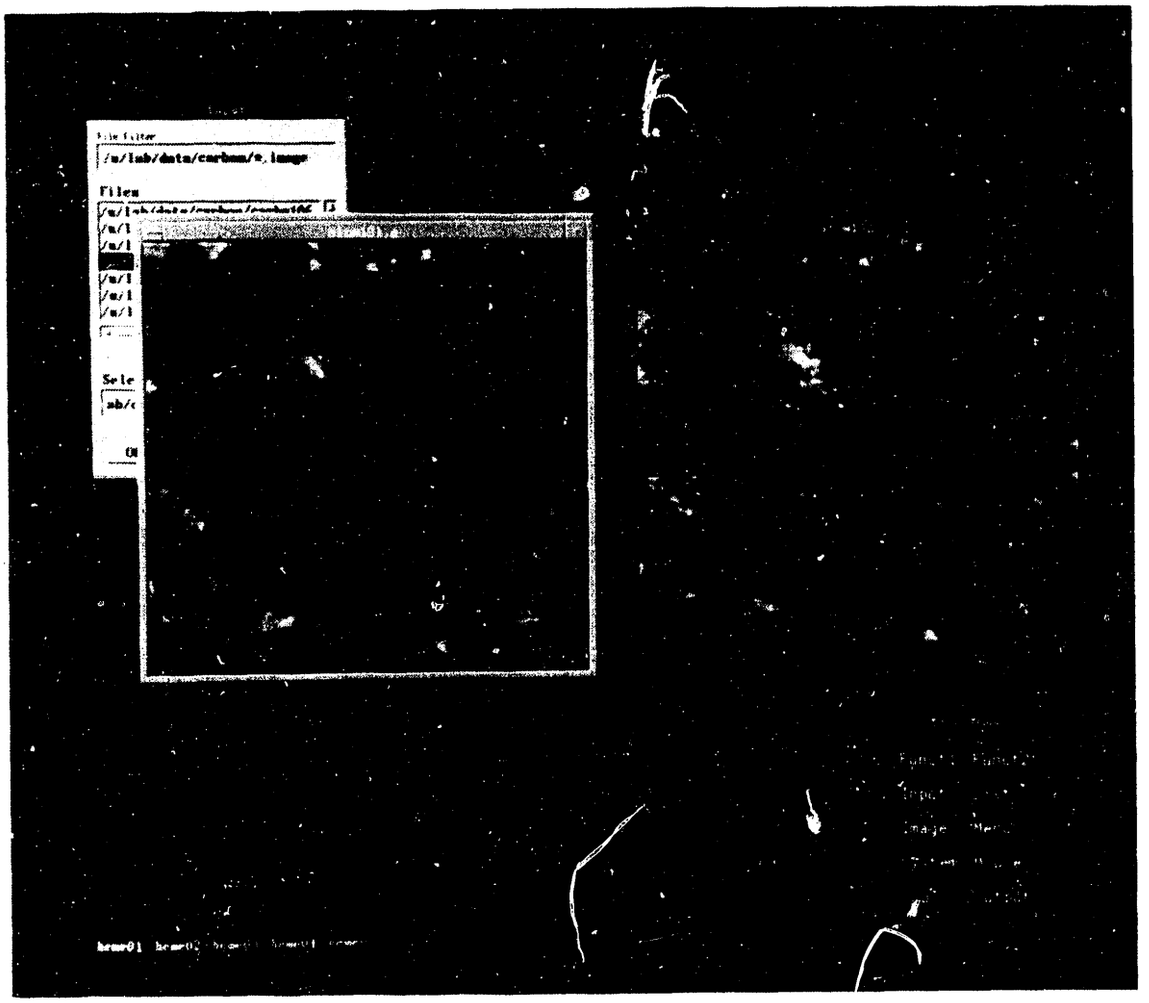
/u/lab/data/carbon/*.image
Files

Image Processing Utilizing an APL Interface

Introduction

In electron microscopy the computer has assumed an increasingly important role in the analysis of electron micrographs. Image processing is used to extract as much information from a micrograph as possible, extending the usefulness of the original data. These techniques continue to improve with advances in computer technology. As computers have become ubiquitous in the research laboratory, the use of these computers is no longer limited to traditional programmers. Image processing software must be available to scientists knowledgeable in microscopy, but not necessarily computer programming.

We are developing an image processing system for the analysis of digital images obtained with the 2.4 Å resolution STEM and the Hitachi field-emission SEM. While recognizing the need to make image processing software easier to use, we should not prevent the more advanced computer user from creating his own subroutines and hence tailoring the imaging environment to his particular needs.

Use of APL

A digital image is an array of numbers representing the intensity and/or color value of a given pixel, with the indices of the array corresponding to the Cartesian location of that pixel. At its most fundamental level, digital image processing is the numerical manipulation of these arrays. The image data of electron micrographs is monochrome; an image is reduced to an array of gray-scale values usually with 8-bit precision (0-255).

An attractive method for manipulating images utilizes the high-level, interpretive language, APL. APL is a matrix oriented programming language. Within APL an array may be treated as a single entity, and most operations may be performed through a combination of built-in primitives. Because APL is an interpreted language, a user may manipulate data interactively as if the computer were a high-powered calculator. However, APL is also a programming language and a user may program functions or subroutines as in other languages.

APL is especially suited for image processing, but without a means of displaying an image it is primarily a data analysis tool. Through the use of interfaces built into IBM's APL2 for the PC (each vendor has its own interface), we were able to write APL arrays (images) directly to a second monitor (IBM 8514) while manipulating the image within APL on the primary monitor. This allows a user facile in APL to simultaneously manipulate APL arrays, to display them on the high-resolution monitor, and thus to provide truly interactive image processing. Since APL is a fully-functional programming language, a user may write and execute any desired function, and is not limited to previously written subroutines (e.g. those provided in commercial image processing software packages).

The Menuing System

Although APL is powerful, it is somewhat difficult to learn. In addition, considerable practice is required to become a facile programmer. Thus, our imaging system needed an interface which would allow users with a bare minimum of APL experience to do image processing. To accomplish this, we created a menu-based interface for the image processing system. Basic image processing functions (pan, zoom, filter, move, cut, rotate, etc.) may be addressed by selecting the appropriate menu box. A user may enter and exit the menuing system multiple times within a single image processing session. Thus, an experienced APL user may write his own functions, while a novice may use the menuing system to do basic image processing, albeit limiting himself to the available packaged functions. With the ability to alternate between the menuing system and the APL interface, a user may learn APL gradually, while still performing useful image processing.

Hardware

Currently we have APL image processing systems running on two platforms. An IBM 4381 mainframe runs under the VM/CMS operating system, with APL2, release 3. A Device Attachment Control Unit (DACU) connects a Metheus display generator (which drives a 1280 x 1024 pixel color display) to the mainframe. In addition, PC-APL is available on an IBM PS/2 Model 70/A21, equipped with two monitors: an 8513 VGA monitor and an 8514 high-resolution 1024 x 768 monitor. The PS/2 Model 70 has 8 megabytes of Random Access Memory (RAM), providing adequate space for the numerical manipulation of images.

The Advantages of the System

Our imaging system's flexibility contributes to the two most beneficial characteristics of our system: ease of use and user control. Our system is specialized. Since it was developed in-house, it is customized for our lab and the work that we do. Though image processing is a broad field, the system's functions are designed to analyze electron micrographs and the names and commands implemented are consistent with those used in the laboratory. Thus, users of our system find that it is easy to use because it has been specifically adapted for their field of expertise. The system is unique, however, in that its specialization may be extended to other disciplines. Since the menu system is written in the interactive language APL, an advanced user may add functions required for another field to the menu. A sequence of menu buttons commonly used together may be replaced (like a macro), by wiring an APL function that calls the functions associated with the particular menu boxes. This may be done without losing the original function, so the original functions may be recalled. Its extendibility permits the menu functions to grow with the knowledge and needs of a particular lab and not be limited to what the original programmer has deemed important.

There are a variety of ways in which the image processing environment may be controlled. An imaging operator may move in and out of the menuing system at whim; in this fashion he may see how a particular function was programmed and is not limited to a particular language. In addition, if APL is too awkward or slow, a programmer may write a function in FORTRAN, or assembly language, which

may then be called from APL. Commands may be entered interactively and written into a subroutine to be used later.

In APL, the user works with the actual data as well as with the visual representation. He may modify the appearance of an image by operating on its numerical representation. For instance, to decrease the brightness of an image, the user may multiply all elements of the corresponding numerical array by an arbitrary factor (e.g. 0.7) with a single APL expression. For an image A the appropriate APL expression is

$$A \leftarrow A \times 0.7$$

Because APL addresses arrays of any rank (one, two, or three dimensional) with the same syntax, the above expression would be used regardless of the dimensionality of the array A. The size of the image (as long as it fits in memory) is inconsequential; operations affect the array as a whole, or as rows, columns, or elements. Unlike other languages, loops are not required in APL. Since loops and many other "bookkeeping" activities are not necessary, programming time is reduced and algorithm development is put into the hands of a broader range of users (non-programmers).

APL is also a "mature" language, having been developed as a fully functional programming language over the past 25 years. It is complete, containing all mathematical and control functions that might be needed. Unlike many newer image processing languages, APL has been refined, improved, and optimized many times. Any numerical operations to which one might choose to subject image data may be written in APL, and, as the user is working with the actual data as well as with its visual representation, he gains a greater understanding of the effect of mathematical operations on the appearance of the image.

Figure 1 shows the image processing system during a typical session. On the right is the PS/2-70, the 8513 VGA monitor, and the mouse. The VGA monitor is displaying an APL function which is being modified. The 8514 high resolution screen (on left) is used to display the images being manipulated. The PS/2-70 is equipped with an Intel 80386 CPU and 8 megabytes of RAM.

Figure 2 shows a close-up of the high-resolution monitor which is displaying a 256 x 256 pixel chest x-ray. A box (128 x 128 pixels) is drawn over the image, this section has been cut out, re-scaled, and appears on the left of the screen. In this case, the re-scaled image was obtained by raising each element of the original array to a fractional exponent followed by gray-scale expansion (as described above). The histogram (top-left) is generated from the pixel intensities occurring in the processed 128 x 128 image. All of the image porcessing shown was performed with user-written APL code.

Figure 1.

A view of the image processing system

Figure 2.

View of the high-resolution monitor.

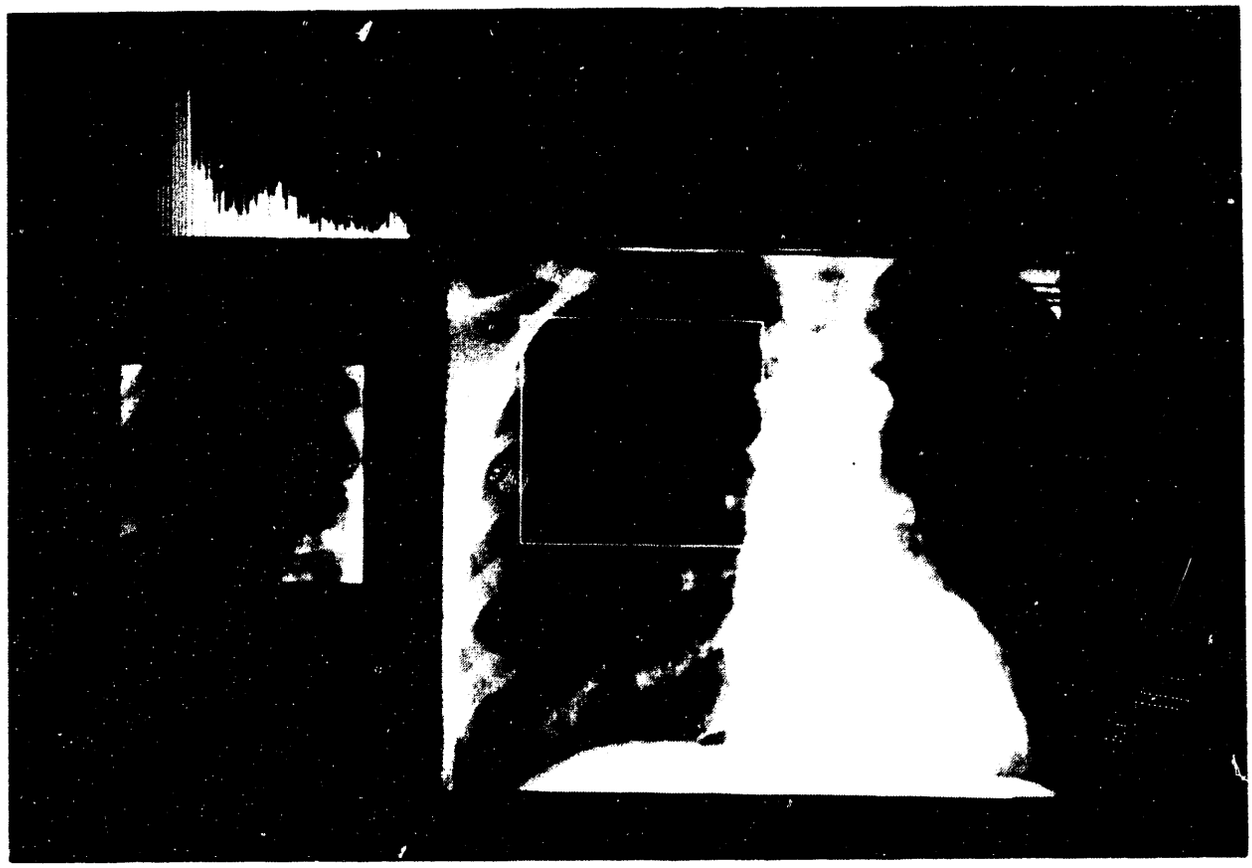

Networking of an Electron Microscope Laboratory Internally and to the Internet

Introduction

The prevalence of computers within scientific laboratories has brought increased attention to the problems of data transfer, storage, and retrieval. Specifically in electron microscopy, image data is produced at a very high rate, and the transfer and management of these large data sets is a major concern. Various technologies are needed to transfer images between computers: the analog image from the microscope must first be digitized and transferred to computer, then the digital image must be transferred to another computer or mass storage device (preferably in compressed form), and finally, the images must be made available for rapid access by researchers. We have developed data manipulation tools and implemented hardware solutions to address these problems.

Data Acquisition

Data acquisition is the first step in the image transfer process. We have worked from scratch to acquire data from our Hitachi HFS-II scanning electron microscope (SEM). This SEM predates mass scale digital image processing and does not allow digital image capture. Since the microscope was not built around any video standards (i.e., RS170 or NTSC), we decided to acquire data as a raw string of intensity values and convert it into image form on the computer after the microscope had finished scanning. This approach decreases the amount of work that the data acquisition hardware needs to perform, thus permitting the use of a lower performance computer.

We decided to use an IBM PC/AT as our data acquisition computer, as its performance, price, availability, and expansibility best fit our needs and resources. The data from the microscope is delivered at the rate of one frame every 17 seconds, and, in order to grab these images in a 512 x 512 format, data acquisition must occur at a rate of at least 15,000 samples per second. At this performance level, the most economical configuration is a PC/AT with a data acquisition card. In order to overcome the difficulty of building a custom frame grabber, we used a fast data acquisition system and captured the image's scan lines sequentially. After the scan lines were obtained on the computer, they were combined to form an image. To increase the speed at which data may be acquired, the images were written directly to a RAM disk, and then transferred to the hard disk for temporary storage. After enough images were obtained (limited by local storage, approximately 100), they were transferred by Ethernet to a local image archive device with greater storage capabilities. The system is connected to Ethernet with an Ethernet adapter card associated with the PC/AT. The image files are transported over the local Ethernet using

TCP/IP, and reach the Internet through a campus gateway (see Figure 1). Thus, the images collected on the microscope are accessible by researchers worldwide.

The Network

We chose to use the existing campus Ethernet to connect the microscope with our image archive computers instead of installing a dedicated "network" because the existing network provided an easy and inexpensive means of connecting the laboratory microscopes, situated on different floors in different wings of the building, to our two archive facilities, also located in different rooms. After considering the amount of data which needed to be transferred (20 megabytes with a maximum size of 1 megabyte per file) and the necessary time scale (less than 1 minute real time), we decided that this network would be adequate. Although the amount of data is significant, and may slightly degrade its performance for a couple of seconds, the existing Ethernet satisfactorily performs this function, as the real time it takes a microscopist to acquire 20 megabytes of image data is at least one hour.

The images are stored on one or more of our four high-performance RISC workstations (two IBM 6000 and two DEC 5000s, combined storage capacity = three gigabytes) or on the disk sub-system of the lab mainframe (IBM 4381, 5 gigabytes of disk). After the raw images are transferred to these computers, they are converted into an archived form (compressed and time stamped). They are then stored until they may be visualized on an image processing workstation.

We are in the process of evaluating data compression algorithms and image archival formats in this laboratory. An image archival format should provide a means of maintaining a database of these images, thus making them more accessible to researchers. The problem of archiving images is concerned with the ability to access the image or subclass of images that are desired. Data compression is an improving technology, and consideration must be given to the type of image compression employed. Micrographs are already limited by the resolutions of the microscope and the data acquisition system; it is unacceptable to lose image information during image compression (e.g. this precluded the use of some fractal-based compression algorithms). Image decompression should also be relatively fast in real time, so that a user may decompress an image without unreasonable delay.

This electron microscope laboratory is now connected with four other imaging facilities at the University of Chicago by a dedicated, high-speed network. One of us (O.K.) is co-investigator of a proposal funded by the Illinois Challenge Fund to develop a "High-performance Network and Archival Facility for Imaging Science." This is a joint project involving industrial partners (IBM Corporation, Ultra Network Technologies Corporation and cisco Systems Corporation) and university research laboratories involved in biomedical, geophysical, astronomical, and electron microscopy imaging. As part of this project, a series of IBM second generation RISC RS-6000 workstations and servers have been obtained for these labs. Programming support is provided to develop software to render, store, and retrieve image collections from these laboratories.

Over 200 scientists at the University of Chicago are involved in various aspects of imaging science, such as image-data acquisition, reconstruction, manipulation, and evaluation. Although this group is comprised of a broad range of disciplines, there are a variety of generic techniques for which common technology is largely absent. A major goal of this work is to provide such a common technology and the techniques to help lower the barriers to interdisciplinary research.

Figure 1 shows a schematic of our electron microscope laboratory and its relationship to the campus Ethernet, Internet, and high-speed imaging network. As may be seen in this figure, images obtained locally may be transferred to the IBM 4381 for local storage. There they may be viewed on either of the two image processing stations connected to the 4381, or on two DEC 5000 or two IBM 6000 RISC workstations. If computationally intensive image processing is needed, images may be transferred via Ethernet to the high-speed image network, or to the high-performance DEC or IBM workstations.

After they are available to the high-speed image network, images may be processed using dedicated image processing hardware. The particular choice of storage location will depend on such factors as the size of the data set, the image processing functions required, and the duration of storage. For instance, if a small data set (less than 50 images) is to be analyzed immediately and requires modest image processing power, it most likely would be stored on the disk subsystem of the IBM 4381 mainframe. Larger data sets requiring high-performance image processing would be archived on the high-performance network servers and analyzed on the high-end DEC and IBM workstations.

Figure 1.

Schematic of the laboratory microscopes and information systems.

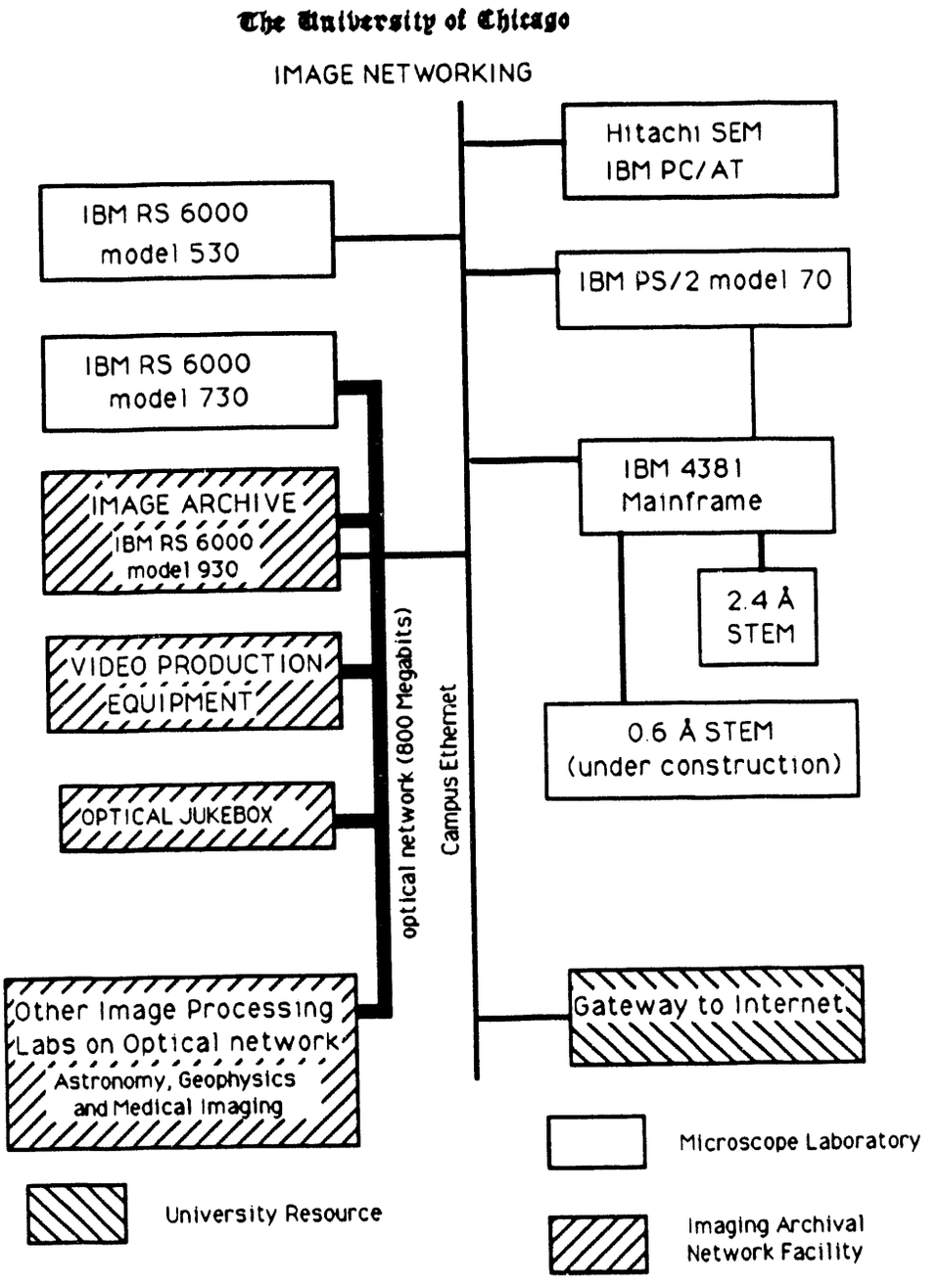
The University of Chicago
IMAGE NETWORKING
Hitachi SEM
IBM PC/AT
IBM RS 6000
model 530
IBM PS/2 model 70
IBM RS 6000
model 730
IBM 4381
Mainframe
IMAGE ARCHIVE
IBM RS 6000
model 930
2.4 Å
STEM
VIDEO PRODUCTION
EQUIPMENT
0.6 Å STEM
(under construction)
OPTICAL JUKEBOX
optical network (800 Megabits)
Campus Ethernet
Other Image Processing
Labs on Optical network
Astronomy, Geophysics
and Medical Imaging
Gateway to Internet
Microscope Laboratory
University Resource
Imaging Archival
Network Facility

Figure 1

Laboratory Publications

Bibliography

1989-1991

1. Z. Shao, Extraction of Secondary Electrons in a Newly Proposed Immersion Lens, *Rev. Scientific Instruments* **60** (1989) pp. 693-699.

2. A.V. Crewe, D.L. Clayton, D.A. Crewe, and K. Moscicka, User-Friendly Field Emission, *Proc. 47th Annual EMSA Mtg.* (San Antonio, TX, 1989).

3. A.V. Crewe, Small, Cool Lenses, *Proc. 47th Annual EMSA Mtg.* (San Antonio, TX, 1989).

4. O.H. Kapp and S.N. Vinogradov, Direct Calculation of Subunit Stoichiometry from Amino Acid Compositions of Multimeric Proteins and Their Subunits, *International Symposium on Invertebrate Dioxygen Carriers* (Leuven, Belgium, 1989).

5. O.H. Kapp, J.S. Wall and S.N. Vinogradov, Comparison of the Three-Dimensional Reconstructions of the Hemoglobins of *Lumbricus terrestris* and *Macrobdella decora* from STEM data, *International Symposium on Invertebrate Dioxygen Carriers* (Leuven, Belgium, 1989).

6. O.H. Kapp, M. Schmuck, I. Pilz and S.N. Vinogradov, Comparison of the Molecular Dimensions and Hydrodynamic Properties of Annelid Hemoglobins Obtained by STEM and SAXS, *International Symposium on Invertebrate Dioxygen Carriers* (Leuven, Belgium, 1989).

7. Z. Shao and P.S.D. Lin, A High Resolution Low Voltage Electron Optical System For Very Large Specimens, *Rev. Sci. Instrum.* **60** (1989) p. 3434.

8. O.H. Kapp, A.N. Qabar, M.C. Bonner, D.A. Walz, J.S. Wall, S.N. Vinogradov, M.S. Stern, and M. Schmuck, Quaternary Structure of the Giant Extracellular Haemoglobin of the Leech *Macrobdella Decora*, *J. Mol. Biol.* **213** (1990) p. 141.

9. O. H. Kapp, A. N. Qabar and S. N. Vinogradov, Calculation of Subunit Stoichiometry of Large, Multisubunit Proteins from Amino Acid Compositions, *Anal. Biochem.* **184** (1990) pp. 74-82.

10. Z. Shao and X. D. Wu, Properties of a Four-Electrode Adjustable Electron Mirror as an Aberration Corrector, *Rev. Sci. Instrum.* **61** (1990) p. 1230.

11. Z. Shao and X. D. Wu, *Appl. Phys. Lett.* **55** (1989) p. 2696.

12. Z. Shao, *Rev. Sci. Instrum.* **60** (1989).

13. Z. Shao and X. D. Wu, A study on Hyperbolic Mirrors as Correctors, *Optik* **84** (1990) p. 51.

14. X. D. Wu and Z. Shao, A Qualitative Analysis of Chromatic Aberration of

"Thick" Electrostatic Lenses, *Optik* **84** (1990) p. 66.

15. S. Ruan and O. H. Kapp, Progress on the Sextupole-Corrected Sub-Angstrom Resolution Scanning Transmission Electron Microscope: An Abstract, *1990 Midwest SPIE Meeting* (Rosemont, IL, Sept. 27-29, 1990).

16. C. Zmola and O. H. Kapp, Image Processing Utilizing an APL Interface: An Abstract, *1990 Midwest SPIE Meeting* (Rosemont, IL, Sept. 27-29, 1990).

17. C. Zmola and O. H. Kapp, Networking of an Electron Microscope Laboratory Internally and to the Internet: An Abstract, *1990 Midwest SPIE Meeting* (Rosemont, IL, Sept. 27-29, 1990).

18. M. J. Ryan and O. H. Kapp, Development of an Image Processing System on a Second Generation RISC Workstation: An Abstract, *1990 Midwest SPIE Meeting* (Rosemont, IL, Sept. 27-29, 1990).

19. O.H. Kapp and S.N. Vinogradov, The Structure of the Hemoglobin of *Eudystilia Vancouverii* Evidence for Isolated Bracelet Protein, *10th International Biophysics Congress-Satellite Meeting* (Whistler, British Columbia, July 1990).

20. S.N. Vinogradov, M. Mainwaring and O.H. Kapp, The Quaternary Structure of the Giant Hemoglobins and Chlorocruorins, *10th International Biophysics Congress-Satellite Meeting* (Whistler, British Columbia, July 1990).

21. O.H. Kapp M.G. Mainwaring, S.N. Vinogradov and A.V. Crewe, The Extracellular Hemoglobin of *Amphitrite Ornata:* Its Molecular Size, Subunits and Its Dissociation, *10th International Biophysics Congress-Satellite Meeting* (Whistler, British Columbia, July 1990).

22. S. Ruan and O. H. Kapp, Progress on the Sextupole-Corrected Sub-Angstrom Resolution Scanning Transmission Electron Microscope, *SPIE Proceedings* **1396** (1991) pp. 298-310.

23. C. Zmola and O. H. Kapp, Image Processing Utilizing an APL Interface, *SPIE Proceedings* **1396** (1991) pp. 51-55.

24. C. Zmola and O. H. Kapp, Networking of an Electron Microscope Laboratory Internally and to the Internet, *SPIE Proceedings* **1396** (1991) pp. 331-334.

25. M. J. Ryan and O. H. Kapp, Development of an Image Processing System on a Second Generation RISC Workstation, *SPIE Proceedings* **1396** (1991) pp. 335-339.

26. Z. Shao, A Note on the Resolution of Low Energy Reflection Electron Microscope Based on Wave Electron Optics, *Ultramicroscopy* (in press).

27. Z. Shao and Y.L. Wang, On the Optimisation of Ion Micro-Probes, *J. Vac. Sci. Technol. B.* (in press).

28. P.K. Sharma, A.N. Qabar, O.H. Kapp, J.S. Wall and S.N. Vinogradov., The principal subunit of earthworm hemoglobin is a dodecamer of heme containing chains, *Structure and Function of Invertebrate Oxygen Binding Proteins: Proceedings Biophysical Society Satellite Symposium of the Xth International Biophysics Congress* (1991) pp. 65-72. S.N. Vinogradov and O.H. Kapp, eds. Springer-Verlag.

29. P.K. Sharma, A.N. Qabar, O.H. Kapp, J.S. Wall and S.N. Vinogradov., Studies of the Dissociation of *Eudistylia Vancouverii* chlorocruorin,. *Structure and Function of Invertebrate Oxygen Binding Proteins: Proceedings*

Biophysical Society Satellite Symposium of the Xth International Biophysics Congress (1991) pp. 79-86. S.N. Vinogradov and O.H. Kapp, eds. Springer-Verlag.

30. O.H. Kapp and S.N. Vinogradov, Direct Calculation of Subunit Stoichoimetry from Amino Acid Compositions of Multimeric Proteins and Their Subunits, *Invertebrate Dioxygen Carriers* (in press). G. Preaux, ed. University of Leuven press.

31. O.H. Kapp, J.S. Wall and S.N. Vinogradov, Comparison of the Three-Dimensional Reconstructions of the Hemoglobins of *Lumbricus terrestris* and *Macrobdella decora* from STEM Data, *Invertebrate Dioxygen Carriers* (in press). G. Preaux, ed. University of Leuven press.

32. O.H. Kapp, M. Schmuck, I. Pilz and S.N. Vinogradov, Comparison of the Molecular Dimensions and Hydrodynamic Properties of Annelid Hemoglobins Obtained by STEM and SAXS, *Invertebrate Dioxygen Carriers* (in press). G. Preaux, ed. University of Leuven press.

33. Z. Shao and Y.L. Wang, Evaluation of Small Ion Probes in an Aberrated System, (to be published).

34. G. McNamara and O.H. Kapp, A New Image Processing System for STEM Images, *Ultramicroscopy* (paper submitted).

35. O.H. Kapp and Z. Shao, Studies of the Effects of Noise on the Inexact Reconstruction Technique, (in preparation).

36. O.H. Kapp, Progress in Microimaging, *1991 Midwest SPIE Meeting* (Rosemont, IL, Sept. 25-27, 1991).

37. O.H. Kapp, The Quaternary Structure of the Annelid Hemoglobins, *Electron Micro. Rev.* (in preparation).

38. O.H. Kapp, The Use of an APL Interface in Image Processing, (in preparation).

39. O.H. Kapp, The Hemoglobin of Spirographis, (in preparation).

APPENDIX

The appendix includes a copy of the program announcement for the conference held by O. Kapp in the Physics Department entitled "First Annual Conference on Developments in High Performance Visualization" and also the front matter and index of the *Proceedings of the Xth International Biophysics Congress Satellite Meeting* entitled *Structure and Function of Invertebrate Oxygen Binding Proteins* that were prepared and edited for publication in this laboratory.

FIRST ANNUAL CONFERENCE
ON
DEVELOPMENTS IN HIGH PERFORMANCE VISUALIZATION

Joint Industry-University Conference

Sponsored by the Enrico Fermi Institute & the Center for Imaging Science at the University of Chicago

Conference Organizers: O.H. Kapp and R.N. Beck

The Enrico Fermi Institute and the Center for Imaging Science will host a joint Industry-University conference on high-performance workstations/visualization the week of July 23-25, 1990. We would like to provide an open forum for industrial representatives to review their future plans and to present practical demonstrations of their most current products. Interspersed throughout the manufacturers demonstrations will be guest lecturers speaking on various aspects of high performance computing/visualization.

The conference will be held at the University of Chicago in the Kersten Physics Teaching Center, 5720 S. Ellis, located on the SW corner of 57th St. and Ellis Ave. in Hyde Park. The main presentations will be held in Room 115. In addition each corporate sponsor will have a laboratory or a classroom where they will display and demonstrate their workstation product lines throughout the meeting. Admission is free and registration will be inside the South Entrance to the Kersten Center each day from 9:00 AM to 4:00 PM. Refreshments will be available in Room 206 throughout the meeting, courtesy of the corporate participants. Parking is available in the parking garage at 59th St. and Cottage Grove.

All workstation demonstrations in Room 115 will be able to utilize an Electrohome ECP4000 graphics projection system which provides a wide screen display without loss of the original pixel resolution of the workstation monitor. This equipment has been generously donated by DataDisplay Corporation of Elk Grove Village, IL.

PROGRAM

Monday, July 23

10:00-11:00 AM

Introductory Remarks: **Professor Robert N. Beck**, Director, The UofC/ANL Center for Imaging Science

Introductory Lecture: **Professor Tom DeFanti**, University of Illinois at Chicago

Title of talk: *A CRT in Every Forehead*

11:00-12:30 AM

Lecture: **Doug Schaff**, Senior Product Manager, SUN Microsystems, Inc.

Title of talk: *An Integrated Visualization Environment for the Desktop*

12:30-1:30 PM

Lunch (A list of local dining facilities is available at the registration desk)

1:30-2:30 PM

Lecture: **Scott Teissler**, Assistant Provost for Computing at the UofC and Director of the University Computing Organizations

Title of talk: *A High Performance Network and Archival Facility for Imaging Science*

2:30-3:15 PM

Lecture-Demonstration: **William Samayoa**, Senior Graphics Analyst & Medical Imaging Specialist, Cray Research, Inc.

Title of talk: *Supercomputer Biomedical Visualization:* Picture Archiving Systems (PACS), Multi-mode Imaging, Magnetic Resonance Imaging (MRI), Positron Emission Tomography (PET).

3:15-4:00 PM

Lecture-Demonstration: **Dr. Timothy Whitley**, Cray Research, Inc.

Title of talk: *Computational Chemistry on Cray Supercomputers:* Cray Unichem demonstration using a high-resolution graphics workstation remotely linked to a Cray Research supercomputer

4:00-5:00 PM

Demonstration: **Dr. Timothy Whitley and Daniel Hogberg**, Cray Research, Inc.

Demonstration of Multi-Application "Touch-Screen" Video Display: including examples in Weather Modeling, Molecular Dynamics, Computational Fluid Dynamics and Crash Simulations

Tuesday, July 24

10:00-11:00 AM

Lecture-Demonstration: **Jack Gold**, Imaging Application Marketing Manager, Digital Equipment Corporation

Title of talk: *An Integrated Visualization Environment*

11:00-12:00 AM

Lecture: **Professor Georges Grinstein**, Director, Computer Graphics Laboratories, University of Lowell, Lowell, Massachusetts

Title of talk: *Experimental Approaches in Scientific Data Visualization*

12:00-1:30 PM

Lunch

1:30-2:30 PM

Lecture: **Professor Robert N. Beck**

Title of talk: *The Emerging Field of Imaging Science, a New Intellectual Discipline*

2:30-3:15 PM

Lecture-Demonstration: **Mike Savello**, DECstation Product Manager, Digital Equipment Corporation.

Title of talk: *High Performance Graphics Workstations and Workstations into the 90s:* (Features DECstation 5000 Model 200)

3:15-4:00 PM

Lecture-Demonstration: **Peter Hallett**, Marketing Manager, Precision Visuals, Inc.

Title of talk: *PV-WAVE, Precision Visuals' Workstation Analysis and Visualization Environment*

4:00-5:00 PM

Lecture to be announced: SUN Microsystems, Inc.

Wednesday, July 25

10:00-10:30 AM

Lecture: **Clint Potter**, National Center for Supercomputing Applications (NCSA), University of Illinois at Champaign-Urbana

Title of talk: *A Distributed High Performance Computing Architecture for the Biomedical Imaging Laboratory*

10:30-11:00 AM

Lecture: **Ray Idaszak**, National Center for Supercomputing Applications (NCSA), University of Illinois at Urbana-Champaign

Title of talk: *High Performance Distributed Visualization*

11:00-12.30 AM

Lecture-Demonstration: **Ian Reid**, Vice President of Visualization, Stardent Computer, Inc.

Title of talk: *Scientific Visualization: New Insight and New Opportunities*

12:30-1.30 PM

Lunch

1:30-2:30 PM

Lecture to be announced: Stardent Computer, Inc.

2:30-5:00 PM

Lecture-Demonstration: Silicon Graphics, Inc. Dr. William Collins

Please address inquiries to either Bud Kapp or Bob Beck at the addresses given below.

Conference Organizers:

Dr. Oscar (Bud) Kapp
Enrico Fermi Institute
University of Chicago
5640 S. Ellis Ave.
Chicago, 60637 Illinois
ph: 312-702-7820
FAX 312-702-5863
bud@rainbow.uchicago.edu
bud@uchistem.bitnet

Prof. Robert N. Beck
Director, Center for Imaging Science
The Franklin McLean Memorial Research Institute
5841 Maryland Ave.
Chicago, 60637 Illinois
ph: 312-702-6271
FAX 312-702-0371
rnbk@midway.uchicago.edu

Serge N. Vinogradov and Oscar H. Kapp

Editors

Structure and Function of Invertebrate Oxygen-Binding Proteins

Please place on Copyright Page:

Proceedings of the Satellite Symposium of the Xth International Biophysics Congress Held in Whistler, British Columbia, Canada July 24–27, 1990

Serge N. Vinogradov
Biochemistry Department, Wayne State University School of Medicine, Detroit, MI 48201, USA

Oscar H. Kapp
Enrico Fermi Institute, University of Chicago, Chicago, IL 60637, USA

Introduction

The content of this volume is based predominantly on the lectures and posters presented by the participants of the Satellite Symposium "Structure and Function of Invertebrate Oxygen-Binding Proteins," held in Whistler, British Columbia, Canada, July 24–27, 1990, the week prior to the Xth International Biophysics Congress in Vancouver, British Columbia. Because not everyone who wished to attend this symposium was able to do so, we decided to also include in this volume contributions from several non-participants.

This volume is dedicated to the memories of Eraldo Antonini, Bernt Linzen and Robert Terwilliger, whose untimely deaths in recent years have tragically deprived all of us working in the area of oxygen-binding proteins of esteemed colleagues and personal friends. We would like to thank Maurizio Brunori, Emilia Chiancone, Heinz Decker, Jürgen Markl and Joseph Bonaventura for contributing the memorial essays.

We would like to thank the following for their support: Dr. G.T. Heberlein, Vice President for Research and Dean of the Graduate School, and Dr. R.J. Sokol, Dean of the School of Medicine, Wayne State University, the Center for Imaging Science of the University of Chicago, IBM Corporation, the National Institutes of Health and the U.S. Department of Energy. In particular, we would like to acknowledge our debt to Ms. Virginia M. Boyce for the careful editing and preparation of the manuscripts for publication.

S.N. Vinogradov
O.H. Kapp

Contents

PART TWO: STRUCTURE AND FUNCTION

PART THREE: AMINO ACID AND cDNA SEQUENCES

END

DATE FILMED

01/23/92